TESTING THEORIES FOR THERMAL TRANSPORT USING HIGH PRESSURE

BY

WEN-PIN HSIEH

DISSERTATION

Submitted in partial fulfillment of the requirements
for the degree of Doctor of Philosophy in Physics
in the Graduate College of the
University of Illinois at Urbana-Champaign, 2011

Urbana, Illinois

Doctoral Committee:

Professor S. Lance Cooper, Chair
Professor David G. Cahill, Adviser
Professor Robert Clegg
Assistant Professor Dallas Trinkle

ABSTRACT

This dissertation focuses on experimental studies of thermal transport in various materials, such as heat transfer in crystals and amorphous polymers, and across interfaces, using an ultrafast pump-probe method, time-domain thermoreflectance (TDTR), combined with gem anvil cell techniques. I demonstrated that pressure tuning of physical properties of materials is an elegant approach to test the validity of theories for thermal transport.

Pressure dependence of the cross-plane thermal conductivity $\Lambda(P)$ of a layered muscovite mica crystal was measured by TDTR combined with diamond anvil cell techniques. Under a simple relaxation time approximation, most of the $\Lambda(P)$ of muscovite mica can be described by the pressure dependence of the cross-plane sound velocity, indicating that the cross-plane sound velocity plays an important role in the thermal transport in a layered crystal.

The validity of the minimum thermal conductivity model for amorphous polymers was verified by the good agreement between my measurements of the pressure dependent thermal conductivity of poly(methyl methacrylate) (PMMA) and the model prediction. The thermal energy exchange between non-propagating

vibrational modes is the dominant mechanism of thermal transport in amorphous polymers.

I also used high pressure to demonstrate the importance of interface stiffness on the interfacial thermal transport. By measuring the pressure dependence of thermal conductance $G(P)$ of clean and modified Al/SiC interfaces, I found that $G(P)$ of a clean interface with high interface stiffness is weakly dependent on pressure and can be well accounted for by the diffuse mismatch model (DMM). By contrast, $G(P)$ of modified interfaces with low interface stiffness initially increase rapidly with pressure; as the interface stiffness is increased to be comparable to the stiffness of chemical bonds, $G(P)$ saturate at the value for the clean interface and value predicted by the DMM.

In order to extend the TDTR measurements to high pressures and high temperatures, I studied the pressure dependent thermoreflectance and piezo-optical coefficient of metal film transducers—Al, Ta, and Au(Pd) alloy (≈5 at. % Pd) at a laser wavelength of 785 nm. The thermoreflectance of Ta and Au(Pd) are comparable to that of Al at ambient conditions and independent of pressure in the range $0<P<10$ GPa. Ta and Au(Pd) also present strong acoustic echo strengths in this pressure range. I conclude that Ta and Au(Pd) films can replace Al as metal transducers and extend TDTR to higher pressures and temperatures.

Dedicated to my parents, Chia-Cheng Hsieh and Pi-Lien Huang,

and my wife, Tein-Chin Lin,

for their love, supports, and encouragements

ACKNOWLEDGEMENTS

I am deeply grateful to my Ph.D. advisor, Prof. David Cahill, for his ceaseless support, encouragement, inspiration throughout my Ph.D. study. Thank you for leading me into the field of “high-pressure thermal physics” and providing me with excellent environment and abundant resources for doing researches. Besides the physics of thermal transport and high pressure, the most important things I learned from David are the way and the scrupulous attitude to analyze and solve problems.

I would also like to thank many collaborators, including Prof. Jie Li, Prof. Pawel Keblinski, Prof. Paul Braun, Prof. Dallas Trinkle, Dr. Alex Goncharov, Dr. Bin Chen, Dr. Mark Losego, Dr. Allen Dalton, Dr. Sergei Shenogin, Dr. Wai Lun Chan, and Austin Lyons. Special thanks go to Dr. Bin Chen, who taught me a lot of techniques used in the high-pressure experiments when I just jumped into this brand-new field and gave me a broad picture about the current progress in the high pressure field. Even though we just worked together for about six months, that was a wonderful research experience!

I also want to thank all the members in Prof. Cahill’s group: Dr. Dong-Wook Oh, Prof. Yee Kan Koh, Ji-Yong Park ,Wei Wang, Andrew Hafeli, Yuxin Wang,

Tamlin Matthews, Dr. Chang Ki Min, Trong Tong, Richard Wilson, Dr. Joe Feser, and Junglo Park. Many thanks for your great help in the experiments and valuable suggestions and inspirations. In addition, special thanks also go to Prof. Jay Bass and his students, for generously letting me use their facilities to prepare my high pressure samples. Of course, I also want to thank many research staffs in MRL and the laser facility which generates essentially all the data in this thesis.

Thank many good friends studying together on this campus, Tzu-Jung Lin, Chi-Hao Tsai, Kuo-Chuan Pan, Ching-Kai Chiu, Kai-Pin Liao, Rosa Chang, Julia Wang, Kuei Sun, Po-Yao Chang, and many people in TSA badminton club (absolutely I still miss many people). Thank you all for sharing the wonderful life in Chambana and giving me excellent memories. Finally, I am deeply indebted to my parents, Chia-Cheng Hsieh and Pi-Lien Huang, and my wife Tein-Chin Lin, for their ceaseless love and support.

This work was partially supported by the US Air Force Office of Scientific Research Grant No. MURI FA9550-08-1-0407 and the Carnegie-DOE Alliance Center (CDAC) through grant DE-FC52-08NA28554. I also received support of the Taiwan Merit Scholarship from the National Science Council of Taiwan, Republic of China.

TABLE OF CONTENTS

LIST OF FIGURES

LIST OF ACRONYMS

TDTR	Time-domain thermoreflectance
DAC	Diamond anvil cell
EOS	Equation of state
PMMA	Poly(methyl methacrylate)
DMM	Diffuse mismatch model
LS	Leibfried-Schlömann
ATRP	Atom-transfer radical polymerization
MD	Molecular dynamics
RIS	Rotational isomeric state
AMM	Acoustic mismatch model
hcp	Hexagonal-closed package
FWHM	Full-width at half maximum
DOS	Density of state

LIST OF SYMBOLS

Λ	Thermal conductivity
J	Heat flux
∇T	Temperature gradient
G	Interface thermal conductance
ΔT	Temperature drop
B_{T}	Isothermal bulk modulus
P	Pressure
t	Delayed time between pump and probe pulses
Q	Quality factor
rf	Radio-frequency
f	Modulation frequency of pump pulse
D	Thermal diffusivity
w_0	Spot size of pump and probe beams
P_i	Incident laser power
R	Optical reflectivity
ΔT_s	Steady-state temperature rise
d_{th}	Thermal penetration depth
C_s	Volumetric heat capacity of the sample
V_{in}	In-phase voltage of the rf lock-in amplifier
V_{out}	Out-of-phase voltage of the rf lock-in amplifier
h_{i}	Thickness of interface layer
C_{i}	Volumetric heat capacity of interface layer
h_{Al}	Thickness of Al
C_{Al}	Volumetric heat capacity of Al
Λ_{Al}	Thermal conductivity of Al
f_{B}	Brillouin frequency
N	Index of refraction
v_l	Longitudinal speed of sound
λ	Laser wavelength
F	External force
A	Contact area of culet

C_{33}	Cross-plane elastic constant
ρ	Mass density
n	Atomic density
τ	Relaxation time
$\langle v_z^2 \rangle$	Average of the square of the cross-plane group velocities
ω_D	Debye frequency
γ	Grüneisen parameter
C_a	Heat capacity per atom
Λ_{min}	The minimum thermal conductivity
τ_y	Yield strength
l_K	Kapitza length
S	Interface stiffness
σ	Stress
Δu	Discontinuity in displacement
C_i	Elastic constant of an interface
ε	Strain
G_P	Gain of preamplifier
V_0	Average dc voltage
T_m	Melting temperature
α	Thermal expansion coefficient

CHAPTER 1

INTRODUCTION

1.1 Thermal transport

Thermal transport through a material is described by Fourier's law of heat conduction: $\vec{J} = -\Lambda \vec{\nabla} T$, (1.1)

where $\vec{J}$ is the heat flux, $\vec{\nabla} T$ is the temperature gradient across the material, and Λ is the thermal conductivity of the material. For non-metallic materials, thermal energy is predominantly conducted by atomic vibrations. In crystals, these wave-like, collective lattice vibrations are called phonons. Phonons are scattered by crystalline defects, grain boundaries, and anharmonic interactions (e.g., three-phonon scattering) in a material and the mean-free-path, which characterizes the average distance that phonons can travel before being scattered, plays a crucial role in determining the thermal conductivity. Therefore, the basic physical picture of phonon interactions and transport behavior can be revealed through measurements of the thermal conductivity of a material.

Studies of the thermal transport properties could also provide useful guidelines

to design materials with new applications in thermal management. Thermal conductivity is an important factor that affects the performance of thermal devices, e.g., thermoelectric devices, which convert thermal energy into electrical energy [1-3]. Researchers have been able to reduce the thermal conductivity of thermoelectric materials and thereby increase the energy conversion efficiency [4-7].

While heat transport through a bulk material is described by its thermal conductivity, interfaces between two materials generate their own thermal barrier. Thermal transport at interfaces is characterized by the interface thermal conductance G which relates the heat flux across the interface (J) to the finite temperature drop across the interface (ΔT): $J = G\Delta T$. The interface thermal conductance plays an important role in determining the thermal transport behavior in nanomaterials [8] and superlattices [9, 10]. By increasing the density of interfaces in multilayered nanostructures, the thermal conductivity of a bulk material can be substantially decreased because the mismatch in the phonon vibrational density of states and elastic properties of materials at either side of the interface inhibits the transfer of thermal energy across the interface [11, 12].

The physics of phonon transport across interfaces has been studied for decades by measuring the thermal conductance of various interfaces [8, 13-17]. Predictions of conventional models, e.g., acoustic mismatch model and diffuse mismatch model [18],

are often employed to compare with experimental data to gain insights into the interface heat transfer mechanism. However, since these models assume that thermal conductance is only related to physical properties of materials on each side of the interface, interfacial heat transfer by other effects, such as the acoustic and vibrational properties of the interface itself, are not completely clear.

1.2 Varying physical parameters to study thermal transport

By applying external stimuli such as temperature, pressure, or magnetic / electric fields, physical parameters that affect thermal transport, such as heat capacity, elastic constants, or phonon mean-free-path, can be modulated. Of these external stimuli, temperature has been the most studied because of its simplicity to employ and its significant impact on relevant parameters, e.g., phonon mean-free-path and heat capacity. Therefore, measurements of the temperature dependence of thermal conductivity and interface thermal conductance [9, 13, 18-20] can advance understanding of the heat transport mechanism. For example, the observation of a linear temperature dependence in the thermal conductance of an individual single crystalline Si nanowire at low temperatures suggests that the phonon boundary scattering is highly frequency-dependent and ranges from diffusive to specular scattering at the interface [21].

High pressure provides another route to significantly alter the properties of materials. In contrast to temperature, which strongly changes the phonon mean-free-path, applying high pressure to a material has an impact on changing the elastic constants, sound velocities, phonon densities of states, and interface bonding stiffness. Figure 1.1 shows the bulk modulus B_T as a function of pressure for several materials. (The elastic modulus determines the phonon density of states and speed of sound, two important quantities affecting thermal transport properties, and the anharmonicity of a material can be derived from the pressure derivative of the elastic modulus.) For example, the bulk modulus of Al increases from B_T =80 GPa at ambient conditions to B_T =130 GPa at P=10 GPa.

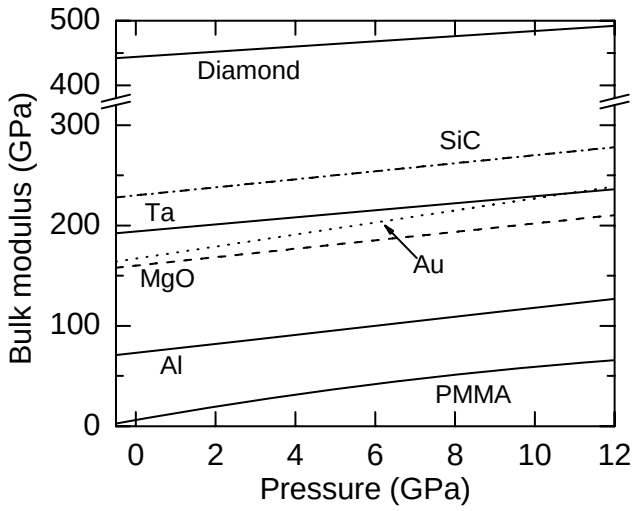

Fig. 1.1. Bulk modulus as a function of pressure for several materials [22-26].

Pressure tuning of physical properties of a material enables critical tests of the validity of conventional models of phonon transport in various condensed matter

systems. For instance, the model of minimum thermal conductivity is often used to predict the minimum thermal conductivity Λ_{min} of amorphous or strongly disordered materials. In the high temperature limit, Λ_{min} can be simplified to be only a function of number density n and elastic constant C_{11} of the material [23]. The application of pressure increases Λ, n and C_{11}. Thus, this model can be tested by comparing measurements of the pressure dependence of thermal conductivity with the predicted Λ_{min}. Details of testing the minimum thermal conductivity model will be presented in Chapter 4. A key component of this thesis will be using in-situ measurements of thermal conductivity and interface thermal conductance under high pressure to elucidate the physics of thermal transport in various materials.

1.3 Reviews of measurements of thermal transport at high pressures

Pressure dependence of the thermal transport in solids [27-31] and amorphous materials [32-35] has been studied for approximately 40 years. One of the conventional approaches to measure the thermal conductivity under pressure is to employ a steady-state technique: samples under study are loaded into a symmetric piston pressure cell with a configuration—*P T S T H T S T P*, where *H* is a heating source embedded in the center of the cell, *T* is the thermocouples to measure the

temperature drop across the sample *S*, and the pressure *P* is applied via two ends of the cylindrical cell [33, 35]. This method was widely used to measure the thermal conductivity of various polymers [33-35] under pressure and the thermal conductivity is obtained by measuring the temperature gradient across the sample combined with the Fourier's law of heat conduction (Eq. 1.1).

Transient techniques, e.g., the hot-wire method, have also been used to measure the thermal conductivity under pressure. For instance, a Ni wire as well as the sample under study are installed in a cylinder cell [36]. The Ni wire is heated electrically at constant power and the temperature change as a function of time is recorded by monitoring the wire resistance via an electronic bridge. The thermal conductivity of the sample can be extracted by comparing the data as a function of time with the temperature evolution calculated using a theoretical model.

The piston-cylinder pressure cell has a limited range of pressure and thus the above techniques can only measure thermal conductivity to a few GPa [31, 32, 37]. For example, the diameter and maximum force of the steel disk used for loading pressure are typically ~10 mm and ~10^5 N [35], which correspond to a pressure of approximately a few GPa. However, pressures of at least 10 to 20 GPa are needed to significantly alter the physical properties that are relevant to thermal transport, e.g., the elastic constants. As shown in Fig. 1.1, creating ≈50 % increase in the bulk

modulus typically requires pressures in excess of 10 GPa. Polymers, such as PMMA, are a special case because their bulk modulus increases by about an order of magnitude when P is increased from ambient conditions to 10 GPa.

Measurements of thermal conductivity at higher pressures, i.e., $P \geq 10$ GPa, are challenging and requires the use of a multi-anvil apparatus or modern gem anvil cells. Thermal diffusivity of silica glass and several minerals, such as olivine and $CaGeO_3$ perovskite, have been measured up to $P \approx 20$ GPa by using the Ångström method within a multi-anvil apparatus [38-40]. The thousand-tons multi-anvil press [41] has been widely used to provide high pressure and high temperature environments; currently the upper limit of the pressure and temperature in multi-anvil press are ≈30 GPa and ≈ 3000 K. The sample under study is encapsulated in a cylindrical tube in which a heater (typically graphite or $LaCrO_3$) is used to heat the sample to high temperatures and a thermocouple wire is embedded in the sample or located next to the sample to measure the temperature. This sample cylinder is then encapsulated in an MgO octahedron with ≈14-25 mm edge length. The high pressure environment is generated by using 6 outer anvil wedges and 8 WC (tungsten carbide) cubic inner anvils with ≈3-10 mm truncated edge length to compress the MgO octahedron containing the sample. Using a loading of 900 tons and inner-anvil with truncated length of 3 mm, a pressure of ≈25 GPa can be achieved [41].

In the Ångström method [40, 42, 43], a sinusoidal temperature wave with an angular frequency is applied by a heater surrounding a cylindrical shape sample and propagates radially into the sample. The amplitude and phase of the varying temperature wave depend on the thermal diffusivity of the sample under study. Therefore, by measuring the amplitude ratio and phase difference of the temperature between two different positions, typically at the center and the outer surface, of the sample, the thermal diffusivity can be obtained. Fig. 1.2 shows the schematic cross-section of the Ångström method within a multi-anvil apparatus [38].

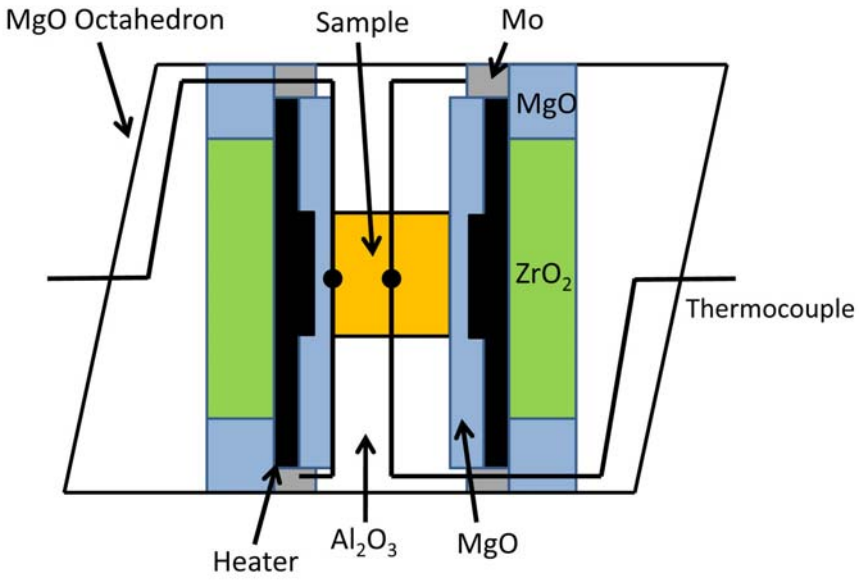

Fig. 1.2. Schematic cross-section of the Ångström method within a multi-anvil apparatus. A cylindrical shape sample (shaded yellow) with diameter of ≈3-4 mm is embedded in the center of the multi-anvil apparatus. The outer case represents the MgO octahedron with ≈14-25 mm edge length. A sinusoidal temperature wave generated by a heater surrounding the cylindrical sample is measured by two thermocouples placed at the center and along the outer surface of the sample, respectively (marked by two black dots) [38].

Diamond anvil cells (DAC) are able to provide even higher pressures because of the much smaller size of sample, ~50 μm, and anvil culet diameter, ≈100-600 μm. To generate pressures higher than 200 GPa, a smaller flat anvil culet which is ≈30 μm in diameter and fabricated on a beveled diamond anvil, is used, see Ref. [44] for the details. The upper limit of the pressure generated by DAC is mainly determined by the size of the small, flat anvil culet fabricated on the beveled diamond anvil.

The optical thermal grating technique [45-47] is compatible with the diamond anvil cell and has been used to measure thermal diffusivity at high pressures. In this technique [46], two mode-locked optical pulses, ≈80 ps duration, are incident on the sample at an angle 2θ to create a constructive interference with periodic distribution of laser intensity. (The sample under study has to be optically absorbing at the laser wavelength energy.) The absorption of the incident light produces a periodic distribution of temperature as well as a periodic distribution of the index of refraction in the sample. The period of the thermal grating $d = \lambda/(2\sin\theta)$, where λ is the laser wavelength. To monitor the temperature evolution as a function of time another Bragg-diffracting probe pulse is incident; if the heat diffusion can be approximated to be one-dimensional, the decay rate of the periodic temperature distribution R_d provides the information about the thermal diffusivity of the sample: $R_d = 4\pi^2 D/d^2$, where D is the thermal diffusivity.

Recently, an optical pulsed transient heating method [48-50] has been developed to measure the thermal diffusivity of several minerals within the diamond anvil cell at pressures as high as 125 GPa. A thin metallic coupler, e.g., Ir or Pt, is embedded in the sample under study; this metallic coupler is heated by a pulsed laser and its surface temperature variation as a function of time is measured by collecting the thermal emission spectrum using an all-reflective microscope. Then the thermal diffusivity of the sample is extracted by fitting the measured temperature evolution to the calculation by a finite element model.

However, the accuracy of this method is not better than ≈50 % because the heat flux model used to extract the thermal diffusivity is insufficient in describing phenomena occurring after the laser heating, such as a non-negligible laser energy absorption in the metallic coupler which reduces the surface temperature of the coupler and is not included in the model calculation. (Typical data measured by this pulsed transient heating technique show a clear discrepancy between the measured temperature and the calculated temperature at the first ≈20 ns, see Ref. [50] for the example data.) Moreover, the transient heating technique can only be applied to study a sample with temperature higher than ≈1400 K since the diagnostics used to measure the temperature of the sample, time-resolved spectroradiometry, only works adequately above 1400 K. (The lower the temperature, the smaller the intensity of

black-body radiation spectrum, which causes the main difficulty in precisely measuring the temperature.)

In contrast to other experimental techniques employed to measure the thermal transport properties of materials at high pressures, time-domain theoreflectance (TDTR), the main technique used in this thesis, has been extensively applied in studies of the thermal conductivity of thin films [11, 51] and thermal conductance of interfaces [15, 52] and its accuracy is typically better than 10%. The details of TDTR will be discussed in Chapter 2. Since the sample dimensions can be as small as the laser spot size (~10 μm), TDTR is much more suitable for measurements of the lattice thermal conductivity in the DAC at extreme pressures [53]. In addition, the combination of TDTR and DAC could be operated, in principle, from a temperature as low as liquid nitrogen to a few thousand Kelvin. The lower and upper limits of the measurement temperature depend on the thermoreflectance and stability of the metal film transducer, respectively.

Figure 1.3 summaries the progress in thermal measurements at high pressures introduced in this section. In the plot, each point labels the first author of the experimental work with the year (x-axis) that the work was published and the highest pressure (y-axis) that was achieved. The table lists the first author, experimental technique, samples, and a reference paper for each point in the plot.

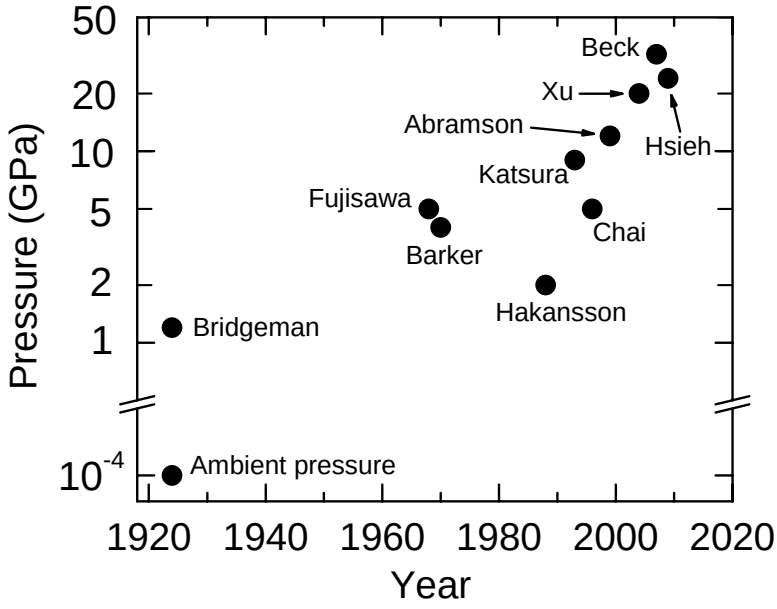

Author(s)	Method	Materials under study	Reference
Bridgeman	Steady-state	Rock and Pyrex glass	Am. J. Sci. 7, 81 (1924)
Fujisawa	Ångström method within a multi-anvil	Mg_2SiO_4, Fe_2SiO_4	J. Geophys. Res. 73, 4727 (1968)
Barker *et al.*	Steady-state	Polytetrafluorethylene	J. Chem. Phys. 53, 2616 (1970)
Hakansson *et al.*	Transient hot-wire	NaCl	Rev. Sci. Instrum. 59, 2269 (1988)
Katsura	Ångström method within a multi-anvil	Silica glass	Phys. Chem. Min. 20, 201 (1993)
Chai *et al.*	Thermal grating	Olivine	Phys. Chem. Miner. 23, 470 (1996)
Abramson et *al.*	Thermal grating	Liquid O_2	J. Chem. Phys. 111, 9357 (1999)
Xu *et al.*	Ångström method within a multi-anvil	Olivine	Phys. Earth Planet. Inter. 143, 324 (2004)
Beck *et al.*	Optical transient heating	MgO, NaCl	Appl. Phys. Lett. 91, 181914 (2007)
Hsieh *et al.*	TDTR	Muscovite mica	Phys. Rev. B 80, 180302 (R) (2009)

Fig. 1.3. Progress in thermal measurements at high pressures.

1.4 Outline of the thesis

In this thesis, I combine an ultrafast pump-probe method, time-domain thermoreflectance, with high-pressure techniques, diamond and SiC anvil cell to investigate the fundamental physics of thermal transport in several materials, e.g., in crystals and amorphous polymers, and across interfaces.

In Chapter 2, I will first describe the main experimental methods I used to conduct experiments: time-domain thermoreflectance (TDTR) and diamond anvil cell (DAC). The novel combination of these two techniques not only provides a powerful approach to study the physics of thermal transport in condensed matter systems, but also opens up a route to measure the thermal transport properties of geophysically important materials, which would help reconstruct the thermal history and geodynamics of our Earth interior.

Chapter 3 presents the first successful combination of TDTR and DAC to study heat transport at high pressures. The dominant mechanism of thermal transport in anisotropic layered crystals is elucidated, and the preliminary result of my measurements of the thermal conductivity of MgO at room temperature up to 60 GPa is also presented.

Testing the validity of the minimum thermal conductivity model for amorphous polymers using high pressure is described in Chapter 4. I study the

pressure dependence of the thermal conductivity $\Lambda(P)$ and elastic constant C_{11} of the poly(methyl methacrylate) (PMMA). The good agreement between my measurements and the prediction of $\Lambda(P)$ based on the minimum thermal conductivity model confirms that the dominant thermal transport mechanism in amorphous polymers is the thermal energy exchange between non-propagating vibrational modes of polymers.

In Chapter 5, I demonstrate the importance of interface stiffness on the thermal transport across interfaces by measuring the pressure dependence of the thermal conductance $G(P)$ of various Al/SiC interfaces. I find that in the low pressure regime the $G(P)$ of weak interfaces increases approximately linearly with pressure; when P>8 GPa, $G(P)$ saturates at the values for strong interfaces. Conventional DMM fails to describe the strong pressure dependence of the $G(P)$ of weak interfaces until pressures are large enough for the interface stiffness to approach the values more typical of the stiffness of chemical bonding.

In Chapter 6, I study the critical factors in TDTR measurements, i.e., the thermoreflectance, piezo-optical coefficient, and physical stability of metal transducers, under pressure. Ta and Au with 5 at. % Pd can replace Al as the metal film transducers for TDTR measurements at high pressure and temperature. Finally, the Chapter 7 summarizes the whole thesis work.

1.5 References

[1] G. J. Snyder, and E. S. Toberer, Nat Mater **7**, 105 (2008).

[2] B. C. Sales, Mrs Bull **23**, 15 (1998).

[3] B. C. Sales, D. Mandrus, B. C. Chakoumakos, V. Keppens, and J. R. Thompson, Phys. Rev. B **56**, 15081 (1997).

[4] T. C. Harman, P. J. Taylor, M. P. Walsh, and B. E. LaForge, Science **297**, 2229 (2002).

[5] A. I. Hochbaum, R. K. Chen, R. D. Delgado, W. J. Liang, E. C. Garnett, M. Najarian, A. Majumdar, and P. D. Yang, Nature **451**, 163 (2008).

[6] K. F. Hsu, S. Loo, F. Guo, W. Chen, J. S. Dyck, C. Uher, T. Hogan, E. K. Polychroniadis, and M. G. Kanatzidis, Science **303**, 818 (2004).

[7] R. Venkatasubramanian, E. Siivola, T. Colpitts, and B. O'Quinn, Nature **413**, 597 (2001).

[8] D. G. Cahill, W. K. Ford, K. E. Goodson, G. D. Mahan, A. Majumdar, H. J. Maris, R. Merlin, and S. R. Phillpot, J. Appl. Phys. **93**, 793 (2003).

[9] Y. K. Koh, Y. Cao, D. G. Cahill, and D. Jena, Adv. Funct. Mater. **19**, 610 (2009).

[10] V. Samvedi, and V. Tomar, Nanotechnology **20**, 365701 (2009).

[11] R. M. Costescu, D. G. Cahill, F. H. Fabreguette, Z. A. Sechrist, and S. M. George,

Science **303**, 989 (2004).

[12] S. T. Huxtable, A. R. Abramson, C. L. Tien, A. Majumdar, C. LaBounty, X. Fan, G. H. Zeng, J. E. Bowers, A. Shakouri, and E. T. Croke, Appl. Phys. Lett. **80**, 1737 (2002).

[13] R. J. Stoner, and H. J. Maris, Phys. Rev. B **48**, 16373 (1993).

[14] R. M. Costescu, M. A. Wall, and D. G. Cahill, Phys. Rev. B **67**, 054302 (2003).

[15] H. K. Lyeo, and D. G. Cahill, Phys. Rev. B **73**, 144301 (2006).

[16] B. C. Gundrum, D. G. Cahill, and R. S. Averback, Phys. Rev. B **72**, 245426 (2005).

[17] D. A. Young, and H. J. Maris, Phys. Rev. B **40**, 3685 (1989).

[18] E. T. Swartz, and R. O. Pohl, Rev. Mod. Phys. **61**, 605 (1989).

[19]D. Y. Li, Y. Y. Wu, P. Kim, L. Shi, P. D. Yang, and A. Majumdar, Appl. Phys. Lett. **83**, 2934 (2003).

[20] D. G. Cahill, and R. O. Pohl, Phys. Rev. B **35**, 4067 (1987).

[21] R. Chen, A. I. Hochbaum, P. Murphy, J. Moore, P. D. Yang, and A. Majumdar, Phys. Rev. Lett. **101**, 105501 (2008).

[22] C. Bercegeay, and S. Bernard, Phys. Rev. B **72**, 214101 (2005).

[23] W. P. Hsieh, M. D. Losego, P. V. Braun, S. Shenogin, P. Keblinski, and D. G. Cahill, Phys. Rev. B **83**, 174205 (2011).

[24] C. H. Park, B. H. Cheong, K. H. Lee, and K. J. Chang, Phys. Rev. B **49**, 4485 (1994).

[25] C. S. Zha, H. Mao, and R. J. Hemley, PNAS, USA **97**, 13494 (2000).

[26] J. J. Xie, S. P. Chen, J. S. Tse, S. de Gironcoli, and S. Baroni, Phys. Rev. B **60**, 9444 (1999).

[27] A. M. Hofmeister, PNAS, USA **104**, 9192 (2007).

[28] D. Gerlich, J. Phys. C-Solid State Phys. **15**, 4305 (1982).

[29] D. Gerlich, and P. Andersson, J. Phys. C-Solid State Phys. **15**, 5211 (1982).

[30] S. W. Kieffer, J. Geophys. Res. **81**, 3025 (1976).

[31] S. W. Kieffer, I. C. Getting, and G. C. Kennedy, J. Geophys. Res. **81**, 3018 (1976).

[32] S. P. Andersson, and R. G. Ross, Int. J. Thermophys. **15**, 949 (1994).

[33] R. E. Barker, R. Y. S. Chen, and R. S. Frost, J. Polymer Sci. B-Polymer Phys. **15**, 1199 (1977).

[34] R. S. Frost, R. Y. S. Chen, and R. E. Barker, J. Appl. Phys. **46**, 4506 (1975).

[35] R. E. Barker, and R. Y. S. Chen, J. Chem. Phys. **53**, 2616 (1970).

[36] B. Hakansson, P. Andersson, and G. Backstrom, Rev. Sci. Instrum. **59**, 2269 (1988).

[37] R. G. Ross, P. Andersson, B. Sundqvist, and G. Backstrom, Rep. Prog. Phys. **47**,

1347 (1984).

[38] M. A. G. M. Manthilake, N. de Koker, and D. J. Frost, Geophys. Res. Lett. **38**, L08301 (2011).

[39] Y. S. Xu, T. J. Shankland, S. Linhardt, D. C. Rubie, F. Langenhorst, and K. Klasinski, Phys. Earth Planet. Inter. **143-44**, 321 (2004).

[40] T. Katsura, Phys. Chem.Min. **20**, 201 (1993).

[41]D. J. Frost, B. T. Poe, R. G. Tronnes, C. Liebske, A. Duba, and D. C. Rubie, Phys. Earth Planet. Inter. **143-44**, 507 (2004).

[42] H. Fujisawa, N. Fujii, H. Mizutani, H. Kanamori, and S. I. Akimoto, J. Geophys. Res. **73**, 4727 (1968).

[43] T. Katsura, Geophys. J. Int **122**, 63 (1995).

[44] W. L. Mao, H. K. Mao, C. S. Yan, J. F. Shu, J. Z. Hu, and R. J. Hemley, Appl. Phys. Lett. **83**, 5190 (2003).

[45] E. H. Abramson, J. M. Brown, and L. J. Slutsky, J. Chem. Phys. **115**, 10461 (2001).

[46] E. H. Abramson, L. J. Slutsky, and J. M. Brown, J. Chem. Phys. **111**, 9357 (1999).

[47] M. Chai, J. M. Brown, and L. J. Slutsky, Phys. Chem. Miner. **23**, 470 (1996).

[48] P. Beck, A. F. Goncharov, V. V. Struzhkin, B. Militzer, H. K. Mao, and R. J.

Hemley, Appl. Phys. Lett. **91**, 181914 (2007).

[49] A. F. Goncharov, P. Beck, V. V. Struzhkin, B. D. Haugen, and S. D. Jacobsen, Phys. Earth Planet. Inter. **174**, 24 (2009).

[50] A. F. Goncharov, V. V. Struzhkin, J. A. Montoya, S. Kharlamova, R. Kundargi, J. Siebert, J. Badro, D. Antonangeli, F. J. Ryerson, and W. Mao, Phys. Earth Planet. Inter. **180**, 148 (2010).

[51] C. Chiritescu, D. G. Cahill, N. Nguyen, D. Johnson, A. Bodapati, P. Keblinski, and P. Zschack, Science **315**, 351 (2007).

[52] Z. B. Ge, D. G. Cahill, and P. V. Braun, Phys. Rev. Lett. **96**, 186101 (2006).

[53] W. P. Hsieh, B. Chen, J. Li, P. Keblinski, and D. G. Cahill, Phys. Rev. B **80**, 180302 (2009).

CHAPTER 2

EXPERIMENTAL TECHNIQUES

2.1 Time-domain Thermoreflectance (TDTR)

2.1.1 TDTR apparatus and data analysis

Time-domain thermoreflectance (TDTR) is an ultrafast optical pump-probe technique which utilizes the output of a femtosecond, mode-locked Ti:sapphire laser to both generate surface heating and probe the resultant temperature evolution on a metal film through the use of the change in optical reflectivity with temperature, known as thermoreflectance dR/dT [1, 2]. The concept of using transient thermoreflectance to study thermal transport properties of materials was proposed and realized approximately 25 years ago [3, 4]. However, more recently Cahill *et al.* [1, 5] made improvements which take advantage of the out-of-phase component of the thermoreflectance signals to improve the accuracy of TDTR. TDTR has since been widely employed to measure the thermal conductivity [6, 7] and the interface thermal conductance [8, 9]. Figs. 2.1(a) and (b) show the setup and the schematic layout of the TDTR system at the University of Illinois.

To perform thermal measurements using TDTR, a thin metal film, typically ≈80 nm-thick Al, is first deposited on the sample of interest using magnetron

(a)

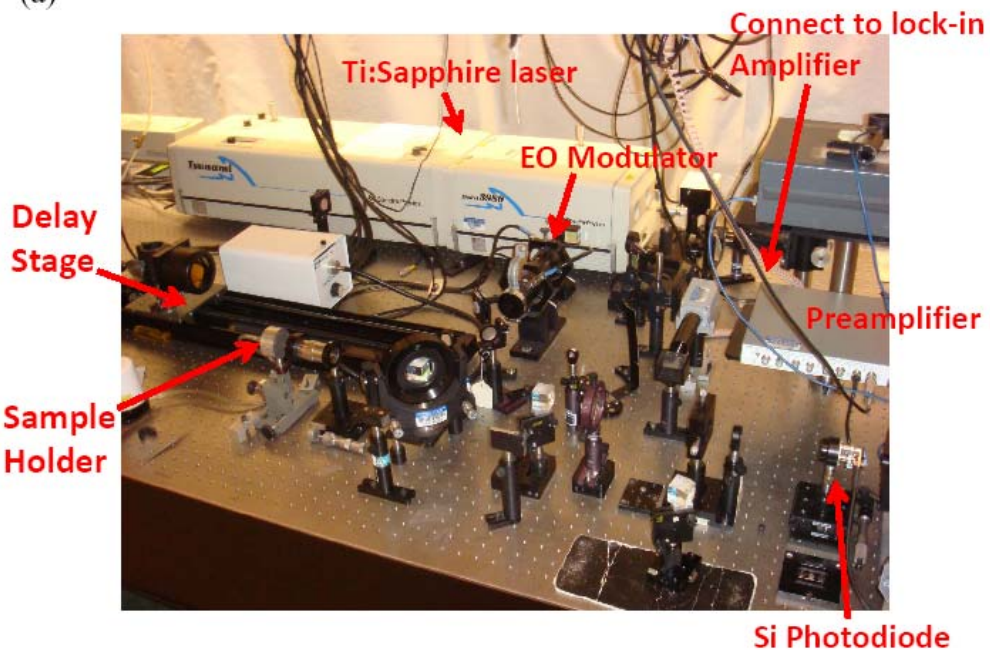

(b)

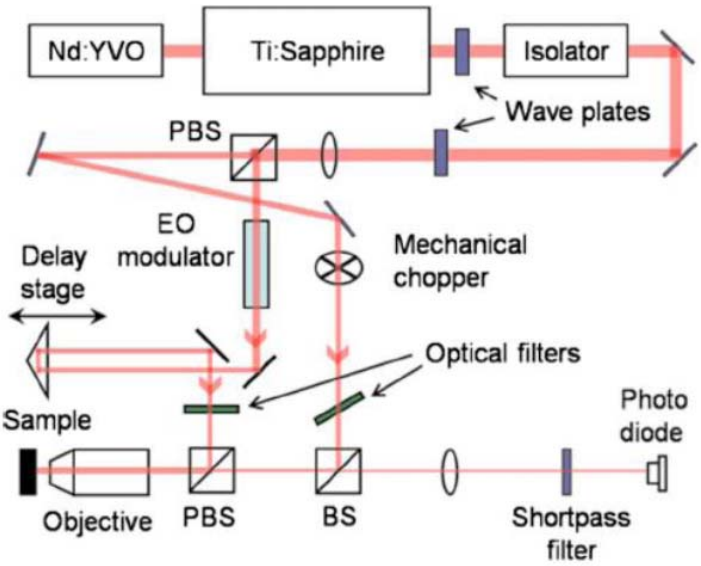

Fig. 2.1. (a) Time-domain thermoreflectance (TDTR) setup at the University of Illinois. **(b)** Schematic layout of TDTR [2].

sputtering and serves as both the light absorber and thermoreflectance transducer. Al is the typical metal film transducer due to its large thermoreflectance at Ti:sapphire laser wavelengths (~785 nm). Large thermal conductivity, large piezo-optical coefficient, and good adhesion to substrates are other useful features for Al being an ideal thermal transducer in TDTR measurements. Large thermal conductivity ensures that after the pump pulse heating, the temperature evenly distributes over the metal film within ~100 ps; beyond this time, the measurement becomes insensitive to the thermal conductivity of metal film transducer and thus does not significantly propagate error to the measured thermal conductivity of the sample under study, see section 2.1.3 for the estimation of uncertainties in the TDTR measurements. Large piezo-optical coefficient, which describes the changes in the optical reflectivity with acoustic strain, is useful to determine the thickness of the metal film.

In the TDTR system, the output of a femtosecond mode-locked Ti:sapphire laser with repetition rate of ≈80 MHz is split into pump and probe beams by a polarized beam splitter. The pump beam, modulated at ≈10 MHz by an electro-optical modulator, passes through a mechanical delay stage which adjusts the relative delay time t between pump and probe beams (typically -20 ps $\leq t \leq$ 4 ns), and is focused on the surface of the sample by an objective lens. (The laser beam is focused to $1/e^2$ intensity radius of ≈7.5 μm by the 10× objective lens and ≈15 μm by the 5× objective lens.) The probe beam is mechanically chopped at ≈200 Hz for double modulation [2], and is also focused on the sample by the same objective. The double modulation is used to suppress the artifacts that occur at the same frequency as the modulation of

the pump beam, such as diffuse pump scattering and unfiltered pump-light, see Ref. [2] for the details.

The temperature evolution at the Al surface is probed as a function of time by measuring changes in the intensity of the reflected probe pulse by a Si photodiode detector. A resonant band-pass filter with a quality factor $Q \approx 10$ is used to enhance the output of the Si photodiode as well as to eliminate the higher, odd harmonic signals. The signal is then further enhanced by a preamplifier with a voltage gain of 5 and measured by a radio-frequency (rf) lock-in amplifier that is set to be synchronized to the modulation frequency of the pump beam, 10 MHz. (The 10 MHz modulation frequency is chosen since under a laser repetition rate of 80 MHz, the real part of the changes in the optical reflectivity is minimized at negative delay times [1].)

To increase the signal-to-noise ratio and prevent the Si photodiode detector from collecting diffuse scattering of the pump pulse due to the unfocused reflection from the interface of SiC and air, in addition to the double modulation technique, a "two-tint" method is used [2]. In this configuration, a 790 nm long-pass filter is placed in the path of the pump beam, and a 785 nm band-pass filter with a bandwidth of 3 nm is placed in the path of the probe beam and is rotated by ≈13° to blue-shift the peak wavelength to ≈781 nm. As a result, the peak wavelength of pump and probe beams after the optical filters are separated by ≈10 nm. Finally, a 780 nm short-pass filter is placed in front of the Si photodiode detector to filter out the diffusively scattered pump beam signals. The diffuse pump light scattered from the rough surface of sample is then suppressed by an extra three orders of magnitude [2].

The steady-state temperature rise ΔT_s at the surface of Al due to the pump pulse heating is given by [1]

$$\Delta T_s = \frac{P_i(1-R)}{2\sqrt{\pi} w_0 \Lambda} \quad , \qquad (2.1)$$

where P_i is the incident laser power, R is the optical reflectivity of metal film, w_0 is the spot size of pump and probe beams focused on the surface of sample, and Λ is the thermal conductivity of the sample. Typically a 20 mW of pump beam is used, which corresponds to an energy of ≈500 pJ per pulse, and a 10 mW of probe beam to limit the ΔT_s on the Al surface to be < 10 K. (The ratio of the power of pump beam to probe beam does not necessarily need to be 2:1 [10], see section 2.1.2.) For instance, with the incident pump power P_i =20 mW, R=0.9 for Al, the thermal conductivity Λ of Si =142 W m^{-1} K^{-1} and w_0 =7.5 μm, the steady-state temperature rise for Al on Si under these conditions is ΔT_s =0.5 K. By contrast, in muscovite mica, the cross-plane thermal conductivity $\Lambda_\perp$ is only 0.46 W m^{-1} K^{-1} and the in-plane thermal conductivity $\Lambda_\parallel$ is 4 W m^{-1} K^{-1}. The steady-state temperature rise under the same conditions as before is ΔT_s ≈55 K, which increases the measurement temperature from room temperature to 355 K. (For a material with anisotropic thermal conductivity, a geometric mean of the in-plane and cross-plane thermal conductivities $\Lambda = \sqrt{\Lambda_\parallel \Lambda_\perp}$ is used in the calculation in Eq. 2.1.) Note that the thermal conductivity of muscovite changes by less than 4% when the measurement temperature changes from 300 K to 355 K [11].

The depth that the thermal energy can propagate into the sample determines the geometry of the heat flow in my experiments: the thermal penetration depth d_{th},

which characterizes the temperature excursion in the sample, is given by

$$d_{th} = \sqrt{\frac{\Lambda}{\pi C_s f}} \quad , \qquad (2.2)$$

where Λ is the thermal conductivity and C_s is the volumetric heat capacity of the sample, f is the modulation frequency of the pump beam. For example, if Λ=10 W $m^{-1} K^{-1}$, C_s=1.5 J $cm^{-3} K^{-1}$, and f=10 MHz, d_{th}≈460 nm. Since the thermal penetration depth d_{th} is typically much smaller than the radius of laser beams after focused on the sample surface (≈7.5 μm for 10× objective and ≈15 μm for 5× objective), heat flow in TDTR measurements is predominantly one dimensional.

To extract the thermal transport properties of the sample under study, I analyze the output of the rf lock-in amplifier $V(t)$ which has an in-phase component $V_{in}(t)$ and an out-of-phase component $V_{out}(t)$, $V(t)= V_{in}(t)+iV_{out}(t)$, where t is the delay time between pump and probe beams. Although the $V_{out}(t)$ signal provides most of the useful information about the thermal conductivity of the sample (at 100 ps$\le t \le$500 ps, $V_{out}(t)$ is approximately proportional to $1/\sqrt{\Lambda C}$, where $\sqrt{\Lambda C}$ is the thermal effusivity of the sample), I analyze the ratio $V_{in}(t)/V_{out}(t)$ which eliminates undesirable artifacts due to the variation of laser spot size and the change in the position of pump beam during the scanning of mechanical delay stage.

2.1.2 Thermal model and data analysis

Thermal conductivity of the sample is determined by comparing the measured ratio $V_{in}(t)/V_{out}(t)$, where 80 ps$\le t \le$4 ns, to the ratio calculated from an exact

numerical solution to the heat diffusion equation for a multilayered structure in cylindrical coordinates [1]. In the thermal model, two boundary conditions are imposed: (1) a pump pulse with the Gaussian spatial distribution of intensity periodically heats the surface of the sample and (2) the heat flows continuously across each interface. Interface thermal conductance is introduced between each layer by an additional interface between each layer, modeled as a thin layer with thickness h_i =1 nm and a non-zero, small volumetric heat capacity C_i =0.1 J cm^{-3} K^{-1}. The thickness of 1 nm is chosen for convenience; the interface thermal conductance given by the thermal conductivity per unit thickness of the interface layer does not change if different thicknesses are used. The heat capacity of 0.1 J cm^{-3} K^{-1} is used such that the interface layer does not absorb significant heat. The detailed description of the thermal model is given in Ref.[1].

There are many parameters in the thermal model: (1) laser spot size w_0, (2) modulation frequency of the pump beam f =10 MHz, (3) repetition rate of the laser oscillator, 80 MHz, (4) thickness h_{Al}, volumetric heat capacity C_{Al} and thermal conductivity Λ_{Al} of Al, (5) thermal conductance G of Al/sample interface, (6) thermal conductivity and volumetric heat capacity of the sample. (When studying a thin film sample which is sandwiched between Al and a substrate, the sample is modeled as a thin layer. Therefore, thickness of the thin film sample and thermal conductivity and volumetric heat capacity of the substrate are also input parameters in the thermal model.)

All of these parameters are either obtained from the literatures or independently measured. For instance, the thicknesses of Al and thin film sample are measured by picosecond acoustics [12] which will be described in the section 2.1.5; the thermal conductivity of Al is obtained by the four-point probe measurements of the in-plane electrical conductivity combined with the Wiedemann-Franz law. The thermal model is not necessarily sensitive to all of these parameters, however.

In general, the thermal conductance G of Al/sample interface and the thermal conductivity Λ of the sample, the two free parameters during the thermal model fitting, can be separated and derived at different delay time regimes. At 100 ps $\leq t \leq$ 500 ps, the ratio $V_{in}(t)/V_{out}(t)$ is more sensitive to the Λ of the sample; at longer delay time, i.e., $t \geq$ 1 ns, $V_{in}(t)/V_{out}(t)$ has stronger dependence on the G of Al/sample interface. (For the definition of sensitivity and how these free parameters affect TDTR measurements, see section 2.1.3 and Fig. 2.3.) Example data and fittings by the thermal model are shown in Fig. 2.2.

In the section 2.1.1, it was stated that the ratio of the incident power of pump beam to probe beam does not necessarily need to be 2:1. I used ratios of 5:1, 2:1, and 1:1 to measure the thermal conductivity of muscovite mica and did not observe any difference in the measured thermal conductivity. A similar result was also mentioned in Ref. [10]. This is because when the ratio $V_{in}(t)/V_{out}(t)$ is used to analyze the data, the incident laser power and ratio of the pump and probe beams are not parameters in the thermal model. Note, however, that the signal-to-noise ratio is improved when a large ratio of the power of pump beam to probe beam is used, such as 5:1 or 10:1.

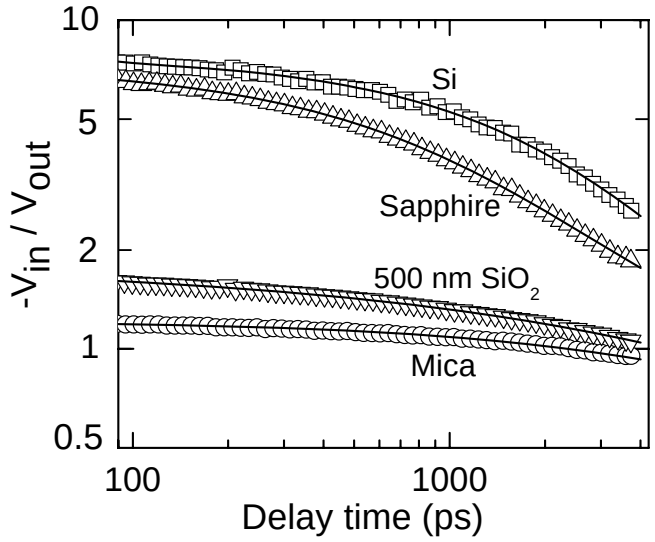

Fig. 2.2. Ratio of the in-phase voltage to the out-of-phase voltage $V_{in}(t)/V_{out}(t)$ as a function of delay time for Si, sapphire, 500 nm SiO_2, and mica. The solid lines are the fits by the thermal model to the data. In these TDTR measurements, the thickness, volumetric heat capacity, and thermal conductivity of Al are ≈80-90 nm, 2.44 J cm^{-3} K^{-1}, and 200 W m^{-1} K^{-1}, respectively; the laser spot size is ≈7.5 μm. The heat capacities of 1.62 J cm^{-3} K^{-1} for Si, 3.19 J cm^{-3} K^{-1} for sapphire, 1.64 J cm^{-3} K^{-1} for SiO_2, and 2.3 J cm^{-3} K^{-1} for mica are used to analyze the data. Thermal conductivities of Si, sapphire, 500 nm SiO_2, and mica are determined to be 140 W m^{-1} K^{-1}, 35 W m^{-1} K^{-1}, 1.32 W m^{-1} K^{-1}, and 0.46 W m^{-1} K^{-1}, respectively.

2.1.3 Estimation of uncertainties in the TDTR measurements

To estimate uncertainties in the TDTR measurements, it is helpful to calculate the sensitivity parameter [13], defined as:

$$S_\alpha = \frac{\partial \ln(-V_{in}/V_{out})}{\partial \ln \alpha} \quad , \quad (2.3)$$

where $-V_{in}/V_{out}$ is the ratio of the in-phase to out-of-phase voltages in TDTR measurements, α is one of the parameters in the thermal model described above, e.g., laser spot size, thickness h_{Al}, volumetric heat capacity C_{Al} and thermal conductivity Λ_{Al} of Al, and thermal conductivity of substrate. Fig. 2.3 shows the calculated S_α for

each parameter in the thermal model. For an example sample of Al on Si substrate, at 100 ps $\leq t \leq$ 500 ps, the ratio, $-V_{in}/V_{out}$, is sensitive to the thickness h_{Al} and heat capacity C_{Al} of Al film as well as the thermal conductivity Λ_{Si} and heat capacity C_{Si} of Si. At $t \geq 1$ ns, the ratio, $-V_{in}/V_{out}$, is more sensitive to the thermal conductance G of Al/Si interface.

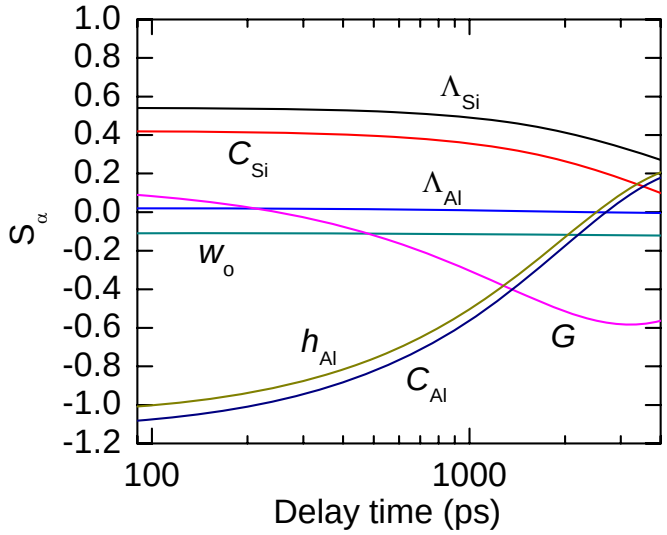

Fig. 2.3. Calculated sensitivity parameter S_α for each parameter in the thermal model. An example sample of Al on Si substrate is considered in this calculation: the thickness h_{Al}, heat capacity C_{Al}, and thermal conductivity Λ_{Al} of Al are 80 nm, 2.44 J cm^{-3} K^{-1}, and 200 W m^{-1} K^{-1}, respectively; the heat capacity C_{Si} and thermal conductivity Λ_{Si} of Si are 1.62 J cm^{-3} K^{-1} and 142 W m^{-1} K^{-1}, respectively. Thermal conductance G of Al/SiC interface is 160 MW m^{-2} K^{-1} and laser spot size is w_0 =7.5 μm. The larger the absolute value of S_α, the more sensitive the parameter to the ratio, $-V_{in}/V_{out}$.

The accuracy of the thermal measurements is limited by the uncertainties in all the parameters in the thermal model. With the calculation of S_α for each parameter, the error in the thermal conductivity measurements Δ_Λ that is caused by the uncertainty Δ_α from a parameter α : $\Delta_\Lambda = \Delta_\alpha S_\alpha / S_\Lambda$ can be estimated. For example, at

100 ps $\leq t \leq$ 500 ps, the sensitivity for thermal conductivity of Si is $S_{\Lambda} \approx 0.55$ and the sensitivity for the thickness of Al is $S_{hAl} \approx 0.9$; if the uncertainty in the Al thickness Δ_{hAl} is 3 % , it will propagate ≈5 % error in the measured thermal conductivity of Si.

The total error in the measured thermal conductivity of sample can be estimated by the square root of the sum of the squares of errors caused by uncertainties in each parameter. Assuming 3 % uncertainties in all the parameters, such as the thickness and heat capacity of Al and heat capacity of Si, the total error in the thermal conductivity of Si is estimated to be ≈7.5 %.

2.1.4 Time-domain stimulated Brillouin scattering

The elastic constants or speed of sound of materials are often measured by Brillouin scattering, inelastic light scattering from acoustic modes. The frequency shift of the scattered light is called the Brillouin frequency f_B.

TDTR also provides *in situ* measurements of the elasticity and speed of sound of transparent materials through time-domain stimulated Brillouin scattering, also called picosecond interferometry [14, 15]. Figure 2.4 illustrates the principle of time-domain stimulated Brillouin scattering. In TDTR measurements, after the pump pulse heats the Al film, the thermal expansion of Al generates a longitudinal acoustic strain pulse propagating in the transparent sample. Part of the subsequent incident probe pulse reflecting from this moving acoustic strain wave interferes with the remainder of the probe pulse reflecting from the Al film. The position of the moving strain determines the optical path difference between these two reflected probe pulses

and therefore determines the interference is constructive or destructive. When the interference is coherent, a periodic oscillation of the $V_{in}(t)$ signal will be observed. The period (inverse of the Brillouin frequency) of the oscillatory $V_{in}(t)$ signal provides the information about the speed of sound of the sample.

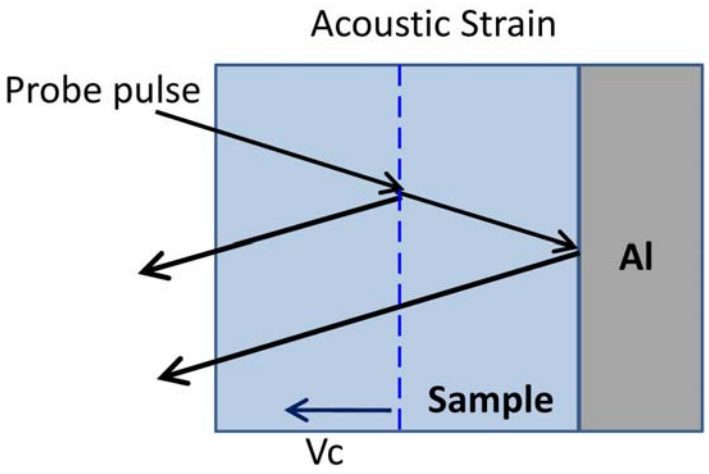

Fig. 2.4. Schematic illustration of the time-domain stimulated Brillouin scattering. A longitudinal acoustic strain (dashed line) is generated by the thermal expansion of Al and propagates in the transparent sample. Part of the incident probe pulse reflecting from this moving acoustic strain wave interferes with the remainder of the probe pulse reflecting from the Al film. The *V*c denotes the speed of sound of the sample.

In my experiments, the pump and probe beams are focused by a 10× objective lens with a numerical aperture of 0.28 and incident on the sample by an angel θ of ≈16° from the sample surface normal (θ=0° for the normal incident). If the Brillouin scattering is approximated as being in a backscattering geometry with normal incident of laser beam, the Brillouin frequency f_B in the longitudinal modes is $f_B = 2Nv_l / \lambda$, where N is the index of refraction of the sample, v_l the longitudinal speed of sound, and λ the laser wavelength. This approximation introduces ≈3-4 % error in the measured f_B. Once f_B, N, and λ are known, v_l and the corresponding elastic constant

of the sample can be obtained.

Traditional techniques for measuring elasticity, such as Brillouin spectroscopy [16] and impulsive stimulated light scattering [17], are time-consuming (minutes to hours of accumulation time). By contrast, the picosecond interferometry of TDTR takes much less time (only few minutes) to probe the longitudinal sound velocity with high accuracy.

2.1.5 Picosecond acoustics

The acoustic properties or thickness of a material can be characterized by picosecond acoustics using TDTR [12]. As described in the section 2.1.4 time-domain stimulated Brillouin scattering, when the pump pulse heats the Al film coated on a substrate, the thermal expansion of Al creates a longitudinal strain pulse. This strain wave propagates through the metal film and partially reflects at the interface between Al and the substrate. As the reflected strain pulse returns back to the Al surface, it changes the optical reflectivity of the Al film. Thus, by multiplying the average longitudinal speed of sound of Al, v_l = 6.42 nm ps^{-1}, by half of this acoustic echo time, the thickness of Al is determined. Example data for the Al on Si wafer and Al on mica are shown in Fig. 2.5. The acoustic echo peak at t= 36.2 ps for Al/Si and t= 24.1 ps for Al/mica are observed; therefore, the Al thicknesses h_{Al} are determined to be 116 nm and 77 nm, respectively.

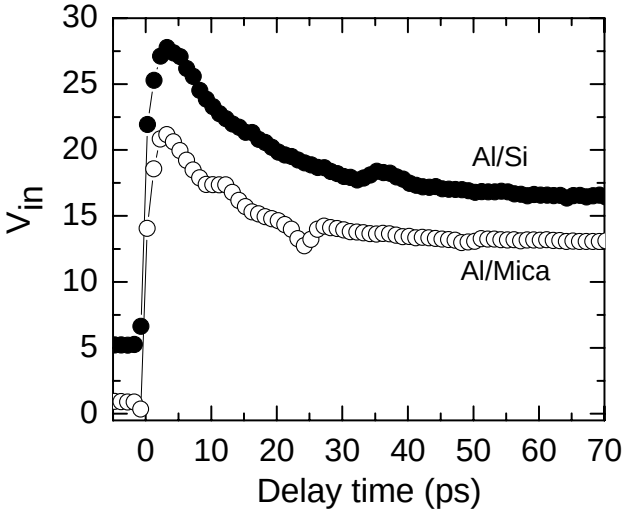

Fig. 2.5. Example data for the acoustic signals of Al on Si and Al on mica. $V_{in}(t)$ is proportional to the changes in the optical reflectivity of the Al surface. The acoustic echo peak at t=36.2 ps for Al/Si corresponds to h_{Al}=116 nm and the acoustic echo at t=24.1 ps for Al/mica corresponds to h_{Al}=77 nm. The acoustic echoes of Al/Si and Al/mica have opposite signs because the acoustic impedance, product of atomic density and speed of sound, of Al is smaller than that of Si but larger than mica. $V_{in}(t)$ of Al/Si is up-shifted for clarity.

A computer code is also used to simulate the acoustic signals. The program is based on Ref. [12] and provided by Prof. H. Maris of Brown University. There are several parameters in the program: (1) laser wavelength of pump and probe beams; (2) thickness, atomic density, sound velocity, index of refraction, and diffusion length of each layer. (The diffusion length characterizes the distance that the deposited heat extends in the material [18].) For a multilayered sample structure, this simulation program is particularly helpful to identify acoustic echoes in the picosecond acoustics data. For example, Fig. 2.6 shows the acoustic signals of an Al-coated poly(methyl methacrylate) (PMMA) on a SiC substrate. The open circles represent the acoustic signals measured by piscosecond acoustics and the red curve shows the simulation

results. As an acoustic strain propagates through the Al film and arrives at the interface of Al and PMMA layer, part of the acoustic strain reflects back toward the Al surface and the remainder of the strain continues to propagate into the PMMA layer and then reflects at the interface of PMMA and SiC. In Fig. 2.6, the downward peak at t=20.2 ps is caused by the acoustic strain reflecting from the Al/PMMA interface and therefore the thickness of Al is determined to be h_{Al}=65 nm. Compared to the strain reflecting from the Al/PMMA interface, the strain propagating through the PMMA and reflecting back at the PMMA/SiC interface propagates an additional distance, i.e., twice of the thickness of PMMA layer. By comparing the data with simulation results,

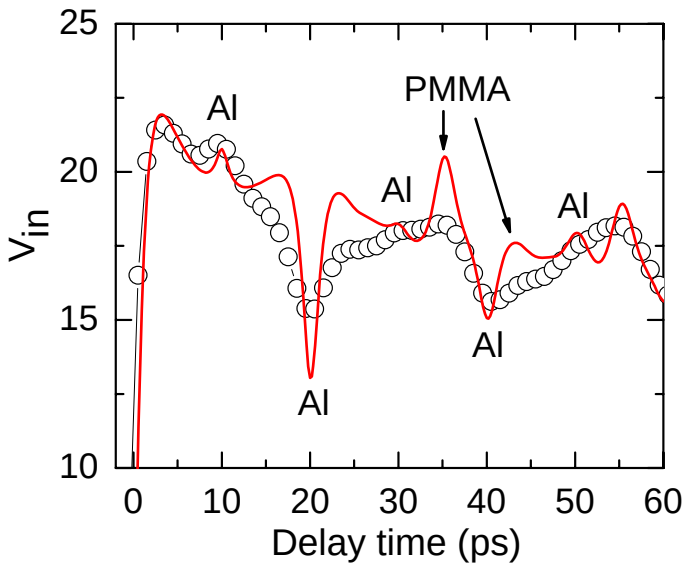

Fig. 2.6. Example data for the acoustic signals of an Al-coated PMMA on SiC. The open circles show the picosecond acoustics data and the red curve shows the acoustic signals simulated by the program. The thickness of Al is determined by the acoustic echo at t=20.2 ps, corresponding to h_{Al}=65 nm; the echo at t=35.3 ps is caused by a strain reflecting from the PMMA/SiC interface and returning back to the Al surface. The thickness of PMMA is h_{PMMA}=22 nm. Note that the acoustic echo at t=10.1 ps is caused by acoustic strain waves launched from the Al surface which contacts with the PMMA layer. Such acoustic strain wave is generated by hot electrons that diffuse through the Al film before losing energy to phonons.

the acoustic echo at t=35.3 ps is confirmed to be caused by the strain which reflects at the PMMA/SiC interface and returns back to the Al surface; therefore the thickness of PMMA h_{PMMA} is determined by multiplying the speed of sound of PMMA, v_l = 2.9 nm ps^{-1}, by half of the time difference between the echo of Al (t=20.2 ps) and PMMA (t=35.3 ps).

2.2 Generating high pressures: Diamond Anvil Cell (DAC)

2.2.1 Fundamental aspects of DAC

High pressure environment can be generated by either static or dynamic loading. Shock waves are able to provide dynamic compression to pressures as high as the conditions in Earth's core [19]; however, this approach is severely limited by the short duration time on the order of milliseconds. Diamond anvil cell (DAC) is a powerful and commonly used technique generating static high pressures above 100 GPa [20-24]. In this thesis, all the high pressure experiments were conducted using diamond or SiC anvil cells. Fig. 2.7 shows two types of cells used in this thesis.

Figure 2.8 shows the principle of the diamond anvil cell: an external force is applied on the large table facets of two opposing diamonds which will transmit the force directly to their small culet facets, typically ≈500 μm or smaller, creating a pressure $P=F/A$, where F is the external force and A is the area of the small culet. Pressures of few gigapascal can be easily generated by a pair of diamond or SiC anvils with the culet size of 500 μm.

Fig. 2.7. Two types of the opposing-plate diamond and SiC anvil cells used in this thesis work. A penny is included as the scale bar of anvil cells.

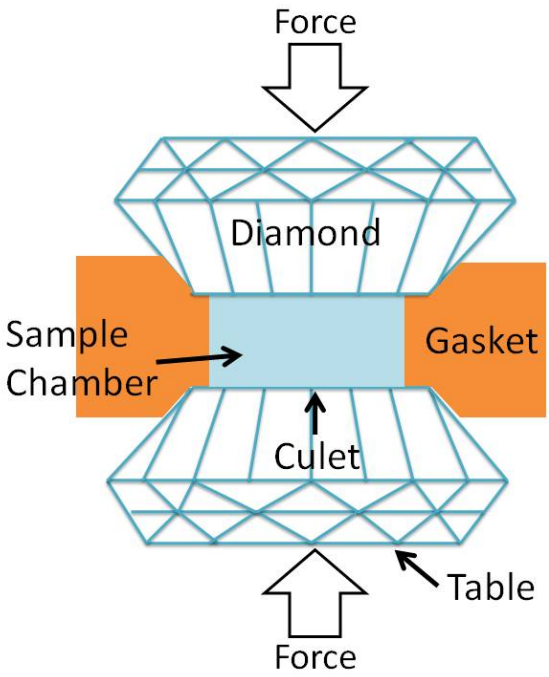

Fig. 2.8. Schematic drawing of the configuration of opposing-plate diamond anvil cell.

Diamond has excellent mechanical and optical properties for optical measurements under high pressure. For example, diamond is the hardest material and is transparent in a wide range of the electromagnetic spectrum which enables *in situ* measurements using X-ray, visible light, and infra-red. Therefore, diamond anvil is the ideal candidate to be used to create high pressure environments.

SiC is another material widely used in the high pressure anvil cell and is also transparent in a wide range of the electromagnetic spectrum. In this dissertation, I show that interesting physics of thermal transport can be observed during the pressure range created by SiC anvil cell, i.e., $0<P<12$ GPa. As a practical matter, SiC anvils are much less expensive than the diamond anvils, typically by a factor of 10 for the same weight of anvil. A 1/3 carat SiC anvil manufactured by Charles & Colvard Ltd. costs ≈ $110.

2.2.2 Preparation of the high pressure cell

Figure 2.9 summaries the procedure for preparing the high pressure cell. To prepare the high pressure cell, epoxy was used to mount a pair of diamond or SiC anvils on backing plates (seats) that are made of hardened steel. Before loading samples onto the anvil, the two culets of the diamond anvils were aligned to achieve optical parallelism; a symmetric ring at the center of the anvils is observed when these two anvils contact with each other. These two well-aligned anvils are then used to pre-indent a gasket. The gasket is made of hardened stainless steel SS301 and is used to confine the sample within the sealed chamber as well as to protect the anvils from

breakage. Typically, I pre-indent the gasket from an initial thickness of 250 μm to ≈100 μm and then drill a hole with ≈100 μm in diameter at the center of the pre-indented area by electric discharge machining. The drilled hole serves as the sample chamber as shown in Fig. 2.8.

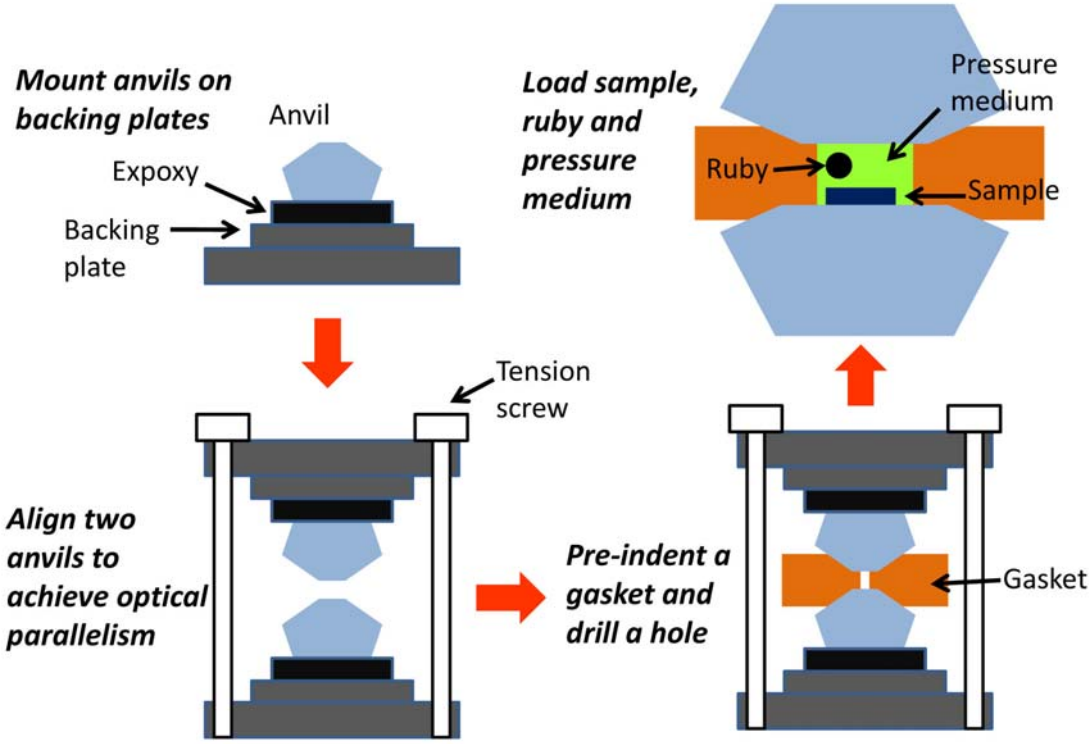

Fig. 2.9. Schematic illustration of the procedure for preparing a pressure cell.

After these preparations, a sample that has been coated with Al film and cut into a small piece (~50×50 μm^2) is manually loaded onto the gem anvil. For thin film samples, such as polymers, the sample is directly deposited on the anvil and then coated with Al. A small ruby crystal is also loaded into the sample chamber to calibrate the hydrostatic pressure by ruby fluorescence [25]. To transmit the hydrostatic pressure on the sample, typically Ar is loaded as the pressure medium into

the sample chamber using cryogenic loading. When performing thermal measurements at low pressure regime, $P < 1.3$ GPa, H_2O is used as the pressure medium since the liquid Ar may leak from the cell. (At room temperature and $P < 1.3$ GPa, Ar is a liquid; when $P > 1.3$ GPa, the equilibrium phase of Ar is a hcp crystal [26].) The pressure acting on the sample is increased (decreased) by tightening (loosening) the long tension screws on the cell.

2.3 Combination of TDTR and DAC

The main contribution of this thesis is to combine the ultrafast optical pump-probe method, TDTR, with DAC to explore the physics of thermal transport at higher pressures [15, 27-29].

This novel combination, in principle, can be applied to any material as long as the material is able to be (1) prepared or deposited with a flat surface, (2) coated with a metal film, and (3) loaded into the DAC. In addition, the measurement temperature can be varied from liquid nitrogen temperature to room temperature, or even a few thousand Kelvin. The physical stability of the metal film transducer determines the upper limit of the measurement temperature. For instance, typically Al is used as the thermal transducer; however, Al is not suitable for the high temperature measurements because of its low melting temperature, ≈930 K. Extension of the TDTR measurements to higher pressures and temperatures will be described in Chapter 6.

Furthermore, advances in the experimental technique also benefit the studies of thermal conductivity of minerals at Earth's lower mantle and core. For example,

the thermal conductivities of (Fe, Mg)O ferropericlase and (Fe,Mg)SiO_3 perovskite at extreme pressures and temperatures could be precisely measured using TDTR within DAC. Examples of studying the thermal conductivity of H_2O at high pressures [27] and measurements of the thermal conductivity of MgO up to 60 GPa at room temperature will be described in Chapter 3. These measurement results will be important steps to reconstruct the thermal history of icy planets and Earth's interior, respectively.

2.4 References

[1] D. G. Cahill, Rev. Sci. Instrum. **75**, 5119 (2004).

[2] K. Kang, Y. K. Koh, C. Chiritescu, X. Zheng, and D. G. Cahill, Rev. Sci. Instrum. **79**, 114901 (2008).

[3] C. A. Paddock, and G. L. Eesley, J. Appl. Phys. **60**, 285 (1986).

[4] D. A. Young, C. Thomsen, H. T. Grahn, H. J. Maris, and J. Tauc, in *Phonon Scattering in Condensed Matter*, edited by A. C. Anderson and J. P. Wolfe (Springer, Berlin, 1986).

[5] D. G. Cahill, K. Goodson, and A. Majumdar, J. Heat Transfer **124**, 223 (2002).

[6] C. Chiritescu, D. G. Cahill, N. Nguyen, D. Johnson, A. Bodapati, P. Keblinski, and P. Zschack, Science **315**, 351 (2007).

[7] R. M. Costescu, D. G. Cahill, F. H. Fabreguette, Z. A. Sechrist, and S. M. George, Science **303**, 989 (2004).

[8] Z. B. Ge, D. G. Cahill, and P. V. Braun, Phys. Rev. Lett. **96**, 186101 (2006).

[9] H. K. Lyeo, and D. G. Cahill, Phys. Rev. B **73**, 144301 (2006).

[10] Y. K. Koh, Ph. D. Thesis, p.13 (2010).

[11] A. S. Gray, and C. Uher, J. Mater. Sci. **12**, 959 (1977).

[12] C. Thomsen, H. T. Grahn, H. J. Maris, and J. Tauc, Phys. Rev. B **34**, 4129 (1986).

[13] D. G. Cahill, and F. Watanabe, Phys. Rev. B **70**, 235322 (2004).

[14] C. Thomsen, H. T. Grahn, H. J. Maris, and J. Tauc, Optics Comm. **60**, 55 (1986).

[15] W. P. Hsieh, B. Chen, J. Li, P. Keblinski, and D. G. Cahill, Phys. Rev. B **80**, 180302 (2009).

[16] S. Sinogeikin, J. Bass, V. Prakapenka, D. Lakshtanov, G. Y. Shen, C. Sanchez-Valle, and M. Rivers, Rev. Sci. Instrum. **77**, 103905 (2006).

[17] J. C. Crowhurst, A. F. Goncharov, and J. M. Zaug, J. Phys.-Conden. Matt. **16**, S1137 (2004).

[18] G. Tas, and H. J. Maris, Phys. Rev. B **49**, 15046 (1994).

[19] L. Vocadlo, J. Brodholt, D. Alfe, G. D. Price, and M. J. Gillan, Geophys. Res. Lett. **26**, 1231 (1999).

[20] H. K. Mao, and P. M. Bell, Science **200**, 1145 (1978).

[21] A. P. Jephcoat, R. J. Hemley, and H. K. Mao, Physica B & C **150**, 115 (1988).

[22] H. K. Mao, J. F. Shu, G. Y. Shen, R. J. Hemley, B. S. Li, and A. K. Singh, Nature **399**, 280 (1999).

[23] H. K. Mao, Y. Wu, R. J. Hemley, L. C. Chen, J. F. Shu, and L. W. Finger, Science **246**, 649 (1989).

[24] H. K. Mao, J. Xu, V. V. Struzhkin, J. Shu, R. J. Hemley, W. Sturhahn, M. Y. Hu, E. E. Alp, L. Vocadlo, D. Alfe, G. D. Price, M. J. Gillan, M. Schwoerer-Bohning, D. Hausermann, P. Eng, G. Shen, H. Giefers, R. Lubbers, and G. Wortmann, Science **292**, 914 (2001).

[25] H. K. Mao, P. M. Bell, J. W. Shaner, and D. J. Steinberg, J. Appl. Phys. **49**, 3276 (1978).

[26] J. Wittlinger, R. Fischer, S. Werner, J. Schneider, and H. Schulz, Acta Crystallographica Section B-Structural Science **53**, 745 (1997).

[27] B. Chen, W. P. Hsieh, D. G. Cahill, D. R. Trinkle, and J. Li, Phys. Rev. B **83**, 132301 (2011).

[28] W. P. Hsieh, M. D. Losego, P. V. Braun, S. Shenogin, P. Keblinski, and D. G. Cahill, Phys. Rev. B **83**, 174205 (2011).

[29] W. P. Hsieh, A. Lyons, E. Pop, P. Keblinski, and D. G. Cahill, (in preparation).

CHAPTER 3

PRESSURE TUNING OF THE THERMAL CONDUCTIVITY OF CRYSTALS

Parts of Section 3.1 were published in *Phys. Rev. B* **80**, 180302(R) (2009) by Wen-Pin Hsieh, Bin Chen, Jie Li, P. Keblinski, and David G. Cahill. Parts of Section 3.3 were published in *Phys. Rev. B* **83**, 132301 (2011) by Bin Chen, Wen-Pin Hsieh, David G. Cahill, Dallas R. Trinkle, and Jie Li.

3.1 Heat conduction in layered, anisotropic crystals

Recently, Chiritescu and Cahill *et al.* reported the observation of ultra-low thermal conductivity, thermal conductivity substantially lower than predicted by the minimum thermal conductivity model [1], in a disordered, layered crystal WSe_2 [2]. Low thermal conductivity in layered crystals has many applications, ranging from improvements in thermal barriers to materials for thermoelectric energy conversion [3-6].To understand the

origin of ultralow thermal conductivity in disordered, layered crystals, a subsequent molecular dynamics (MD) simulations was performed and showed that a high degree of anisotropy in elastic constants plays a critical role in suppressing the cross-plane thermal conductivity of a layered crystal [7]. As introduced in Chapter 1, pressure tuning of the elastic constant and thermal conductivity in the cross-plane direction enables a critical test of the validity of the MD results; in general, the softer cross-plane elastic constant C_{33} of a layered crystal has a higher anharmonicity and therefore increases more rapidly with pressure than the stiffer in-plane elastic constants.

To study the physics of thermal transport experimentally in layered crystals, a prototypical layered crystal, muscovite mica was chosen. Even though the layered structure of muscovite is not disordered, the cross-plane thermal conductivity Λ=0.46 W m^{-1} K^{-1} is extremely small for an oxide; it is a factor of ≈2 lower than the predicted minimum thermal conductivity in the cross-plane direction , 0.9 W m^{-1} K^{-1} [8, 9]. (The longitudinal and transverse speeds of sound in the cross-plane direction at ambient pressure, v_l=4.5 km s^{-1} and v_t=2.4 km s^{-1}, were calculated from the elastic constants C_{33}=58.6 GPa, C_{44}=16.5 GPa [10] , and mass density ρ=2.83 g cm^{-3}. The atomic density is n= 8.26×10^{22} cm^{-3}.) In addition, the thermal conductivity of muscovite at ambient pressure is also highly anisotropic: the in-plane thermal conductivity is ≈ 4 W m^{-1} K^{-1} [8].

To prepare the sample, a sheet of ≈20 μm-thick muscovite mica, $KAl_2(Si_3Al)O_{10}(OH)_2$ (grade V-1 from SPI Supplies) was first coated with ≈80 nm-thick Al film and cut into a small piece, ~50×50 μm^2, using a razor blade. This small Al-coated muscovite mica and a small ruby crystal were then loaded into a diamond anvil cell (DAC) with culet size of ≈500 μm and pressurized by high-pressure gas loading with Ar [11], see Fig. 3.1 for the schematic diagram of the Al/muscovite sample in DAC. (The schematic unit cell of muscovite is shown in Ref. [10].)

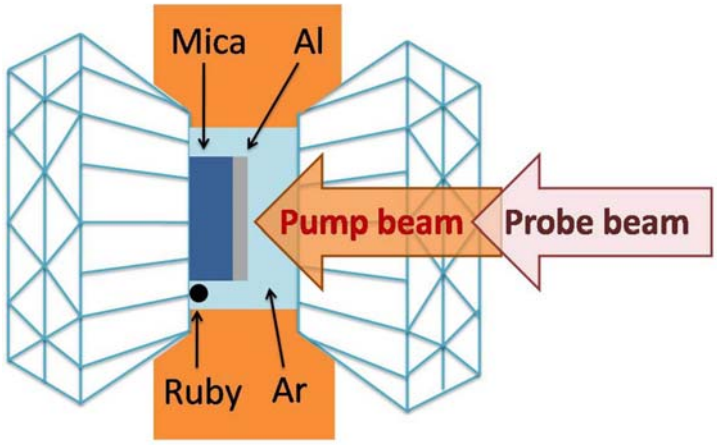

Fig. 3.1. Schematic drawing of the optical pump-probe measurements, i.e., TDTR and Brillouin scattering, of a muscovite mica within a diamond anvil cell. An Al thin film serves as a transducer to absorb energy from the pump beam and enables measurements of temperature evolution by measuring changes in the intensity of the reflected probe beam. The pressure medium is Ar.

I measured the cross-plane thermal conductivity Λ of muscovite at room temperature using time-domain thermoreflectance (TDTR) [12-14], see Chapter 2 for the details. In the TDTR system, after the optical pump pulse heats the Al film coated on the muscovite mica I measured the changes in the reflectivity of Al as a function of time which reveals its surface temperature evolution. The time dependence of the temperature variation on the Al surface provides important information about the thermal transport properties of the muscovite sample. However, I found the thermoreflectance of Al at 785 nm crosses through zero at $P \approx 6$ GPa [15], which substantially degrades the accuracy of my thermal measurements near this pressure.

To maintain a high signal-to-noise ratio at pressures near $P=6$ GPa, I modified the TDTR setup outlined in Chapter 2 in four ways. First, I shifted the fundamental wavelength of the laser to 765 nm. Second, I replaced the 790 nm long-pass filter in the pump beam path with a 770 nm long-pass filter. Third, I replaced the 785 nm band-pass filter in the path of the probe beam with a 770 nm short-pass filter rotated by ≈18° to blue-shift the peak wavelength to ≈761 nm. Fourth, I replaced the short-pass filter in front of the Si photodiode detector with a 760 nm short-pass filter. These changes allowed me conduct my experiments with a probe beam at a wavelength of 765 nm, where thermoreflectance of Al does not approach zero until ≈8 GPa.

In order to determine the cross-plane thermal conductivity of muscovite, I compare the ratio V_{in}/V_{out} as a function of delay time with calculations from a thermal model [16] that was modified to take into account heat flow into the muscovite as well as into the Ar pressure medium [17]. Since the thermal penetration depth at the modulation frequency of the pump beam, 10 MHz, is ≈50-200 nm, much smaller than the radius of the laser spot size, ≈7.5 μm, heat flow is predominately one-dimensional in the cross-plane direction. Fig. 3.2 (a) shows the example data and fits to the thermal model.

As described in section 2.1.2, there are many parameters in the thermal model—laser spot size (≈7.5 μm), Al film thickness h_{Al}, thermal conductivity and heat capacity of each layer—but the thermal conductivity of muscovite mica is the only significant unknown model parameter. I measured the h_{Al} at ambient conditions by picosecond acoustics [18]. The pressure dependent thermal conductivity of Ar at room temperature was taken from recently published molecular dynamics simulations [19], see Fig. 3.3. Since the thermal conductivities of muscovite and Ar are relatively small, the thermal model calculation is insensitive to the thermal conductance G of interfaces between Al and these materials. Therefore, I set G= 200 MW m^{-2} K^{-1} for the Al/muscovite interface and G= 80 MW m^{-2} K^{-1} for the Al/Ar interface at low pressures, and find that G= 200 MW m^{-2} K^{-1} for the Al/Ar interface provides the best fit to my data at high

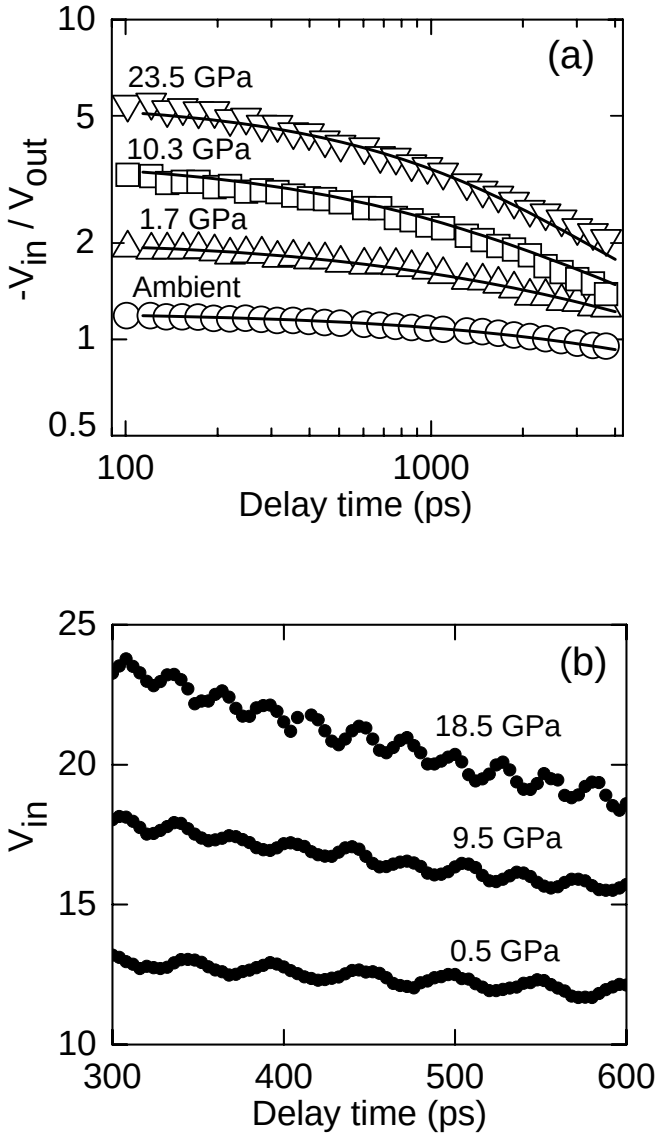

Fig. 3.2. (a) Example data for the ratio V_{in}/V_{out} as a function of delay time and fits (solid lines) to the thermal model of Ref. [16]; data and fits are labeled by the pressure. **(b)** Example data for the periodic oscillations in V_{in} that are used to measure the Brillouin frequency of muscovite mica.

pressures. At intermediate pressures, I linearly scale the pressure dependence of thermal conductance of Al/Ar interface by $G = G_0 + G_1 P$ MW m^{-2} K^{-1}, where G_0=70 MW m^{-2} K^{-1} and G_1=5.2 MW m^{-2} K^{-1} GPa^{-1}, and P is the pressure in GPa.

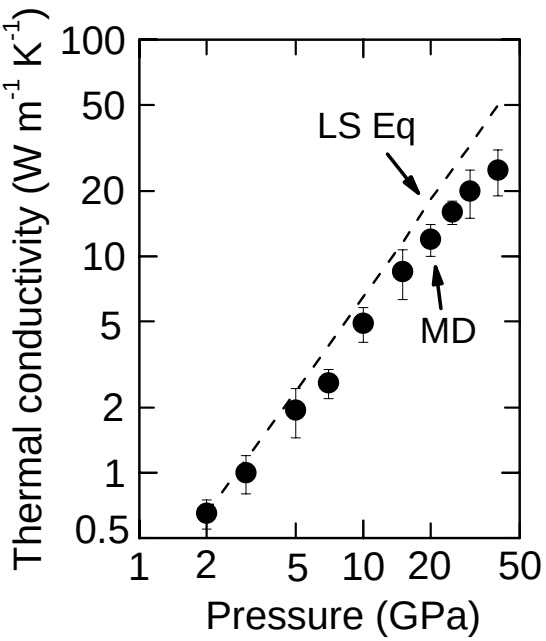

Fig. 3.3. Pressure dependence of the thermal conductivity of Ar at room temperature calculated by molecular dynamics (MD) simulations using Green-Kubo formalism (solid symbols) [19]. The thermal conductivity of Ar predicted by the Leibfried-Schlömann (LS) equation (dashed line), see Eq. (3.2), is plotted for comparison. The Grüneisen constant as a function of pressure in the LS equation is taken from Ref. [19].

Since the heat capacities of Al, muscovite mica, and Ar at high pressures are not known, I estimate the pressure dependence of the heat capacities from data for the temperature dependence of the heat capacity combined with data for the pressure dependence of the atomic density and elastic constants. For example, because of the

relatively low Debye temperature of Ar, the heat capacity should be in good agreement with the value at the classical limit [19]. (The Debye temperature Θ_D is 132 K and 370 K at *P*=2 and 20 GPa, respectively.) Thus, I fix the heat capacity per atom as the classical value, i.e., $3k_B$ per atom, where k_B is the Boltzmann constant; *C*= 1.36, 1.86, and 2.16 J cm^{-3} K^{-1} at *P*=2, 10, and 20 GPa, respectively [20].

For Al, I assume that changes in the specific heat at high pressures can be estimated from the specific heat at ambient pressure but at reduced temperature [21]. For example, at 10 and 20 GPa, the Debye temperature Θ_D of Al increases by 24 % and 43 % [22], respectively, and therefore I use the measured specific heats of Al at *T*=300/1.24=242 K and *T*=300/1.43=210 K to calculate the heat capacities at 10 GPa and 20 GPa. Figure 3.4 shows the estimated specific heat of Al (solid symbols) as a function of reduced temperature T/Θ_D, where T is the measurement temperature, 300 K.

In my first paper [23], an error was made due to the double counting of this volumetric heat capacity of Al film under pressure. To correct this error, I take into account changes in the Al thickness h_{Al} under pressure. The changes in h_{Al} as a function of pressure is obtained by calculating changes in the volume of Al using the equation of state, $B_T = 73 + 4.54P$ [24] and by assuming that the Al film adheres well to the muscovite mica substrate and that the Al film plastically deforms to accommodate the mismatch in

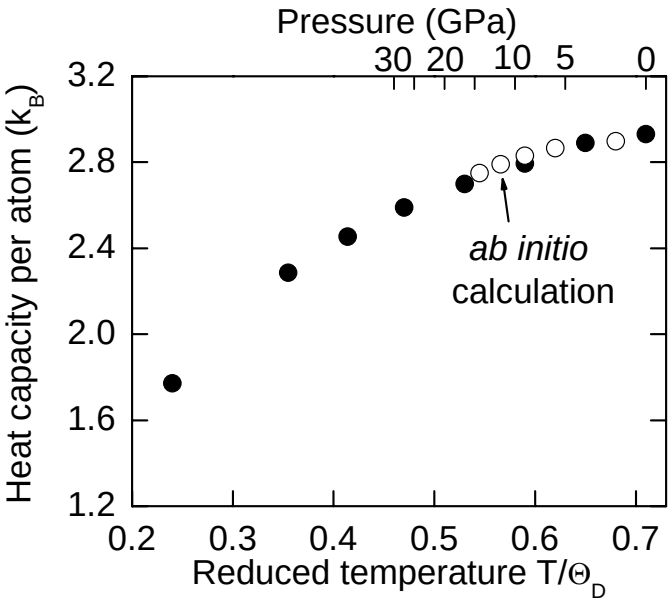

Fig. 3.4. Estimated heat capacity per atom of Al as a function of reduced temperature T/Θ_D, where T=300 K and Θ_D is the Debye temperature of Al. Heat capacity per atom obtained by *ab initio* calculation [25] (open circles) is plotted for comparison.

lateral compression of the Al film and the muscovite substrate. The changes in the lattice constants of muscovite under pressure are taken from the data in Ref. [26]. For example, at 10 GPa, the volume of Al decreases by 10 % and the lattice constants of muscovite decrease by 2.2 % and 2.3 % along *a* and *b* direction, respectively, where *a* and *b* are two principal axes in the basal plane of muscovite. Therefore, the decrease in the Al thickness h_{Al} is 5.5 %. The h_{Al} decreases by 3.1 % at 5 GPa, 5.5 % at 10 GPa, and 7.5 % at 20 GPa. Figure 3.5 summarizes the heat capacity per atom, volumetric heat capacity, thickness, and heat capacity per unit area of Al as a function of pressure.

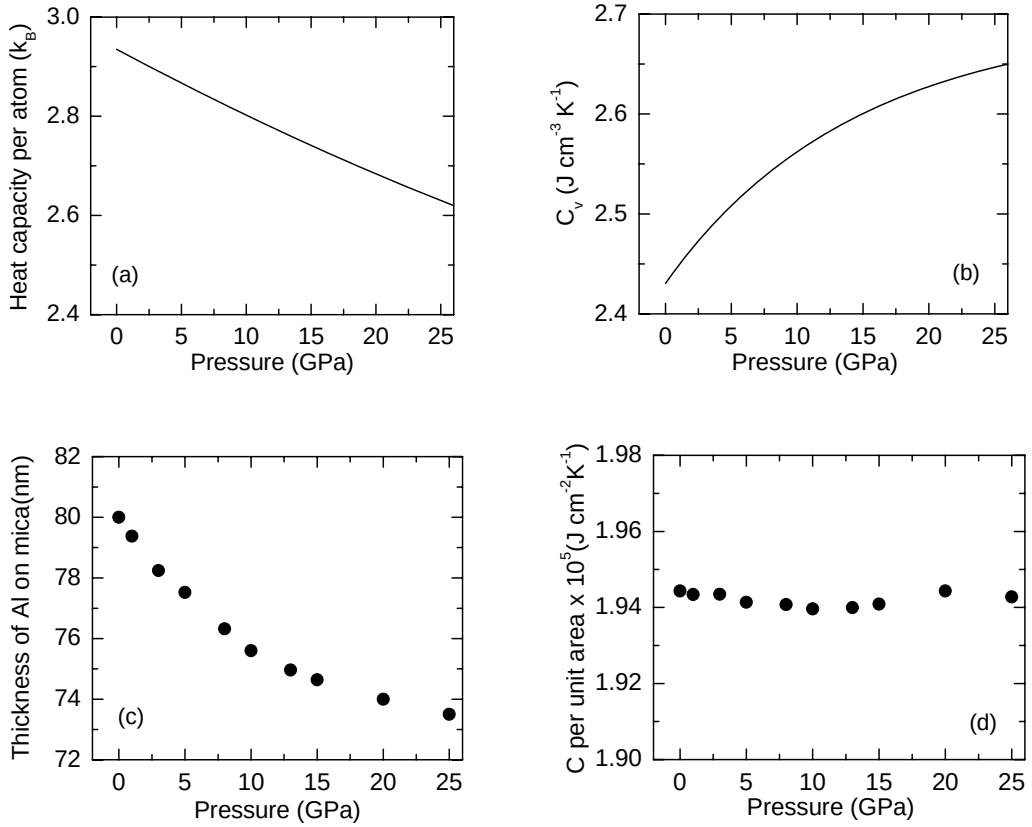

Fig. 3.5. Estimated **(a)** heat capacity per atom and **(b)** volumetric heat capacity of Al as a function of pressure. **(c)** Pressure dependence of the thickness of an Al film (80 nm thick at ambient) on muscovite. **(d)** Heat capacity per unit area, product of volumetric heat capacity in (b) and thickness in (c), of Al on mica as a function of pressure.

For muscovite, I use data for the pressure dependence of elastic constants of $MgSiO_3$ [27] to estimate the changes in the Debye temperature of muscovite mica at high pressures. This is justified because $MgSiO_3$ has nearly the same average atomic weight as muscovite and the temperature dependence of the specific heats are nearly identical to that of mica over a wide temperature range [21]. The pressure dependence of the heat

capacity of muscovite mica was estimated by the calculation of changes in the Debye temperature combined with the data for temperature dependence of specific heat at ambient pressure. The volumetric heat capacity of muscovite at ambient conditions is $C_{muscovite}$= 2.3 J cm^{-3} K^{-1} and increases by 9% at 10 GPa and 15% at 20 GPa. The density of muscovite increases by 11.5% at 10 GPa and 20% at 20 GPa [28].

The elastic constants of mica were measured by time-domain stimulated Brillouin scattering, see section 2.1.4 for the details. The frequency of the periodic oscillations in the in-phase signal V_{in}, as shown in Fig 3.2 (b), is just the Brillouin frequency f_B. For longitudinal modes in a backscattering geometry, $f_B = 2Nv_l / \lambda$, where N is the index of refraction, v_l the longitudinal speed of sound, and λ the laser wavelength.

The pressure dependence of f_B of the muscovite mica is shown in Fig. 3.6(a). In order to obtain the corresponding cross-plane elastic constant C_{33}, see Fig. 3.6(b), I calculated the pressure dependence of the density ρ using the equation of state of muscovite [28] and calculated the index of refraction N using the Lorentz-Lorenz formula $\left(N^2-1\right)/\left(\rho\left(N^2+2\right)\right)=A$, where A is assumed to be a constant [29]. At ambient conditions, N= 1.56, ρ= 2.83 g cm^{-3}, and A= 0.114; N increases by 4.8% at 10 GPa and 9% at 20 GPa.

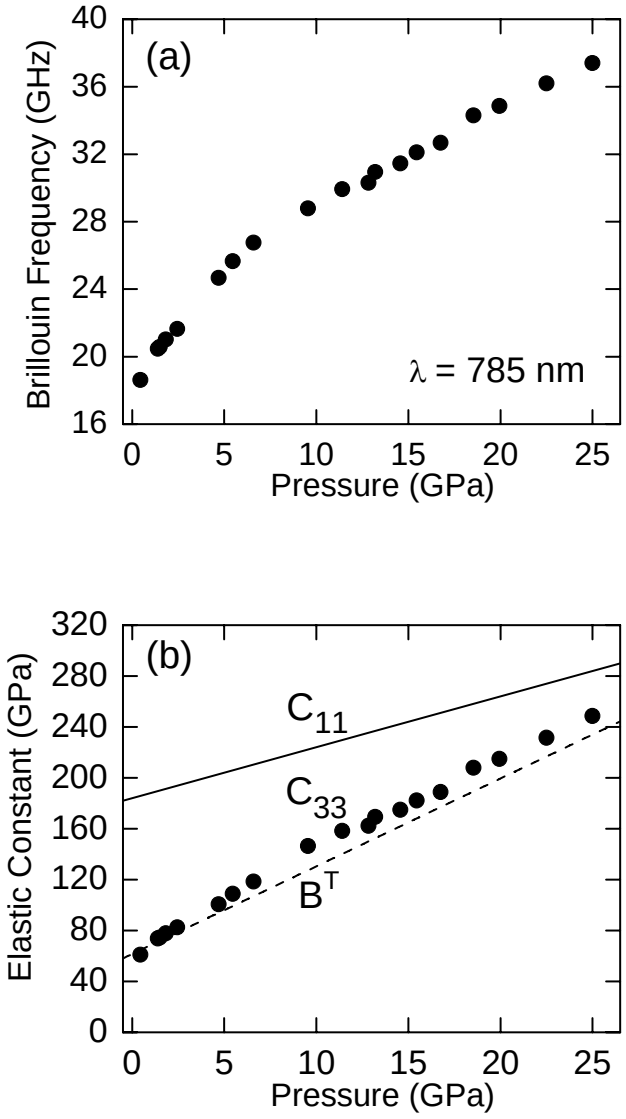

Fig. 3.6. Pressure dependence of the **(a)** Brillouin frequency and **(b)** C_{33} of the muscovite mica. C_{33} is obtained from the Brillouin frequency measurements combined with the equation of state of muscovite and an assumption that the index of refraction follows the Lorentz-Lorenz formula. The estimated C_{11} = 184 GPa +4P and previously measured bulk modulus B_T = 61.4 GPa + 6.9P [28] are plotted as solid and dashed line, respectively, for comparison.

The pressure dependence of the in-plane elastic constant C_{11} and the transverse speed of sound can not be measured using the current apparatus. However, if I assume that $dC_{11}/dP \approx 4$, a typical value for many silicates [30, 31], then C_{11}= 184 GPa +4P and C_{33} approaches C_{11} as the measurement pressure increases to P≈24 GPa, see Fig. 3.6(b). As the layered muscovite is compressed along the cross-plane direction, the force constants of the interaction between the silicate layers increases [29].

Pressure dependence of the cross-plane thermal conductivity Λ of muscovite mica is shown in Fig. 3.7. Λ increases with pressure [32] by a factor of ≈3 and ≈11 at a pressure of 5 GPa and 24 GPa, respectively. Note that this data set includes measurements for both increasing and decreasing pressure. To check if there is hysteresis in the measured thermal conductivity, I also measured the thermal conductivity at ambient pressure after I unloaded the cell and obtained the same value, 0.46 W m^{-1} K^{-1}, as I measured before the muscovite mica was compressed. As a result, the changes in the thermal conductivity of muscovite mica are reversible and I have not observed significant hysteresis in the thermal conductivity. Furthermore, my measurements do not support a previous study which reports that a crystal-to-amorphous transition in muscovite is observed at P≥20 GPa [28].

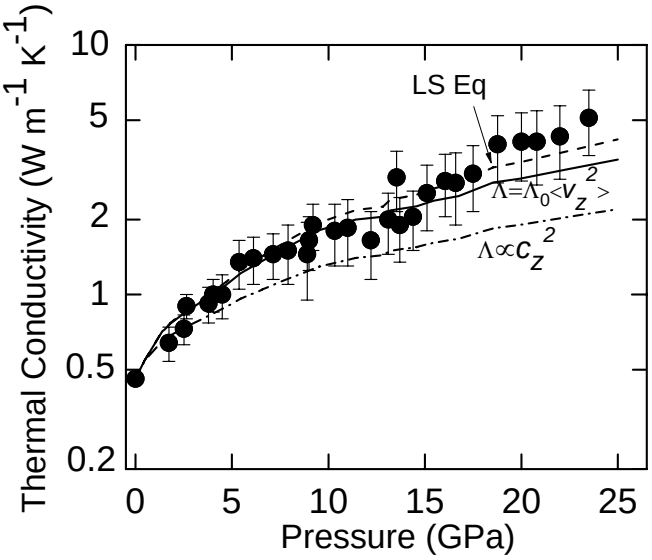

Fig. 3.7. Measurements (solid symbol) and theoretical predictions of the cross-plane thermal conductivity Λ of muscovite as a function of pressure. Error bars on the data points are dominated by uncertainties in the parameters in the thermal model used to analyze the data. The predicted Λ based on a constant relaxation time and an anisotropic Debye model (Eq. 3.1) is shown as a solid line; and the dashed-dot line shows the scaling $\Lambda \propto c_z^2$. The difference between the scaling predicted by Eq. 3.1 and the scaling $\Lambda \propto c_z^2$ is the contribution to the pressure dependence of Λ due to changes in elastic anisotropy. The prediction of the LS equation using the scaling $\omega_D \propto \sqrt{C_{33}}$ is shown as a dashed line.

As mentioned before, in my first paper [23], an error was made due to the double counting of the volumetric heat capacity of Al film under pressure. When the pressure dependence of the Al thickness is corrected, the thermal conductivity of the muscovite mica decreases by 23% at the highest pressure, *P*=23.5 GPa, in the data shown in Ref. [23]. This error is comparable to the experimental uncertainties and the correction does

not change any conclusion in Ref. [23]. The data shown in Fig. 3.7 have been corrected.

To gain insight into the physics of thermal transport in layered crystals, I compare my thermal conductivity data with two simple models. First, I consider the thermal conductivity in a relaxation time approximation, $\Lambda = C \left\langle v_z^2 \right\rangle \tau$, where C is the volumetric heat capacity of the vibrational modes that contribute significantly to thermal transport, τ is the relaxation time, and $\left\langle v_z^2 \right\rangle$ is the average of the square of the group velocities of the vibrational modes in cross-plane direction. If both the volumetric heat capacity C and relaxation time τ can be assumed to be weakly dependent on the pressure, then the changes in $\left\langle v_z^2 \right\rangle$ dominates the changes in Λ.

In an anisotropic Debye model, the phonon dispersion is given by $\omega^2 = (k_x c_x)^2 + (k_y c_y)^2 + (k_z c_z)^2$, where k_i and c_i are the wave vector and speed of sound along the i direction. The group velocity in the cross-plane direction is $v_z = \partial\omega/\partial k_z$. For muscovite mica, $C_{11} \approx C_{22}$; therefore, I assume $c_x = c_y$ which gives:

$$\left\langle v_z^2 \right\rangle = c_z^2 \int_0^{\pi/2} \frac{c_z^2 \cos^2\theta}{c_x^2 \sin^2\theta + c_z^2 \cos^2\theta} \sin\theta d\theta . \qquad (3.1)$$

To evaluate Eq. (3.1), since $c_x^2 = C_{11}/\rho$ and $c_z^2 = C_{33}/\rho$, I assume the pressure dependence of c_x^2 and c_z^2 follows the pressure dependence of C_{11} and C_{33}. The solid line in Fig. 3.7 shows the predicted Λ based on the relaxation time approximation and using $\left\langle v_z^2 \right\rangle$ from Eq. (3.1) and a fit to Λ at ambient pressure; i.e., $\Lambda = \Lambda_0 \left\langle v_z^2 \right\rangle$ with

Λ_0=4.2×10^{-8} J s m^{-3} K^{-1}. Even though the effects of changes in the relaxation time with pressure cannot be excluded, the good agreement between my data and the prediction based on Eq. (3.1) suggests that most of the pressure dependence of Λ can be accounted for by changes in the sound velocities in the cross-plane direction.

Note that such good agreement between the data and this simple model also suggests that the thermal energy transport along the cross-plane direction in muscovite mica is predominantly carried by acoustic phonons. Even though the acoustic phonons are known to be the dominant heat carriers in dielectric materials, this conclusion is not obviously true for thermal transport along the cross-plane direction of muscovite because the cross-plane thermal conductivity is much smaller than the predicted minimum value and only a minority of the vibrational modes are acoustic modes with large group velocities.

On the other hand, the Leibfried-Schlömann (LS) equation can also describe my data:

$$\Lambda = A_0 \frac{V^{\frac{1}{3}} \omega_D^{\ 3}}{\gamma^2 T}, \qquad (3.2)$$

where V is the volume, ω_D the Debye frequency, γ the Grüneisen constant, T the temperature, and A_0 is a constant that is independent of pressure [33, 34]. If I assume that

the Debye frequency ω_D scales with C_{33}, i.e., $\omega_D \propto \sqrt{C_{33}}$, then the prediction of Eq. (3.2) is proportional to $C_{33}^{3/2}$ and also agrees well with the data, see Fig. 3.7. I assume the Grüneisen constant for longitudinal modes in the cross-plane direction, $\gamma = (1/2)dC_{33}/dP \approx 3.8$, is approximately a constant. However, since the original derivation of LS equation assumes an isotropic crystal, the scaling $\omega_D \propto \sqrt{C_{33}}$ is difficult to justify.

3.2 Thermal conductivity of MgO up to 60 GPa at room temperature

Understanding the thermal evolution and geodynamics of the Earth's core and mantle is one of the most important topics in geophysics. Thermal conductivity of minerals in Earth's interior plays a critical role in interpreting many geophysical phenomena, such as the temperature evolution of mantle and core [35, 36]. Knowledge of the pressure dependence of thermal conductivity of minerals in Earth's mantle would advance the progress in mantle convection models [37-39]. However, current estimates of the thermal and electrical conductivity of minerals in the mantle and core rely mostly on theoretical calculations [40-43] and extrapolations [44] with large uncertainties. Therefore, precise measurements of thermal conductivities of main constituents in Earth's lower mantle, e.g., (Mg, Fe)O ferropericlase and (Mg, Fe)SiO_3 perovskite, are essential.

In collaboration with Dr. Alex Goncharov at the Geophysical Laboratory of Carnegie Institution of Washington, we have studied the thermal conductivity of single crystalline MgO at room temperature up to 60 GPa.

A piece of single crystalline MgO (from SPI supplies), 5×5 mm^2 and 0.5 mm in thickness, was first placed on a graphite sheet heater and electrically heated to ≈1200 K for 30 minutes under a pressure of ≈4×10^{-7} torr to remove the volatile contaminants on the MgO surface. After the MgO cools down to near room temperature, it was coated with ≈80 nm-thick Al film by magnetron sputtering. Subsequent sample preparation was completed by Dr. Allen Dalton in Dr. Alex Goncharov's group. The back side of the MgO was manually polished down to ≈20 μm in thickness and cut into a smaller piece, ≈30×30 μm^2 with a razor blade. The Al-coated MgO and a ruby chip were then loaded into a diamond anvil cell with culet size of ≈300 μm using high-pressure gas loading. Ar was used as the pressure medium. The pressure was determined by ruby fluorescence [45].

The sample preparation plays a critical role in obtaining correct data. When the MgO was polished first, and then coated with Al on the polished side, a thin layer of hydroxide on the surface of MgO is formed which substantially reduces the interface thermal conductance between MgO and Al. This high interface thermal resistance results

in my measurements being less sensitive to the thermal conductivity, increasing the uncertainty in my measurements. Heating the polished MgO to ≈1200 K before Al deposition may not completely remove the hydroxide layer. I was unable to obtain a reliable measurement of the thermal conductivity of MgO, near the expected value of Λ=53 W m^{-1} K^{-1}, at ambient conditions on samples that were polished prior to Al deposition.

I used time-domain thermoreflectance to measure the thermal conductivity of MgO at high pressures. The experimental setup is the same as that in the studies of muscovite mica. The heat capacity C_{Al} of Al, thermal conductivity Λ_{Ar} and heat capacity C_{Ar} of Ar as a function of pressure are all obtained by the same approaches as described in section 3.1. However, the heat capacity of Ar at pressures higher than 30 GPa starts to deviate from the classical limit since the T/Θ_D is smaller than 0.7 [46]. The Debye temperature Θ_D of Ar is 440 K, 530 K, and 600 K at P=30, 45, and 60 GPa, respectively. I correct the deviation of heat capacity from the classical limit by assuming a Debye-like density of states for Ar [46].

For the pressure dependence of the thickness h_{Al} of Al, see Fig. 3.8 (c), I calculate changes in the volume of Al using the equation of state, $B_T = 73 + 4.54P$ [24], and assume that the Al film adheres well to the MgO substrate and that the Al plastically deforms to

accommodate the mismatch in lateral compression of the Al film and MgO. The changes in the lattice constants of MgO under pressure are calculated by the equation of state from Ref. [47]. Figure 3.8 presents the heat capacity per atom, volumetric heat capacity, thickness, and heat capacity per unit area of Al as a function of pressure.

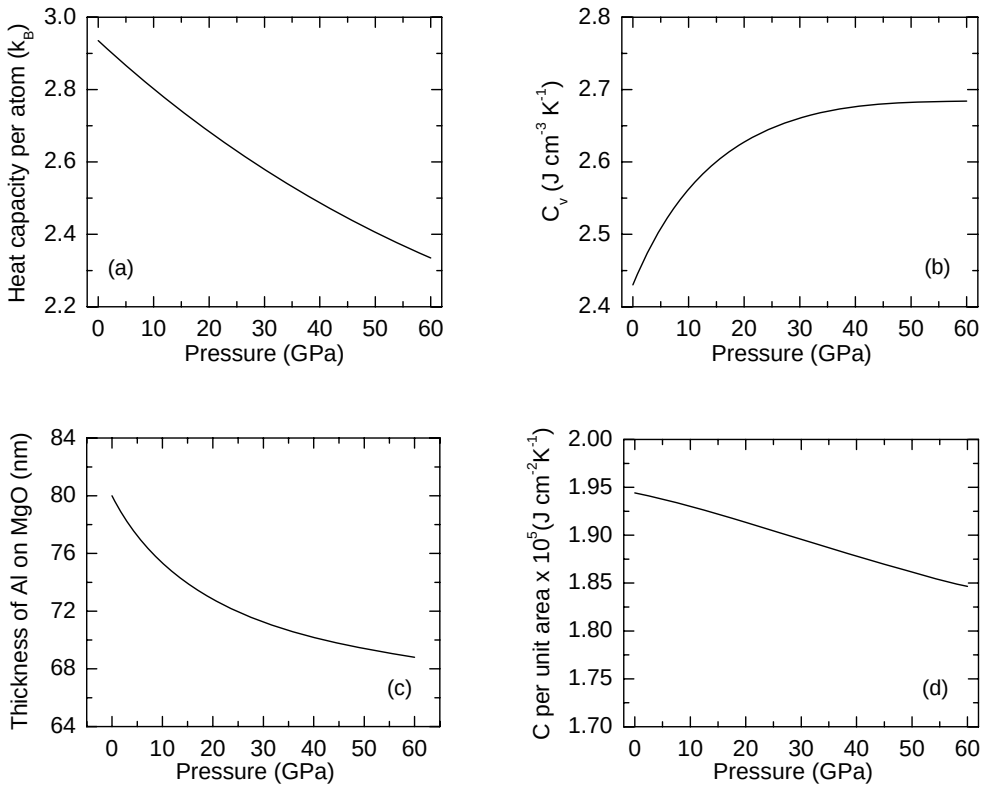

Fig. 3.8. Pressure dependence of **(a)** heat capacity per atom and **(b)** volumetric heat capacity of Al. **(c)** Thickness of an Al film (80 nm thick at ambient) on MgO as a function of pressure. **(d)** Pressure dependence of the heat capacity per unit area, product of volumetric heat capacity in (b) and thickness in (c), of Al.

Literature data for the heat capacity per atom C_a of MgO at high pressures are shown in Fig. 3.9(a) [48-51]. To estimate the pressure dependence of heat capacity per

atom $C_a(P)$ over the pressure range I studied, I fitted these data to a second order polynomial in P and obtained $C_a(P) = C_0 + C_1 P + C_2 P^2$, where C_0=2.23 k_B, C_1=-1.38×10^{-2} k_B GPa^{-1}, C_2=1.16×10^{-4} k_B GPa^{-2}, and P in GPa, see the dashed curve in Fig. 3.9(a). The calculated volumetric heat capacity of MgO at high pressures is plotted in Fig. 3.9(b).

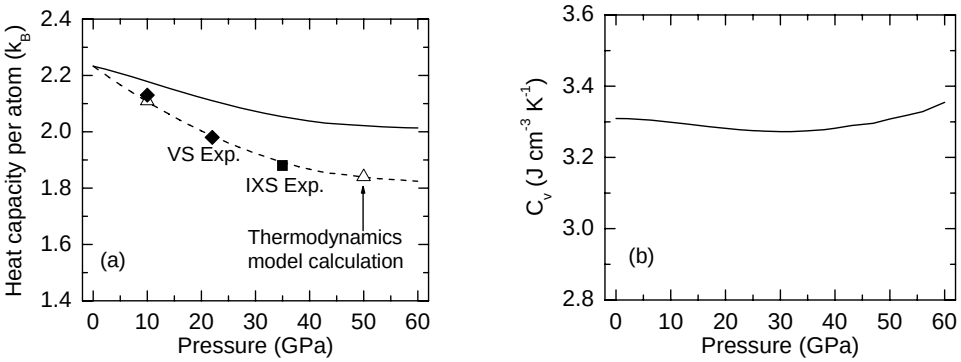

Fig. 3.9. (a) Heat capacity per atom and **(b)** volumetric heat capacity of MgO as a function of pressure. In (a), the solid line shows the heat capacity per atom estimated by specific heat at ambient pressure and reduced temperature combined with the changes in the Debye temperature under pressure, see section 3.1 for the details. VS Exp denotes the heat capacity was obtained by measuring the vibrational spectrum of Cr-doped MgO [48, 49]; IXS Exp denotes the heat capacity was obtained by inelastic x-ray scattering combined with *ab intio* calculations [50].

Figure 3.10 presents the thermal conductivity Λ of MgO at room temperature up to 60 GPa. Λ increases from 53 W m^{-1} K^{-1} at ambient conditions to 161 W m^{-1} K^{-1} at P=59 GPa. This data set includes measurements for both increasing (solid circles) and decreasing (open circles) pressure; the changes in the Λ of MgO are reversible.

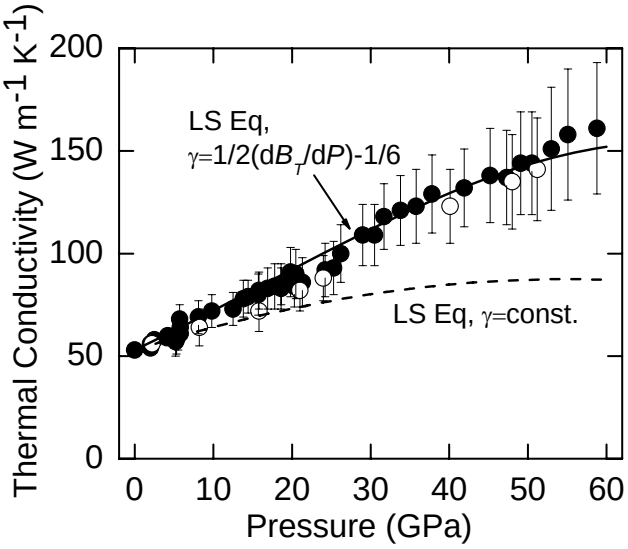

Fig. 3.10. Thermal conductivity of MgO up to 60 GPa at room temperature. The solid (open) circles show compression (decompression) data. The solid curve shows the predicted thermal conductivity based on the LS equation with $\gamma = \frac{1}{2}\frac{dB_T}{dP} - \frac{1}{6}$, which is calculated by the pressure derivative of the isothermal bulk modulus from the EOS of MgO in Ref. [47]. The thermal conductivity predicted by the LS equation with a constant γ is plotted as the dashed curve for comparison.

In Fig. 3.10, I also compare my measurements with the prediction of Λ of MgO based on the Leibfried-Schlömann (LS) equation (Eq. 3.2). As mentioned in the end of section 3.1, the LS equation is widely employed to describe or predict the pressure dependence of thermal conductivity of non-metallic, isotropic crystals where heat is predominantly carried by phonons. The LS equation [33, 34] assumes that most of the thermal energy is conducted by acoustic phonons and the contribution of optical phonons can be neglected. In addition, the LS equation also assumes that the phonon

mean-free-path is dominated by the three-phonon anharmonic scattering between acoustic phonons.

In the LS equation (Eq. 3.2), the pressure dependence of the lattice constant of MgO is calculated using the equation of state (EOS) from Ref. [47]. The Debye temperature, proportional to the Debye frequency ω_D, at high pressures is calculated using the pressure dependence of elastic constants and EOS from Ref. [47] combined with a method described in Ref. [22]. To calculate the Grüneisen parameter γ, the Slater γ [52], I assume that the Poisson ratio and elastic anisotropy are both constant under pressure and therefore the Grüneisen parameter γ can be derived from the pressure derivative of the isothermal bulk modulus: $\gamma = \frac{1}{2}\frac{dB_T}{dP} - \frac{1}{6}$, where B_T is the isothermal bulk modulus of MgO. Taking the pressure derivative of B_T of MgO from the EOS [47], the Grüneisen parameter at ambient pressure is γ=1.82 and decreases by 15 % at 30 GPa and 23% at 60 GPa.

The predicted Λ of MgO based on the LS equation $\Lambda = A\frac{V^{\frac{1}{3}}\omega_D{}^3}{\gamma^2}$, where the constant A=1.71×10^{-28} J s^2 m^{-2} K^{-1}, V is the volume, ω_D is the Debye frequency, and γ is the Grüneisen parameter, is shown as the solid curve in Fig. 3.10. Since the original derivation of the LS equation assumes that the thermal energy is dominantly transported

by acoustic phonons, the good agreement between my measurements and the prediction by the LS equation suggests that optical phonons in MgO play a minor role in the thermal transport. However, since γ varies widely [47, 53-56] due to the uncertainties in the pressure dependence of elastic constants used to derive the Grüneisen parameter, an accurate prediction of Λ by the LS equation requires accurate measurements of the EOS of MgO.

Since minerals at Earth's lower mantle are under extreme pressure and temperature, data for the thermal conductivity of MgO at elevated temperature are essential. I am currently collaborating with Dr. Alex Goncharov's group to perform measurements of the Λ of MgO at high temperature, ≈900 K, using resistive heating.

3.3 Testing the LS equation on materials with multi-atoms per unit cell

Through the collaboration with Dr. Bin Chen and Prof. Jie Li at the University of Michigan, we also tested the validity of the Leibfried-Schlömann equation on a material with multi-atoms per unit cell by measuring the thermal conductivity of H_2O (water, ice VI, and ice VII phases) at room temperature up to 22 GPa using TDTR and DAC [57], see Fig. 3.11.We found that the LS equation describes our measurements of the thermal

conductivity of H_2O to within 20 %. This suggests that the LS equation could be used to predict the thermal conductivity of a non-metallic pure material at high pressures if the thermal conductivity at ambient pressure and the EOS of the material are known.

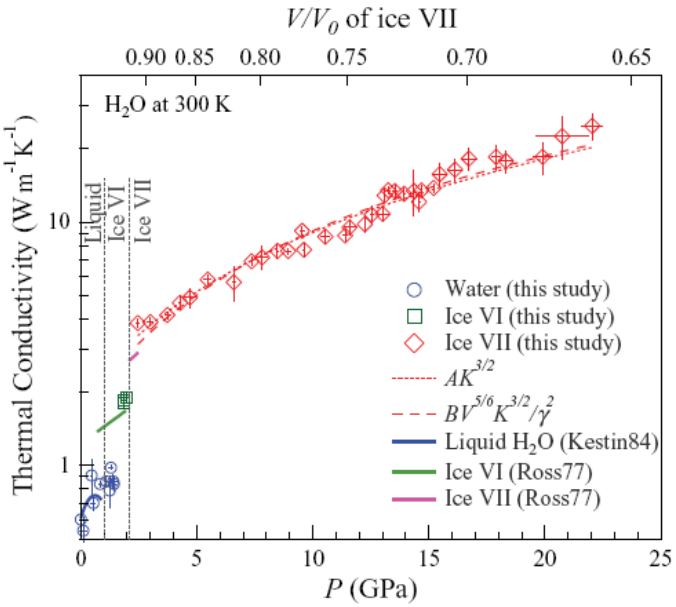

Fig. 3.11. Pressure dependence of the thermal conductivity of H_2O (water, ice VI, and ice VII) at room temperature [57].

3.4 Conclusion

In this chapter, I have shown that the combination of TDTR and DAC is a powerful tool to study the pressure dependence of thermal transport properties of crystals. I anticipate that measurements of the thermal conductivity of MgO at high temperature will provide significant information to examine the validity of current theoretical models for geodynamics in the Earth interior.

3.5 References

[1] D. G. Cahill, S. Watson, and R. Pohl, Phys. Rev. B **46**, 6131 (1992).

[2] C. Chiritescu, D. G. Cahill, N. Nguyen, D. Johnson, A. Bodapati, P. Keblinski, and P. Zschack, Science **315**, 351 (2007).

[3] T. Kanno, S. Yotsuhashi, and H. Adachi, Appl. Phys. Lett. **85**, 739 (2004).

[4] Y. Shen, D. R. Clarke, and P. A. Fuierer, Appl. Phys. Lett. **93**, 102907 (2008).

[5] K. Takahata, Y. Iguchi, D. Tanaka, T. Itoh, and I. Terasaki, Phys. Rev. B **61**, 12551 (2000).

[6] I. Terasaki, H. Tanaka, A. Satake, S. Okada, and T. Fujii, Phys. Rev. B **70**, 214106 (2004).

[7] L. Hu, P. Keblinski, S. Shenogin, and D. G. Cahill, unpublished.

[8] A. S. Gray, and C. Uher, J. Materials Science **12**, 959 (1977).

[9] R. W. Powell, and E. Griffiths, Proc. Roy. Soc. London A **163**, 189 (1937).

[10] M. T. Vaughan, and S. Guggenheim, J Geophys Res-Solid **91**, 4657 (1986).

[11] M. Rivers, V. B. Prakapenka, A. Kubo, C. Pullins, C. M. Holl, and S. D. Jacobsen, High Pressure Research **28**, 273 (2008).

[12] C. A. Paddock, and G. L. Eesley, J. Appl. Phys. **60**, 285 (1986).

[13] D. A. Young, C. Thomsen, H. T. Grahn, H. J. Maris, and J. Tauc, in *Phonon*

Scattering in Condensed Matter, edited by A. C. Anderson and J. P. Wolfe (Springer, Berlin, 1986).

[14] D. G. Cahill, W. K. Ford, K. E. Goodson, G. D. Mahan, A. Majumdar, H. J. Maris, R. Merlin, and S. R. Phillpot, J. Appl. Phys. **93**, 793 (2003).

[15] R. G. Dandrea, and N. W. Ashcroft, Phys. Rev. B **32**, 6936 (1985).

[16] D. G. Cahill, Rev. Sci. Instrum. **75**, 5119 (2004).

[17] Z. B. Ge, D. G. Cahill, and P. V. Braun, Phys. Rev. Lett. **96**, 186101 (2006).

[18] C. Thomsen, H. T. Grahn, H. J. Maris, and J. Tauc, Phys. Rev. B **34**, 4129 (1986).

[19] K. V. Tretiakov, and S. Scandolo, J. Chem. Phys. **121**, 11177 (2004).

[20] H. Shimizu, H. Tashiro, T. Kume, and S. Sasaki, Phys. Rev. Lett. **86**, 4568 (2001).

[21] *Thermophysical properties of high temperature solid materials,* Purdue University, edited by Y. S. Touloukian (1967) **4**.

[22] W. P. Binnie, Phys. Rev. **103**, 579 (1956).

[23] W. P. Hsieh, B. Chen, J. Li, P. Keblinski, and D. G. Cahill, Phys. Rev. B **80**, 180302 (2009).

[24] C. Bercegeay, and S. Bernard, Phys. Rev. B **72**, 214101 (2005).

[25] G. J. Vazquez, and L. F. Magana, Phys. Lett. A **122**, 267 (1987).

[26] N. Curetti, D. Levy, A. Pavese, and G. Ivaldi, Phys. Chem. Minerals **32**, 670 (2006).

[27] R. M. Wentzcovitch, B. B. Karki, S. Karato, and C. R. S. Da Silva, Earth and Planetary Sci. Lett. **164**, 371 (1998).

[28] J. Faust, and E. Knittle, J. Geophys. Res.-Solid Earth **99**, 19785 (1994).

[29] L. E. McNeil, and M. Grimsditch, J. Phys.-Condensed Matter **5**, 1681 (1993).

[30] M. Matsui, and W. Busing, American Mineralogist **69**, 1090 (1984).

[31] R. Newnham, and H. Yoon, Mineralogical Mag. **39**, 78 (1973).

[32] R. G. Ross, P. Andersson, B. Sundqvist, and G. Backstrom, Rep. Prog. Phys. **47**, 1347 (1984).

[33] G. A. Slack, in *Solid State Physics* (Academic, New York, 1979) **34**, 35.

[34] M. Roufosse, and P. G. Klemens, Phys. Rev. B **7**, 5379 (1973).

[35] F. D. Stacey, and D. E. Loper, Phys. Earth Planet. Inter. **36**, 99 (1984).

[36] A. M. Leitch, Phys. Earth Planet. Inter. **89**, 89 (1995).

[37] F. Dubuffet, D. A. Yuen, and M. Rabinowicz, Earth Planet. Sci. Lett. **171**, 401 (1999).

[38] A. M. Hofmeister, and D. A. Yuen, J. Geodyn. **44**, 186 (2007).

[39] J. B. Naliboff, and L. H. Kellogg, Geophys. Res. Lett. **33** (2006).

[40] R. E. Cohen, Rev. High Pressure Sci. Technol. **7**, 160 (1998).

[41] N. de Koker, Phys. Rev. Lett. **103**, 125902 (2009).

[42] N. de Koker, Earth Planet. Sci. Lett. **292**, 392 (2010).

[43] X. L. Tang, and J. J. Dong, Phys. Earth Planet. Inter. **174**, 33 (2009).

[44] A. M. Hofmeister, Science **283**, 1699 (1999).

[45] H. K. Mao, P. M. Bell, J. W. Shaner, and D. J. Steinberg, J. Appl. Phys. **49**, 3276 (1978).

[46] N. W. Ashcroft, and N. D. Mermin, in *Solid State Physics*, (Saunders, Philadelphia, 1976).

[47] C. S. Zha, H. K. Mao, and R. J. Hemley, PNAS, USA **97**, 13494 (2000).

[48] A. Chopelas, Phys. Chem. Miner. **17**, 142 (1990).

[49] A. Chopelas, and M. Nicol, J. Geophys. Res. **87**, 8591 (1982).

[50] S. Ghose, M. Krisch, A. R. Oganov, A. Beraud, A. Bosak, R. Gulve, R. Seelaboyina, H. Yang, and S. K. Saxena, Phys. Rev. Lett. **96**, 035507 (2006).

[51] J. Hama, and K. Suito, Phys. Earth Planet. Inter. **114**, 165 (1999).

[52] J. Slater, in *Introduction to Chemical Physics (McGraw-Hill, New York,* 1939*)*.

[53] A. Chopelas, Earth Planet. Sci. Lett. **114**, 185 (1992).

[54] T. S. Duffy, R. J. Hemley, and H. K. Mao, Phys. Rev. Lett. **74**, 1371 (1995).

[55] S. Speziale, C. S. Zha, T. S. Duffy, R. J. Hemley, and H. K. Mao, J. Geophys. Res. -Solid Earth **106**, 515 (2001).

[56] D. G. Isaak, R. E. Cohen, and M. J. Mehl, J. Geophys. Res. -Solid Earth and Planets **95**, 7055 (1990).

[57] B. Chen, W. P. Hsieh, D. G. Cahill, D. Trinkle, and J. Li, Phys. Rev. B **83**, 132301 (2011).

CHAPTER 4

TESTING THE MINIMUM THERMAL CONDUCTIVITY MODEL USING HIGH PRESSURE

Parts of this chapter were published in *Phys. Rev. B* **83**, 174205 (2011) by Wen-Pin Hsieh, Mark Losego, Paul Braun, Sergei Shenogin, Pawel Keblinski, and David G. Cahill.

4.1 Introduction

The minimum thermal conductivity model was originally proposed by Einstein and later modified by Cahill and coworkers [1, 2]. This model assumes that the thermal energy is transported by harmonic interactions between atoms vibrating with random phases. Using a harmonic Green-Kubo formalism, Allen and Feldman [3, 4] provided a more rigorous foundation for this minimum thermal conductivity model. To classify the vibrational modes in disordered materials, Allen and Feldman also introduced the following phonon categories: locons, diffusons, and propagons. Locons are localized vibrational modes and do not contribute to thermal transport under the harmonic

approximation. Propagons, analogous to the phonons in crystals, are wave-like acoustic vibrational modes. Diffusons are non-propagating, diffusive vibrational modes and play a dominant role in the thermal transport. Based on these ideas and assuming that the density of vibrational states follows a Debye-like distribution, the thermal conductivity of most amorphous materials as well as many strongly disordered crystals can be accurately predicted from elastic constants and atomic density of the materials. (An exception was recently reported for amorphous Si deposited by hot-wire chemical vapor deposition [5], where the measured thermal conductivity is a factor of 4 larger than the predicted thermal conductivity based on the minimum thermal conductivity model.) In the high temperature limit in which all vibrational modes are thermally excited, the predicted minimum thermal conductivity is $\Lambda_{\min} = 0.40 k_B n^{2/3} \left(v_l + 2v_t \right)$, where n is the atomic density and v_l and v_t are the longitudinal and transverse speeds of sound, respectively [2].

However, the validity of this thermal transport mechanism for amorphous polymers is questionable; the density of vibrational states of an amorphous polymer substantially deviates from a Debye-like distribution due to the coexistence of strong covalent bonding within the polymer backbone and side groups with weak non-bonding van der Waals interactions between chains. In addition, since the non-bonding van der Waals interactions are significantly non-linear, the effect of "fracton hopping" [6] due to

the anharmonic interactions between localized modes could also contribute to thermal transport. Recently molecular dynamics simulations of polystyrene [7] and proteins [8, 9] have shown the importance of anharmonicity in the thermal conductivity of amorphous polymers. Pressure tuning of the thermal conductivity enables a critical test of the minimum thermal conductivity model by enabling a continuous variation of the atomic density and elastic constants.

Due to the limitations of the types of pressure cells, previous studies on the pressure dependent thermal conductivity of polymers [10-12] extend to only $P \approx 2$ GPa. Diamond or SiC anvil cell techniques [13-15] can easily generate the high pressures needed to substantially alter the elastic constants of a polymer. For instance, the pressure dependence of the elastic constant C_{11} of a typical glassy polymer is on the order of $C_{11} \approx$ 8 GPa+7P, hence C_{11} increases by an order of magnitude to $C_{11} \approx 80$ GPa at P=10 GPa, which is comparable to the elastic constants of Al at ambient conditions.

4.2 Experiments

4.2.1 Growing polymers on the SiC anvil

Poly(methyl methacrylate) (PMMA) chains grown on SiC anvils were prepared by Dr. Mark Losego in Prof. Paul Braun's group at the University of Illinois. SiC anvils

with a culet size of ≈600 μm were first etched in 10 % HF solutions, rinsed in deionized water, and sonicated in chloroform, followed by ethanol to remove residues and contaminants. A piranha solution (3:1 H_2SO_4 /H_2O_2 (v/v)) was then used to hydroxylate the SiC anvil surface and to facilitate chemical attachment of the radical initiator, (11-(2-bromo-2-methyl)propionyloxy) undecyltrichlorosilane [16].

PMMA brushes were grown from these surfaces using atom-transfer radical polymerization (ATRP) [17]. The term "brush" refers to polymer chains covalently bonded to a substrate at a spacing shorter than the radius of gyration [18]. In the ATRP method, the SiC anvil surface was first functionalized with a self-assembled monolayer having a bromine termination. Methyl methacrylate monomers were then polymerized from this bromine initiator by using copper (I) chloride as the atom-transfer catalyst that abstracts the bromine from the SiC surface and initiates the radical polymerization process. Figure 4.1 shows the schematic illustration of the ATRP method.

By increasing polymerization time the thickness of the brush and molecular weight of the PMMA chains increased. The thickness of the PMMA brush was determined by using picosecond acoustics combined with a simulation of the acoustics signals based on Ref. [19], see section 2.1.5 for the details. By the film thickness and the molecular weight, a grafting density is determined to be ≈0.6 chains nm^{-2}, which

indicates sufficient overlap to force the extension of polymer chains into the brush regime[18].

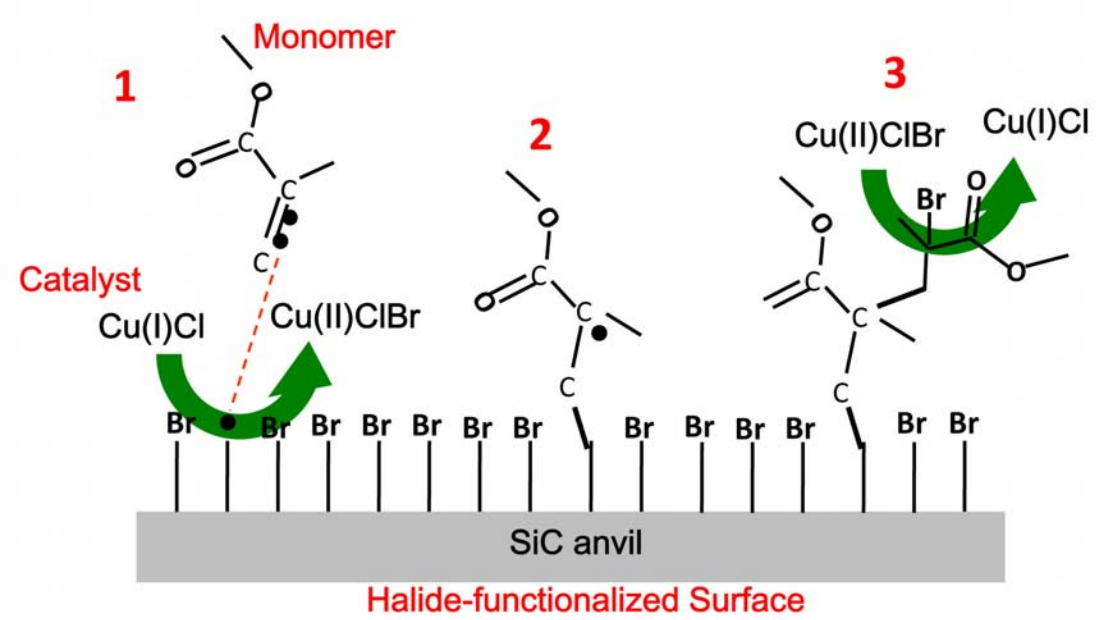

Fig. 4.1. Schematic illustration of the atom-transfer radical polymerization method. In step (1), Cu(I)Cl abstracts a Br atom from the SiC surface, giving a propagating radical; (2) a monomer, methyl methacrylate, is attached on the radical and then polymerized; (3) the brush grows until the radical is capped.

An 80 nm-thick Al film was deposited on the PMMA brushes using magnetron sputtering and serves as an optical transducer for time-domain thermoreflectance (TDTR) measurements. The SiC anvil cell was pressurized by cryogenically loading with Ar or by loading with H_2O as the pressure medium. (Since at room temperature Ar is a liquid at *P*

<1.3 GPa and sometimes leaked from the cell, H_2O was used for thermal measurements at P <1.4 GPa. At room temperature and P >1.3 GPa, the equilibrium phase of the cryogenically-loaded Ar is a hcp crystal [20].) I determined the pressure by measuring ruby fluorescence [21]. Figure 4.2 shows the configuration of the Al-coated PMMA sample in the SiC anvil cell and TDTR measurements.

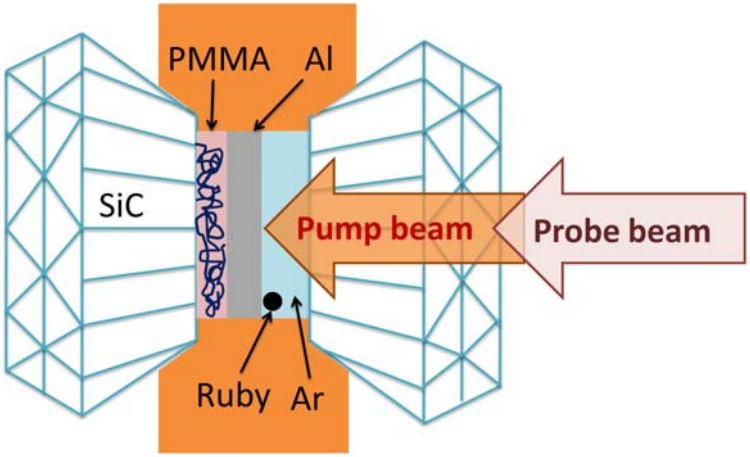

Fig. 4.2. Schematic drawing of a TDTR measurement on PMMA brushes in a SiC anvil cell. Ar is the typical pressure medium for measurements at P >1.3 GPa; H_2O was used for measurements at P <1.4 GPa.

4.2.2 Thermal conductivity measurements by TDTR

I measured the thermal conductivity Λ of PMMA brushes at room temperature by comparing the TDTR [22-24] data with calculations using a thermal model [25] which

takes into account heat flow through the polymer layer and into the SiC substrate as well as heat flow into the pressure medium [26].

There are several parameters in the thermal model—laser spot size, and the thickness, heat capacity and thermal conductivity of each layer—but the thermal conductivity Λ of the PMMA layer is the only significant unknown. The PMMA layers are chosen to be thin (< 25 nm) so that most of the heat flows into the SiC anvil, which has a high thermal conductivity, and only a small fraction of the heat flows into the pressure medium, which has a much lower thermal conductivity. Uncertainties in the thermal conductivity and heat capacity of the pressure medium propagate less than 2% error in the thermal conductivity measured for the thickest (22 nm) PMMA layers at P=10 GPa.

The thickness of the Al film at ambient pressures was determined by picosecond acoustics and its changes under pressure was calculated by the equation of state $B_T = 73 + 4.54P$ [27] and by assuming that the Al film deforms plastically and adheres well to the PMMA layers and that SiC does not have lateral compression. Estimates of the pressure dependence of the heat capacity of Al are discussed in Chapter 3. Figure 4.3 shows the pressure dependence of the thickness and heat capacity per unit area of Al film. I also calculated changes in the thickness of PMMA by its equation of

state. (The approach for determining the equation of state is described below.) Since the PMMA layers are thermally thin, the thermal model is not sensitive to the heat capacity of the PMMA brush.

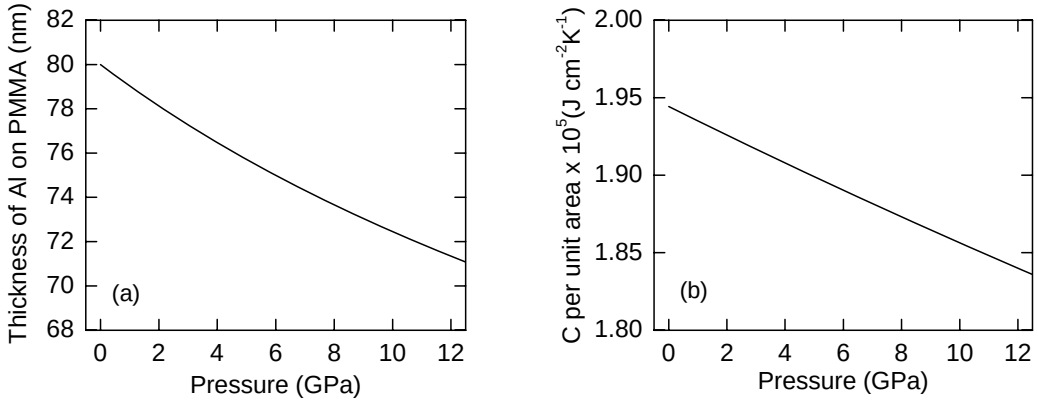

Fig. 4.3. (a) Pressure dependence of the thickness of an Al film (80 nm thick at ambient) on PMMA/SiC. **(b)** Heat capacity per unit area, product of volumetric heat capacity and thickness in (a), of Al as a function of pressure.

4.2.3 Measurements of elastic constants

Elastic constants of PMMA were measured by time-domain stimulated Brillouin scattering [15, 28, 29], in which the thickness of the PMMA is required to be thicker than half of the laser wavelength (~785 nm). Therefore I measured the elastic constant C_{11} of a thick (>1μm), spun-cast PMMA layer. In a backscattering geometry, the Brillouin frequency in longitudinal modes is $f_B = 2Nv_l / \lambda$, where N is the refractive index, v_l is the longitudinal sound velocity, and λ=785 nm is the laser wavelength. The pressure

dependence of f_B is shown in Fig. 4.4(a).

The equation of state and elastic constant C_{11} of PMMA, see Fig. 4.4(b), are determined by a self-consistent and iterative approach. To begin, I use a trial function for the isothermal bulk modulus B_T=6 GPa+6P and calculate the pressure dependence of the density $\rho(P)$, index of refraction $N(P)$, and $C_{11}(P)$ using the Lorentz-Lorenz formula $(N^2-1)/(\rho(N^2+2))=A$, where A is a constant [15], combined with the picosecond acoustics data. (At ambient pressure ρ=1.19 g cm^{-3} and A=0.241.) If the Poisson ratio ν can be assumed to be a constant ν=1/3, the isothermal bulk modulus $B_T(P)=(2/3)C_{11}(P)$. I then fit this $B_T(P)$ to a second order polynomial in P and calculate the pressure dependence of the molecular density n from $B_T=n(dP/dn)_T$.

This procedure is iterated until C_{11} and B_T are self-consistent; the final equation of state is $B_T=B_0+B_1P+B_2P^2$, where B_0=6.15 GPa, B_1=7, and B_2=−0.17 GPa^{-1}. Based on this equation of state, the atomic density n increases by 31% at 5 GPa and 46% at 10 GPa. Here, I assume that the amorphous polymer plastically deforms under high pressure so that the state of stress is close to hydrostatic. (At low pressures, the yield strength of PMMA is $\tau_y \approx$ 0.05 GPa+0.2P [30].)

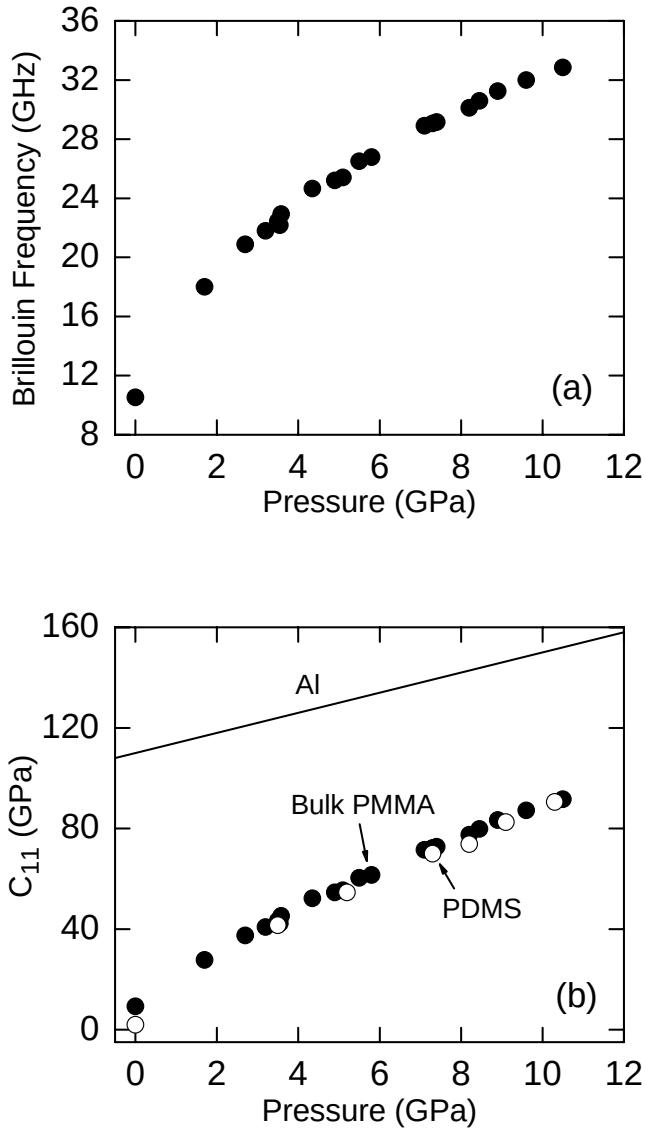

Fig. 4.4. Pressure dependence of the **(a)** Brillouin frequency and **(b)** C_{11} of a spun-cast layer of PMMA. C_{11} is derived from the Brillouin frequency data using a self-consistent equation of state of PMMA and the assumptions that the Poisson ratio is constant and the refractive index follows the Lorentz-Lorenz equation. Data for Polydimethylsiloxane (PDMS) [31] and previously estimated C_{11}= 110 GPa+4P of Al [27] are plotted for comparison.

4.3 Results and discussion

4.3.1 Thermal conductivity of PMMA

Figure 4.5 presents the pressure dependence of the thermal conductivity $\Lambda(P)$ of PMMA brushes (solid symbols) with different thicknesses. $\Lambda(P)$ is independent of the thickness h when $h > 6$ nm and increases monotonically with increasing P. The uncertainty in my thermal conductivity measurements is estimated to be ≈10 % and is dominated by uncertainties in the thicknesses of PMMA and Al. For comparison, I also measured $\Lambda(P)$ of a 10 nm thick spun-cast PMMA (open diamond) and found the spun-cast and brush forms of PMMA show the same behavior. The thermal conductivity at ambient pressure, $\Lambda \approx 0.185$ W m^{-1} K^{-1}, agrees well with the literature value, $\Lambda \approx 0.20$ W m^{-1} K^{-1} (open square) [32, 33]; in the low pressure regime, the weaker pressure dependence is similar to that of previous work by Andersson and Ross (open circle) [10] whose ambient conductivity, 0.225 W m^{-1} K^{-1}, is ≈10 % higher than the data reported in Refs. [32, 33].

The result that brushes and spun-cast PMMA have the same behavior is consistent with a previous work by my collaborators who studied the thickness dependence of the effective thermal conductivity at ambient pressure [34]. In my experiments, the dry PMMA brushes are amorphous and the extension of polymer chains is relatively short; in

the previous work, the brushes were estimated to extend to only 25% of their contour length, and the increase in the thermal conductivity due to the small chain extension is only comparable to the uncertainties of the data shown in Fig. 4.5.

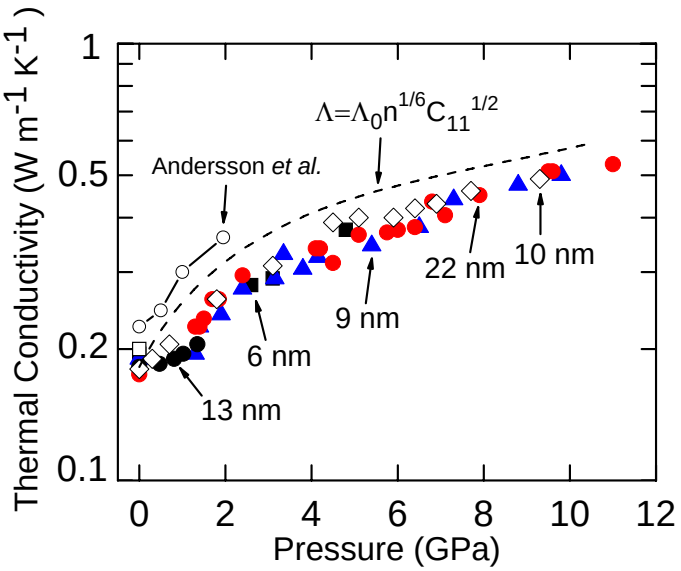

Fig. 4. 5. Measurements of the thermal conductivity of PMMA brushes (solid symbols) and a spun-cast layer (open diamond) as a function of pressure. The uncertainty in the thermal conductivity and pressure measurements are ≈10 % and 0.2 GPa, respectively. Ar was the pressure medium for all measurements except for those of the 13 nm brushes and 10 nm spun-cast layer where H_2O was used. The dashed line shows the predicted thermal conductivity of PMMA based on the minimum thermal conductivity model, the pressure dependence of the atomic density *n,* and the elastic constant C_{11} obtained by a polynomial fit. Data for bulk PMMA by Andersson *et al.* (open circle) [10] and by Cahill *et al.* and Putnam *et al.* (open square) [32, 33] are included for comparison. Lines between Andersson's data are added to emphasize that the pressure dependence of the prior data are similar to that of my measurements in the low pressure regime.

Data sets for 9 and 22 nm-thick brushes and the 10 nm-thick spun-cast layer include measurements for both increasing and decreasing pressure. The lack of hysteresis shows that any structural changes in the PMMA under pressure are reversible.

The measurements of the thermal conductivity of PMMA films include the contribution to the thermal resistance from the bulk of the polymer layer as well as the thermal resistance of the Al/PMMA and PMMA/SiC interfaces. I have not experimentally determined the series sum of the thermal conductance of Al/PMMA and PMMA/SiC interfaces; instead, I estimate the interface thermal conductance $G \approx 300$ MW m^{-2} K^{-1} based on the previous study [34]. Using this estimation, the sum of the Kapitza lengths of Al/PMMA and PMMA/SiC interfaces is small, $l_K = \Lambda / G \sim 1$ nm, and therefore I do not expect a significant reduction in the effective thermal conductivity of PMMA caused by the finite interface thermal conductance even for the thinnest, 6 nm, brushes.

Data for $\Lambda(P)$ is also compared with the prediction by the minimum thermal conductivity model Λ_{min} [2], see Fig. 4.5. In the high temperature limit, the minimum thermal conductivity Λ_{min} depends only on atomic density n and the sound velocities $v_l = \sqrt{C_{11}/\rho}$ and $v_t = \sqrt{C_{44}/\rho}$. If the ratio C_{11}/C_{44} is assumed to be approximately constant under pressure, the pressure dependence of Λ_{min} simplifies to $\Lambda_{min} = \Lambda_0 n^{1/6} C_{11}^{1/2}$. A fit to the average of the data at ambient pressure Λ= 0.185 W m^{-1}

K^{-1} using $n=4.3\times10^{28}\ m^{-3}$ and C_{11}=9.2 GPa gives $\Lambda_0 = 3.25\times10^{-11}\ J^{1/2}\,m\,K^{-1}\,s^{-1}$. The dashed line in Fig. 4.5 shows $\Lambda_{min} = \Lambda_0 n^{1/6} C_{11}^{1/2}$ using the C_{11} [Fig. 4.4 (b)] derived from the polynomial fit and n obtained from the equation of state $B_T = n(dP/dn)_T$ as described above.

Note that the $\Lambda(P)$ can also be approximated by a simple function of pressure. In the high pressure limit, the elastic constant C_{11} is roughly linear in P, and $n^{1/6}$ is essentially a constant. Thus, the predicted thermal conductivity can be expressed as $\Lambda = \Lambda_1 + \Lambda_2 P^{1/2}$, where Λ_1 = 0.185 W m^{-1} K^{-1} is the thermal conductivity at ambient pressure and $\Lambda_2 \approx 0.11$ W m^{-1} K^{-1} $GPa^{-1/2}$.

As shown in Fig. 4.5, the predicted pressure dependence of the thermal conductivity based on $\Lambda_{min} = \Lambda_0 n^{1/6} C_{11}^{1/2}$ captures well the trends in the data and accurately predicts $\Lambda(P)$ at higher pressures. Note, however, that in the low pressure regime, P<1 GPa, the data deviate slightly from the prediction of the minimum thermal conductivity model but the difference is relatively small and comparable to the experimental uncertainties, ≈10 %. (Andersson's data show a similar deviation from the model prediction even after using another $\Lambda_0 = 3.95\times10^{-11}\ J^{1/2}\,m\,K^{-1}\,s^{-1}$ to fit their data in Ref. [10] at ambient pressure.) The good agreement between my data and the model prediction over the entire pressure range supports the idea that the dominant mechanism

of thermal transport in glassy polymers is the exchange of thermal energy between non-propagating vibrational modes [35].

4.3.2 Thermal conductivity of polystyrene by molecular dynamics simulations

To gain further insight into the mechanism of heat transport in amorphous polymers, and to evaluate the generality of my findings shown in the previous section, Dr. Sergei Shenogin and Prof. Pawel Keblinski of Rensselaer Polytechnic Institute calculated the pressure dependent thermal conductivity of a model of polystyrene (PS) using molecular dynamics (MD) simulations. Although another study of the thermal conductivity of polystyrene under pressure by MD simulations was recently reported by Algaer *et al.* [36], their results did not show significant dependence on the elastic constants because they only studied pressures up to 60 MPa. Details of the MD simulations are described in Ref. [37].

Figure 4.6 depicts the pressure dependence of the thermal conductivity $\Lambda(P)$ of PS calculated by our MD simulations. The solid line shows the predicted Λ based on the minimum thermal conductivity model $\Lambda_{\min} = \Lambda_0 n^{1/6} C_{11}^{1/2}$, where $\Lambda_0 = 5.66 \times 10^{-11}$ J$^{1/2}$ m K^{-1}s^{-1} is determined by fitting $\Lambda_{\min} = 0.20$ W m^{-1} K^{-1} at ambient pressure. The model

prediction agrees well with the MD simulations, indicating that the heat transport mechanism in amorphous polystyrene is the same as the mechanism described by the minimum thermal conductivity model. Furthermore, the fact that the minimum thermal conductivity model describes well the data for both PMMA and PS suggests that indeed amorphous polymers share a universal thermal transport mechanism where thermal energy is transferred predominately through the diffusion of thermal energy between non-propagating vibrational modes.

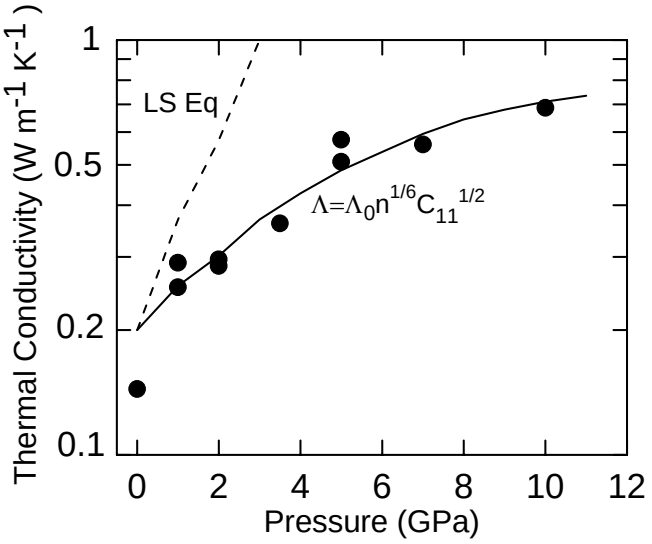

Fig. 4.6. Pressure dependence of the thermal conductivity of polystyrene by molecular dynamics simulations (solid circles). The solid line shows the predicted thermal conductivity by the model of the minimum thermal conductivity. The dashed line shows the pressure dependence of the thermal conductivity predicted by the Leibfried-Schlömann equation using the scaling $\omega_D \propto \sqrt{C_{11}}$.

Compared to the relatively weak pressure dependence of thermal conductivity predicted by the minimum thermal conductivity model, the Leibfried-Schlömann equation, as discussed in Chapter 3, is often used to describe the thermal conductivity of isotropic crystals and predicts much stronger pressure dependence:

$$\Lambda_{LS} = A\frac{V^{\frac{1}{3}}\omega_D{}^3}{\gamma^2 T}, \qquad (4.1)$$

where V is the volume, ω_D the Debye frequency, γ the Grüneisen parameter, T the temperature, and A is a constant under pressure [38, 39]. If I assume that γ is also a constant in the pressure range of $0<P<12$ GPa and that the Debye frequency scales with the square root of elastic constant, i.e., $\omega_D \propto \sqrt{C_{11}}$, then the predicted thermal conductivity $\Lambda(P)$ based on Eq. (4.1) is shown as the dashed line in Fig.4.6. The distinctly different pressure dependence of Λ predicted by the LS equation supports my conclusion that diffusion of thermal energy between non-propagating vibrational modes dominates the heat conduction in amorphous polymers. The propagation of wave-like vibrational modes, the dominant mechanism of heat conduction in crystals, plays a minor role in the amorphous polymers.

4.4 Conclusion

I present my studies of the pressure dependence of elastic constants and thermal conductivity of PMMA using time-domain stimulated Brillouin scattering and time-domain thermoreflectance combined with SiC anvil cell techniques. The minimum thermal conductivity model can well describe the pressure dependent thermal conductivity of PMMA by TDTR measurements and polystyrene by MD simulations, suggesting that heat diffusion between non-propagating vibrational modes can mostly capture the basic heat transport mechanism in amorphous polymers and contributions to heat transport from localized excitations and anharmonic effects are minor considerations.

4.5 References

[1] A. Einstein, Ann. Phys. **35**, 679 (1911).

[2] D. G. Cahill, S. K. Watson, and R. O. Pohl, Phys. Rev. B **46**, 6131 (1992).

[3] P. B. Allen, and J. L. Feldman, Phys. Rev. B **48**, 12581 (1993).

[4] P. B. Allen, J. L. Feldman, J. Fabian, and F. Wooten, Philosophical Magazine B **79**, 1715 (1999).

[5] H. S. Yang, D. G. Cahill, X. Liu, J. L. Feldman, R. Crandall, B. Sperling, and J.

Abelson, Phys. Rev. B **81**, 104203 (2010).

[6] S. Alexander, O. Entinwohlman, and R. Orbach, Phys. Rev. B **34**, 2726 (1986).

[7] S. Shenogin, A. Bodapati, P. Keblinski, and A. McGauphey, J. Appl. Phys. **105**, 034906 (2009).

[8] D. M. Leitner, Annu. Rev. Phys. Chem. **59**, 233 (2008).

[9] X. Yu, and D. M. Leitner, J. Chem. Phys. **122**, 054902 (2005).

[10] S. P. Andersson, and R. G. Ross, International J. of Thermophys. **15**, 949 (1994).

[11] R. E. Barker, R. Y. S. Chen, and R. S. Frost, J. Polymer Sci. B **15**, 1199 (1977).

[12] R. S. Frost, R. Y. S. Chen, and R. E. Barker, J. Appl. Phys. **46**, 4506 (1975).

[13] E. H. Abramson, J. M. Brown, and L. J. Slutsky, J. Chem. Phys. **115**, 10461 (2001).

[14] P. Beck, A. Goncharov, V. Struzhkin, B. Militzer, H. K. Mao, and R. Hemley, Appl. Phys. Lett. **91**, 181914 (2007).

[15] W. P. Hsieh, B. Chen, J. Li, P. Keblinski, and D. G. Cahill, Phys. Rev. B **80**, 180302 (2009).

[16] S. Boyes, A. M. Granville, and W. J. Brittain, Macromolecular Synthesis **13**, 15 (2004).

[17] C. B. Gorman, R. J. Petrie, and J. Genzer, Macromolecules **41**, 4856 (2008).

[18] Y. Tsujii, K. Ohno, S. Yamamoto, A. Goto, and T. Fukuda, Surface-Initiated

Polymerization I **197**, 1 (2006).

[19] C. Thomsen, H. Grahn, H. Maris, and J. Tauc, Phys. Rev. B **34**, 4129 (1986).

[20] J. Wittlinger, R. Fischer, S. Werner, J. Schneider, and H. Schulz, Acta Cryst. B **53**, 745 (1997).

[21] H. K. Mao, P. Bell, J. Shaner, and D. Steinberg, J. Appl. Phys. **49**, 3276 (1978).

[22] D. G. Cahill, W. Ford, K. Goodson, G. Mahan, A. Majumdar, H. Maris, R. Merlin, and S. Phillpot, J. Appl. Phys. **93**, 793 (2003).

[23] C. A. Paddock, and G. L. Eesley, J. Appl. Phys. **60**, 285 (1986).

[24] D. A. Young, C. Thomsen, H. Grahn, H. Maris, and J. Tauc, in *Phonon Scattering in Condensed Matter*, edited by A. C. Anderson and J. P. Wolfe (Springer, Berlin, 1986).

[25] D. G. Cahill, Rev. Sci. Instrum. **75**, 5119 (2004).

[26] Z. B. Ge, D. G. Cahill, and P. V. Braun, Phys. Rev. Lett. **96**, 186101 (2006).

[27] C. Bercegeay, and S. Bernard, Phys. Rev. B **72**, 214101 (2005).

[28] K. E. O'Hara, X. Y. Hu, and D. G. Cahill, J. Appl. Phys. **90**, 4852 (2001).

[29] C. Thomsen, H. Grahn, H. Maris, abd J. Tauc, Opt. Commun. **60**, 55 (1986).

[30] S. Rabinowitz, I. M. Ward, and J. S. C. Parry, J. Mater. Sci. **5**, 29 (1970).

[31] L. L. Stevens, E. Orler, D. Dattelbaum, M. Ahart, and R. J. Hemley, J. Chem. Phys. **127**, 104906 (2007).

[32] D. G. Cahill, and R. O. Pohl, Phys. Rev. B **35**, 4067 (1987).

[33] S. A. Putnam, D. G. Cahill, B. Ash, and L. Schadler, J. Appl. Phys. **94**, 6785 (2003).

[34] M. D. Losego, L. Moh, K. Arpin, D. G. Cahill, and P. Braun, Appl. Phys. Lett. **97**, 011908 (2010).

[35] J. L. Feldman, M. Kluge, P. Allen, and F. Wooten, Phys. Rev. B **48**, 12589 (1993).

[36] E. A. Algaer, M. Alaghemandi, M. Bohm, and F. Muller-Plathe, J. Phys. Chem. A **113**, 11487 (2009).

[37] W. P. Hsieh, M. Losego, P. Braun, S. Shenogin, P. Keblinski, and D. G. Cahill, Phys. Rev. B **83**, 174205 (2011).

[38] G. A. Slack, in *Solid State Physics* (Academic, New York, 1979) **34**, 35.

[39] M. Roufosse, and P. G. Klemens, Phys. Rev. B **7**, 5379 (1973).

CHAPTER 5

PRESSURE TUNING OF THE INTERFACE THERMAL CONDUCTANCE

Parts of section 5.1 will be published in "Pressure tuning of the thermal conductance of weak interfaces" by Wen-Pin Hsieh, Austin S. Lyons, Eric Pop, Pawel Keblinski, and David G. Cahill, *submitted for publication*.

5.1 Pressure tuning of thermal transport across weak interfaces

Thermal transport across interfaces is characterized by the interface thermal conductance $G : J = G\Delta T$, where J is the heat flux across the interface and ΔT the temperature drop at the interface. The interface thermal conductance plays a critical role in controlling thermal conduction in nanostructures [1], nanoscale composites [2, 3], and superlattices [4]. For example, a high density of interfaces can reduce the thermal conductivity of materials below a value predicted by the minimum thermal conductivity model for amorphous limit [5, 6] and therefore may find applications in

improving thermoelectric energy conversion [7].

The acoustic mismatch model (AMM), diffuse mismatch model (DMM), and phonon radiation limit (PRL) are conventional theories [8] used to predict and compare the experimental data for interface thermal conductance. These models assume perfect contact (e.g., strong bonding) at the interface between materials and that the interface thermal conductance is determined only by the lattice dynamics, such as acoustic and vibrational properties, of the bulk materials on each side of the interface; the acoustic and vibrational properties of the interface itself are not included in these models. In the AMM, in analogy with transmission line theory, the phonon transmission at the interface is derived from acoustic impedances, the products of the mass density and speeds of sound. In this model, large mismatch in acoustic impedances leads to smaller interface thermal conductance G. The DMM, on the other hand, assumes strong phonon scattering at the interface, and that the phonon transmission is simply governed by the relative density of phonon vibrational states in the materials on either side of the interface. In the DMM, the more dissimilar the densities of phonon vibrational states, the smaller the value of G.

The PRL predicts the maximum possible thermal conductance involving a harmonic two-phonon process [9, 10]. Considering the interface studied here, Al/SiC, the PRL assumes that phonons incident from SiC into Al have a transmission

coefficient of unity for all phonons in SiC with frequencies lower than the highest frequency vibrational mode of Al, ν_{max}. For phonons in SiC with frequencies higher than the ν_{max}, the transmission coefficient is zero. Thus, the prediction of PRL is a function of the highest frequency ν_{max} of Al as well as the phonon density of states of SiC.

The importance of interface bonding on thermal transport at interfaces [11-17] has been discussed for decades. For example, anomalously high thermal conductance of Pb/diamond interfaces was attributed to the enhanced interface bonding between Pb and diamond [11]. Using a lattice-dynamics model, Young and Maris [17] showed that when interface spring constant is much smaller than the bulk spring constants of two materials on either side of the interface, the phonon transmission at the interface is significantly reduced. More recently molecular dynamics simulations have demonstrated that low interface stiffness can substantially reduce the interface thermal conductance [12, 13]. Analytical models [14, 16] that include the effects of weak interface spring constants have shown that in the limit of extremely weak interfaces, G scales with the square of the interface spring constant, and as the interface stiffness is increased to the strong bonding limit, G approaches the value predicted by the AMM.

The interface stiffness S is related to an applied stress σ via $\sigma = S\Delta u$, where

Δu is the discontinuity in displacement created by the applied stress at the interface [18]. An interface between materials can be modeled as a thin layer with an elastic constant C_i and thickness t [19]. When an applied stress σ creates a strain ε on the interface layer, $\sigma = C_i \varepsilon$, where $\varepsilon = \Delta t / t$ and Δt is the displacement of the interface layer due to the applied stress. Then the interface stiffness *S* can be defined by C_i / t , the elastic constant of the interface layer per unit thickness.

Under pressure, the elastic properties of materials are changed [20]. This allows us to systematically vary the interface stiffness *S* and directly reveal the critical role that weak interface bonding plays in thermal conductance *G*. The interface stiffness *S*, analogous to the elastic constants of bulk materials, is expected to initially increase linearly with pressure $P, S(P) = S_0 + S_1 P$. As introduced in Chapter 1, modern gem anvil cell techniques [21, 22] can easily generate high pressures, typically *P*~10 GPa, needed to increase the small elastic constants of weak van der Waals interactions to values that are typical of strong chemical bonds [23].

In order to explore how the interface stiffness affects the interface thermal conductance, three types of interfaces with stiffness ranging from strong to weak were prepared: (1) a clean Al/SiC interface; (2) Al deposited on the native oxide of SiC, Al/SiO_x/SiC; and (3) a similar interface incorporating a monolayer graphene, i.e., Al/graphene/SiO_x/SiC. To produce the clean interface (1), a sputtering chamber was

constructed in which the SiC anvil is placed in a small diameter (5 mm), shallow hole (0.25 mm in depth) drilled in a thin graphite plate (0.5 mm in depth) and the graphite plate is then heated electrically to ≈1300 K for 30 minutes under a pressure of $\approx 5\times10^{-7}$ torr. The temperature of the graphite heater was measured by optical pyrometry. After the SiC anvil cools to near room temperature, an 80 nm-thick Al film was *in-situ* deposited on the clean SiC surface by magnetron sputtering without being exposed to air. Figure 5.1 shows the setup of the sputtering chamber and graphite plate heater.

The type (2) interface, Al/SiO_x/SiC, was prepared by depositing an 80 nm-thick Al film on the native oxide of the as-received SiC anvil at room temperature. The thickness of the native oxide on the as-received SiC anvil, ≈1 nm, was determined by the measured ratio, $R\approx3$, of the integrated intensities of Si-C to Si-O peaks in the Si 2p X-ray photoelectron spectrum [24]. The photoelectron current was measured at normal incidence.

To further weaken the interface stiffness, a monolayer of graphene was inserted between the Al and the native oxide layer on SiC, forming the type (3) interfaces, Al/graphene/SiO_x/SiC. The growth of monolayer graphene and subsequent transferring graphene onto the SiC anvil were completed by Austin Lyons in Prof. Eric Pop's group at the University of Illinois. Monolayer graphene was first grown on a Cu foil by chemical-vapor-deposition [25]. One side of the Cu foil was spin-coated

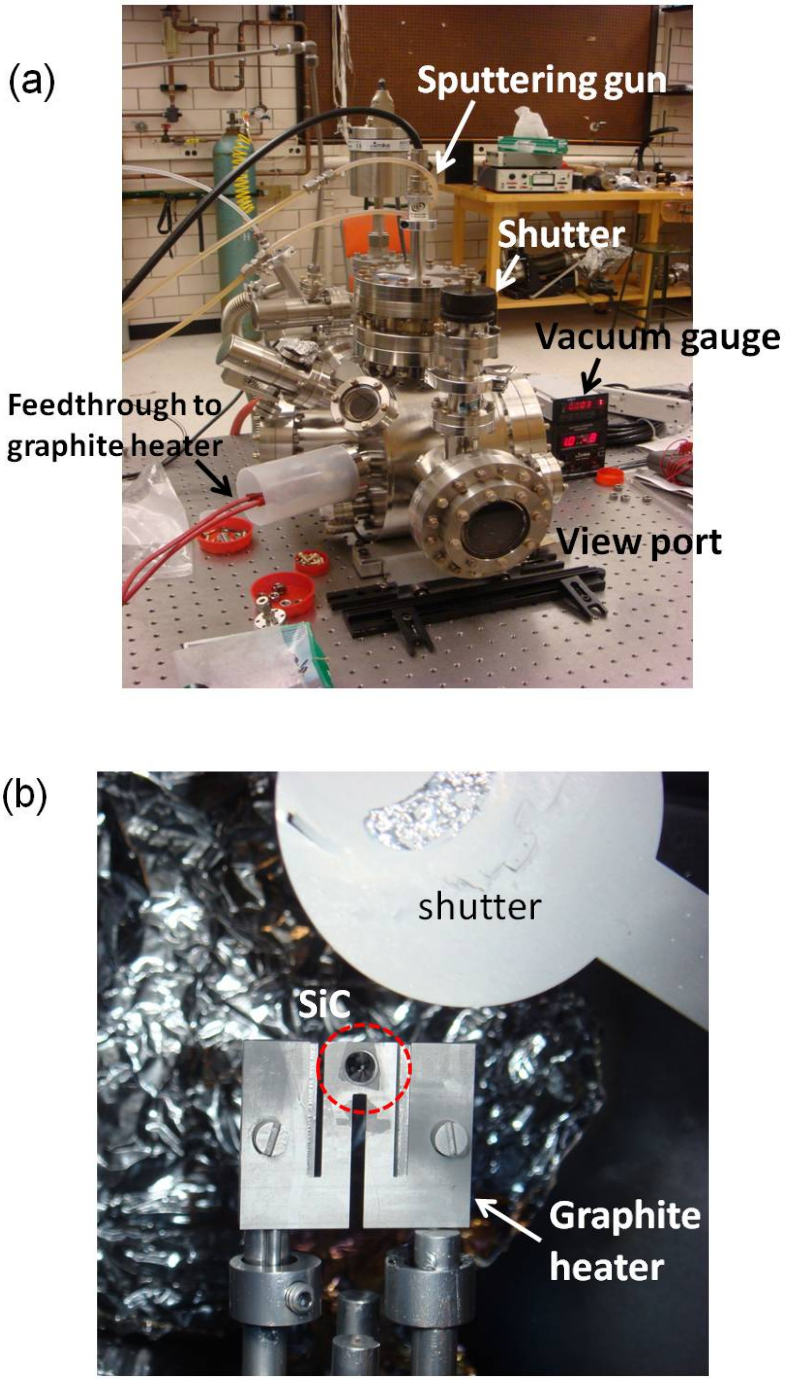

Fig. 5.1. (a) Setup of the sputtering chamber in which samples under study can be heated electrically up to ≈1650 K and *in situ* coated with metal films. **(b)** Home-made graphite plate heater (32×25.4 mm^2 and 0.5 mm thick). A SiC anvil, circled by red dashed lines, is placed in a small diameter (5 mm), shallow hole (0.25 mm in depth) drilled in the graphite plate.

with a 250 nm-thick poly(methyl methacrylate) (PMMA) layer, and the other side of the foil with extra graphene film was etched in an O_2 plasma, followed by an aqueous ferric chloride [25]. The PMMA and graphene were then rinsed in deionized water and transferred onto the SiC anvil. After using a 1:1 methylene-chloride/methanol solution to remove the PMMA carrier layer, the sample was annealed at ≈670 K for one hour at atmospheric pressure using a gas flow of 500 sccm H_2 and 500 sccm Ar to remove organic contaminants. The number of layers of the graphene transferred onto the SiC anvil was characterized by Raman spectroscopy; the full-width-at-half-maximum (FWHM) of the 2D peak of graphene, ≈34 cm^{-1}, confirms that the graphene is monolayer [26], see Fig. 5.2. (Bilayer graphene is easily distinguished from monolayer graphene by a significantly larger FWHM ≈60 cm^{-1} [26].)

Two types of "weak" interface samples containing graphene were prepared. First, the CVD-grown graphene was transferred directly onto the as-received SiC anvil. The other type of sample was prepared to test how the thickness of the native oxide layer affects the interface thermal conductance: the as-received SiC was first cleaned at high temperatures as described above and then exposed to ambient air for ~24 hours. X-ray photoelectron spectroscopy (XPS) data showed that the thickness of

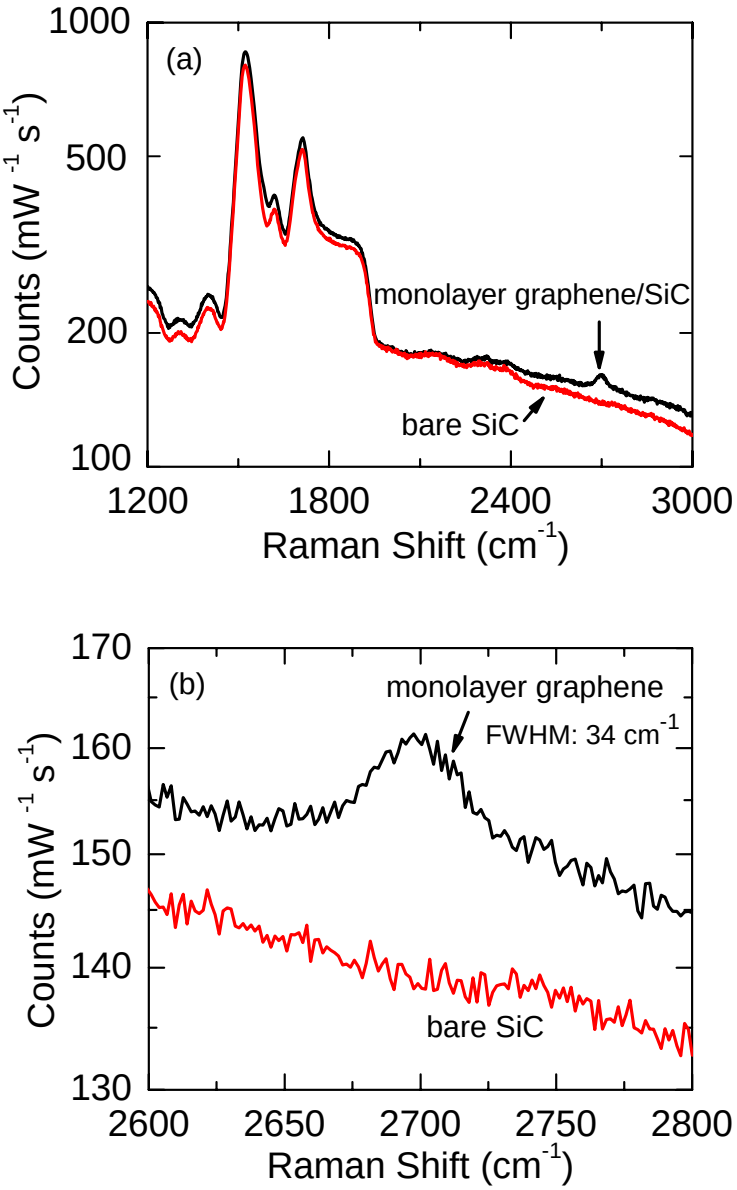

Fig. 5.2. (a) Raman spectra of a bare SiC (red curve) and a monolayer graphene on a SiC anvil (black curve) **(b)** Raman spectra around the wave number of 2700 cm^{-1}.The monolayer graphene is confirmed by the 2D peak near 2700 cm^{-1} with a full-width-at-half-maximum (FWHM) of 34 cm^{-1}.

the regrown native oxide layer was ≈0.5 nm. Both types of "weak"interface samples were heated to ≈420 K to remove surface volatile contaminants and then coated with Al films. The SiC anvil cells were pressurized by loading Ar or H_2O (the pressure

medium) into the sample chamber. The pressure was determined by ruby fluorescence [27].

The thermal conductance G of Al/SiC interfaces were measured using time-domain thermoreflectance (TDTR) [1, 30, 31] at room temperature and extracted using a thermal model that takes into account the heat flow through the interface layer and into the SiC substrate as well as into the pressure medium [28]. The thermal model contains several parameters—laser spot size ($w_0 \approx 6.5$ μm), and the thickness, heat capacity and thermal conductivity of each layer—but the thermal conductance of Al/SiC interfaces is the only significant unknown model parameter. The thickness of the Al film h_{Al} for each sample at ambient pressure was determined by picosecond acoustics [29]. I calculated the changes in Al thickness h_{Al} under pressure by assuming that the Al film deforms plastically and adheres well to the SiC anvil surface [30]; h_{Al} decreases by 5.4 % at 5 GPa and 9.4 % at 10 GPa. Estimates of the pressure dependence of the volumetric heat capacity of Al are described in Chapter 3. For an 80 nm-thick Al film, the heat capacity per unit area is $h_{Al}C = 1.94 \times 10^{-5}$ J cm^{-2} K^{-1} at ambient conditions and decreases by 4 % at 10 GPa.

Figure 5.3 shows example data for the type (2) Al/SiO_x/SiC interfaces and fits to the thermal model. At long time delays, the ratio V_{in}/V_{out} drops faster as the applied pressure increases, indicating that the interface thermal conductance increases with

pressure. Since the thermal conductivity of SiC anvil is much higher than the thermal conductivity of pressure medium, most of the heat created by the pump pulse flows into the SiC anvil and only a small fraction of the heat flows into the pressure medium. Thus, uncertainties in the thermal conductivity and volumetric heat capacity of the pressure medium propagate to less than ≈2 % error in the measurements of the interface thermal conductance *G*. The overall uncertainty in *G* is <8 % and is dominated by the uncertainty in the thickness of the Al film.

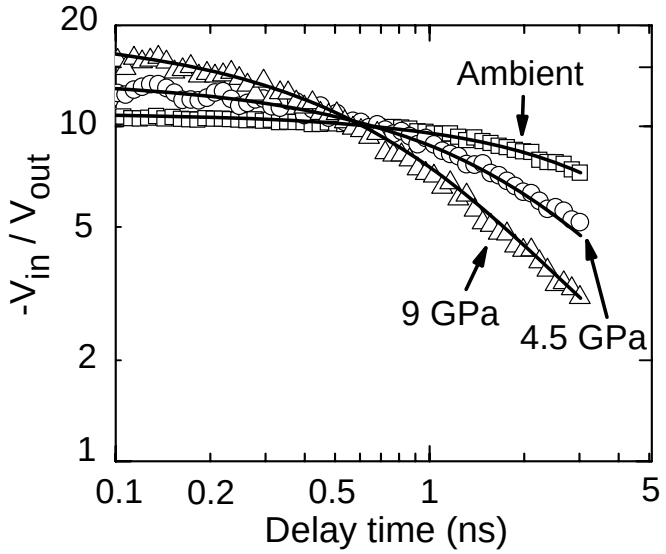

Fig. 5.3. Example data for time-domain thermoreflectance measurements on $Al/SiO_x/SiC$ interfaces and fits (solid lines) to the thermal model as described in Ref. [31]. Data and fits are labeled by the pressure. The interface thermal conductance is enhanced by the increasing pressure.

Figure 5.4(a) shows the pressure dependence of the thermal conductance $G(P)$ of the various Al/SiC interfaces. The thermal conductance of the clean Al/SiC interface (open circles) at ambient pressure is high, $G \approx 200$ $MWm^{-2}K^{-1}$, and is weakly

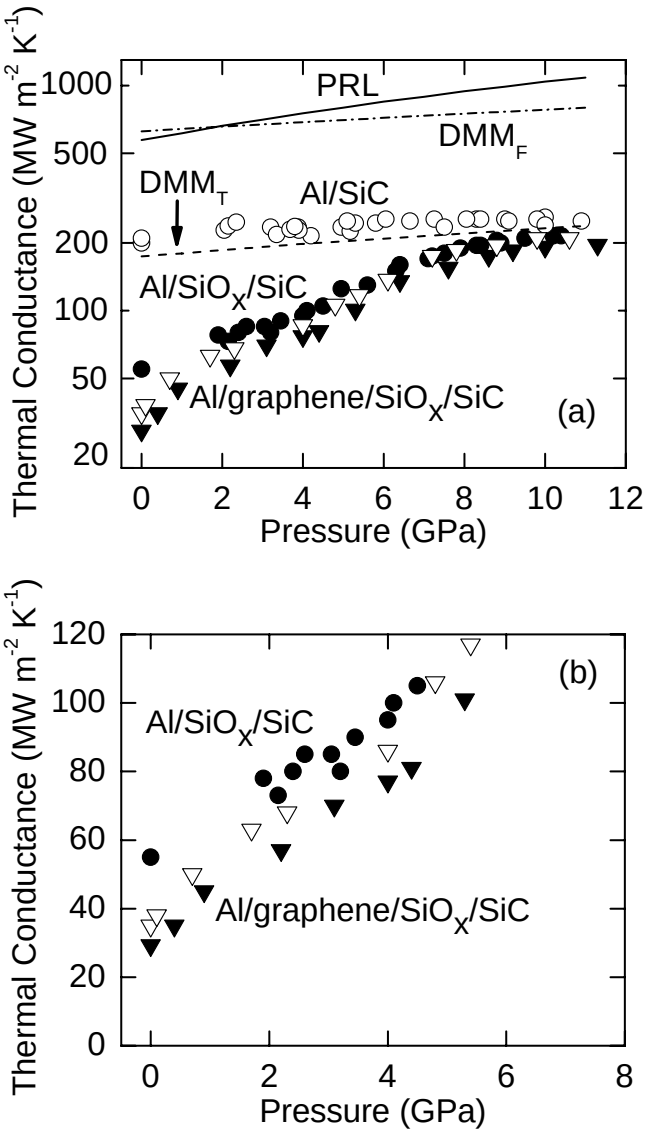

Fig. 5.4. (a) Pressure dependent thermal conductance $G(P)$ of various Al/SiC interfaces. $G(P)$ of the clean Al/SiC interface (open circles) is weakly dependent on the pressure. By contrast, $G(P)$ of the weak interfaces, Al/SiO_x/SiC (solid circles) and Al/graphene/SiO_x/SiC (open and solid triangles) increase rapidly with pressure due to the increasing interface stiffness, and saturate at P>8 GPa. The thickness of the native oxide on SiC for solid triangle data, ≈1 nm, is twice as thick as that for the open triangle data. The prediction of the $G(P)$ of Al/SiC interface by DMM_T is shown as the dashed line, which agrees well with the $G(P)$ of the clean interface but fails to describe the much stronger pressure dependence of $G(P)$ of weak interfaces. Predictions of the $G(P)$ of Al/SiC interface by DMM_F and PRL are shown as the dashed-dot and solid lines, respectively. **(b)** $G(P)$ of weak interfaces in the low pressure regime. The symbols for each interface are the same as in (a). All measured interface thermal conductances increase approximately linearly with pressure.

dependent on pressure. The large ambient value and weak pressure dependence of G suggests that the interface created by depositing Al on clean SiC is strongly bonded with high interface stiffness. In the limit of strong bonding, the diffuse mismatch model (DMM) should adequately predict the thermal conductance G.

The dashed line in Fig. 5.4(a) shows the DMM calculation for the $G(P)$ of type (1) Al/SiC interface based on a truncated Debye model, DMM_T. The program code for DMM calculations is provided by Prof. Yee Kan Koh of National University of Singapore. This approach is similar to that described in Ref. [32], in which the phonon dispersions in Al and SiC are assumed to be linear. The longitudinal and transverse cutoff frequencies have been set using the frequencies of each acoustic phonon mode at the Brillouin zone boundary in the [111] direction for Al [33] and [0001] direction for SiC [34]. The pressure dependence of the cutoff frequencies was assumed to scale with the Debye frequencies of Al and SiC at high pressures. The $G(P)$ of the Al/SiC interface calculated by DMM_T has a rate of change with pressure, $dG/dP \approx 6$ MW m^{-2} K^{-1} GPa^{-1}, in good agreement with the experimentally determined average slope for the clean Al/SiC interface, $dG/dP \approx 4.5 \pm 1$ MWm^{-2} K^{-1} GPa^{-1}. The DMM_T well describes both the magnitude and pressure dependence of G of a clean interface. The dashed-dot line shows the calculated $G(P)$ of Al/SiC interface using DMM based on a full Debye model (DMM_F) in which the linear phonon dispersion

extends to the zone boundary without being truncated.

$G(P)$ of the Al/SiC interface predicted by phonon radiation limit (PRL) is shown as the solid line in Fig. 5.4(a). In the high temperature limit, the radiation limit is given by $G_{PRL} = \pi k_B \nu_{\max}^{3} / c_D^{2}$, where k_B is the Boltzmann constant, $\nu_{\max}$ is the maximum vibrational frequency of Al, and c_D is the Debye velocity of SiC. I used $\nu_{\max}$=10 THz at ambient conditions taken from Ref. [33] and assumed that the pressure dependence of $\nu_{\max}$ scales with the Debye frequency of Al at high pressures. The predicted $G(P)$ by PRL is higher than the data for the $G(P)$ of clean Al/SiC interface by a factor of ≈3 over the pressure range I studied (see section 5.2 for the discussion of PRL).

The thermal conductance of Al/SiO_x/SiC interface, see the solid circles in Fig. 5.4(a), shows strikingly different behavior. At ambient pressure, G ≈55 $MWm^{-2}K^{-1}$, a factor of 4 smaller than G of a clean Al/SiC interface. Moreover, $G(P)$ of the Al/SiO_x/SiC interface increases dramatically with pressure and then saturates at ≈200 $MWm^{-2}K^{-1}$ after P>8 GPa. Such behavior suggests that interfacial thermal transport is suppressed by the low interface stiffness at low pressure regime.

For the graphene-inserted interfaces, i.e., Al/graphene/SiO_x/SiC, the interface stiffness is further reduced. The thermal conductance G at ambient pressure is lower than G of Al/SiO_x/SiC interface by an additional factor of ≈2, and is only weakly

dependent on the thickness of the native oxide: the open triangles in Fig. 5.4 are $G(P)$ of Al/graphene/SiO_x/SiC with a 0.5 nm-thick native oxide layer grown on a pre-cleaned SiC, and the solid triangles are $G(P)$ of Al/graphene/SiO_x/SiC with the 1 nm native oxide of the as-received SiC anvil. The two sets of data behave nearly the same.

The data for $G(P)$ shown in Fig. 5.4 include measurements for both increasing and decreasing P. The lack of any obvious hysteresis shows that changes in the interface stiffness under pressure are reversible.

Fig. 5.4(b) shows that at low pressure regime, $G(P)$ of weak interfaces increases approximately linearly with pressure. As the pressure is increased higher than 8 GPa , $G(P)$ approach the data for the clean Al/SiC interface and the value predicted by the DMM_T. Furthermore, the overall behavior of $G(P)$ of weak interfaces is consistent with the results of molecular dynamics simulations on qualitatively similar interfaces [12, 13].

The pressure dependence of interface thermal conductance $G(P)$ can not be described by a simple function of pressure. For an interface with low interface stiffness, the phonon transmission coefficient decreases rapidly with increasing phonon vibrational frequency and the frequency range in which the phonons are transmitted is narrow. As pressure increases the interface stiffness, the transmission

frequency window broadens, leading to an increase in the average phonon transmission coefficient. When the interface stiffness is strengthened to approach the limit of strong bonding, most of phonon modes contribute to the thermal transport at interface and the transmission coefficient eventually saturates at a large value as predicted by the DMM_T.

Pressure tuning of the interface bonding over a broad range of stiffness demonstrates that the interface stiffness dominates the thermal transport at weak interfaces, but plays a minor role for strong interfaces. The DMM based on a truncated Debye model correctly predicts the thermal conductance only when the interface stiffness is comparable to the stiffness of chemical bonds.

5.2 Thermal conductance of Al/MgO interface

In the previous section, it was shown that the DMM based on a truncated Debye model, DMM_T, well describes both the magnitude and pressure dependence of thermal conductance $G(P)$ of a clean Al/SiC interface. Here, I present my measurements of $G(P)$ of Al/MgO interface at room temperature up to 60 GPa and compare the data with DMM calculations for $G(P)$ using a truncated Debye model (DMM_T) and a full Debye model (DMM_F).

Figure 5.5 shows the pressure dependence of thermal conductance $G(P)$ of Al/MgO interface measured by TDTR combined with diamond anvil cell techniques. $G(P)$ of Al/MgO interface was extracted from the same set of data acquired in the measurements of the pressure dependent thermal conductivity of MgO, see section 3.2 for the details of sample preparation and experimental setup. The thermal conductance of the clean Al/MgO interface at ambient pressure is high, $G \approx 470$ MWm^{-2} K^{-1}, and is weakly dependent on pressure. The calculated $G(P)$ of Al/MgO interface using the DMM_T, DMM_F, and PRL are shown as the dashed, dashed-dot, and solid lines, respectively, in Fig. 5.5. In contrast with the $G(P)$ of Al/SiC interface which is well accounted for by the DMM_T, the $G(P)$ of Al/MgO interface is better described by the DMM_F. The calculated $G(P)$ using PRL is much higher than the data.

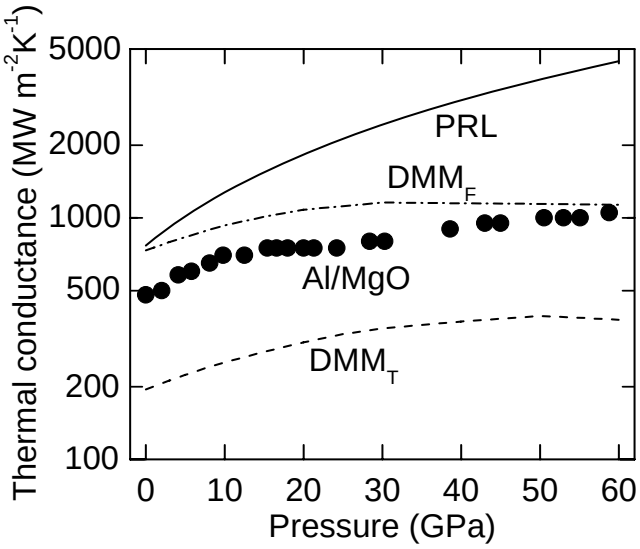

Fig. 5.5. Pressure dependence of the thermal conductance $G(P)$ of Al/MgO interface at room temperature. The calculated $G(P)$ using DMM_T, DMM_F, and PRL are plotted as dashed, dashed-dot, and solid lines, respectively.

To gain insight into the physics of thermal transport across interfaces, I compare phonon densities of states (DOS) of Al, MgO, and SiC under different assumptions. Real DOS taken from Refs [35-38] , DOS based on a full Debye model, and DOS based on a truncated Debye model are shown in Fig. 5.6(a), (b), and (c), respectively; all these DOS are at ambient conditions. As expected, the full Debye model overcounts the real DOS, resulting in excess thermal transport at higher frequencies that do not exist in the real DOS [39, 40]. The truncated Debye model, on the other hand, underestimates the available modes that contribute to the heat transport across interfaces.

Even though the modeled DOS significantly deviates from the details of the real DOS, these models may still describe the measured thermal conductance well. For example, in the truncated Debye model, see Fig. 5.6(c), the overlap of DOS between Al and SiC is similar to the overlap of their real DOS, and thereby the calculated thermal conductance of clean Al/SiC interface by DMM_T is in good agreement with the measured value. By contrast, for the Al/MgO interface, the overlap of DOS in the truncated Debye model is much smaller than that of real DOS and the calculated *G* is lower than the measured value. The predicted interface thermal conductance depends mostly on the similarity between the overlap of real and

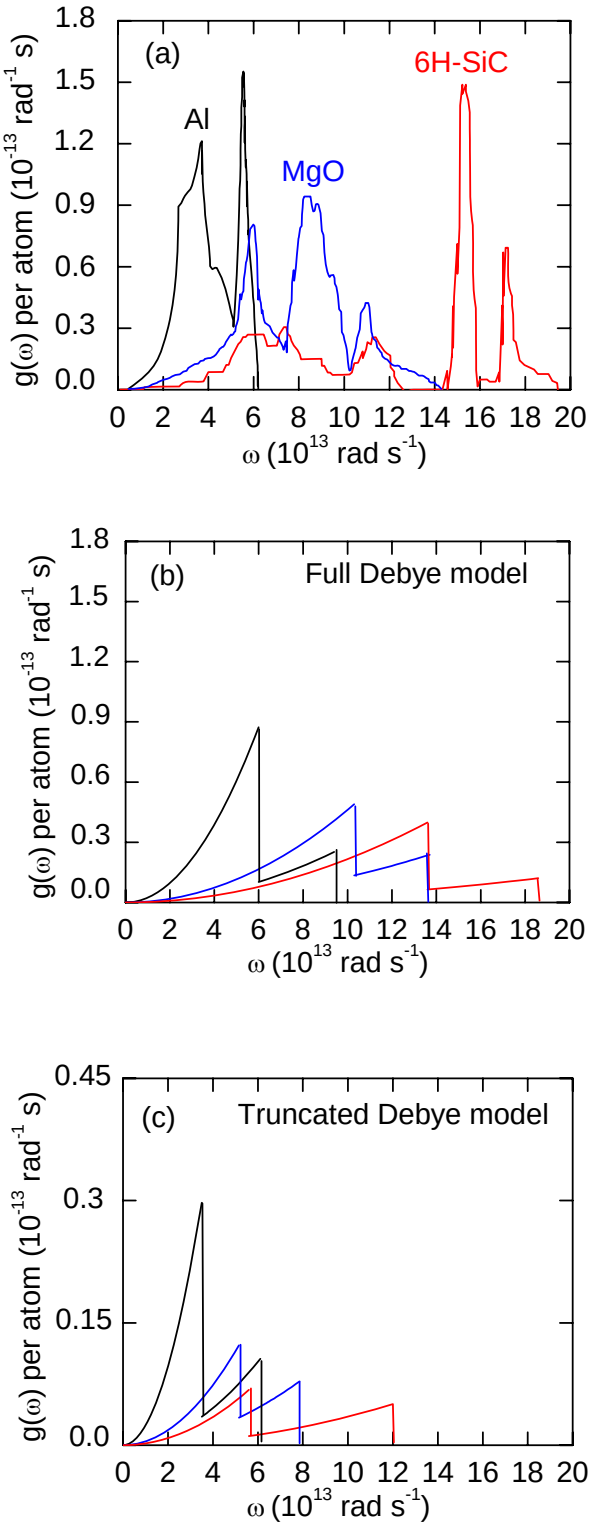

Fig. 5.6. Phonon densities of states (DOS) of Al (black), MgO (blue), and SiC (red) at ambient conditions. **(a)** Real DOS taken from Refs.[35-38]. The total area under each DOS curve is 3. **(b)** Modeled DOS using full Debye model. **(c)** Modeled DOS using truncated Debye model where the cutoff frequencies are set by the frequencies at zone boundaries [33-35]. Note that the DOS in (c) is in different extent.

modeled DOS, the quality of which varies depending on the cutoff frequencies set in the DMM_T.

Note that the calculated $G(P)$ of Al/SiC and Al/MgO interfaces at ambient using PRL are both higher than the measured values, see Fig. 5.4(a) and Fig. 5.5. In the real DOS, the maximum frequency of Al, ν_{max}=10 THz, is close to the frequencies of transverse acoustic modes of SiC and MgO at zone boundary, where the phonons do not substantially contribute to the thermal transport due to the small group velocities. In other words, the assumption of the PRL that all the phonons with frequencies lower than ν_{max} of Al are linear dispersed and have transmission coefficient of unity is invalid, leading to an overestimated thermal conductance.

5.3 Conclusion

In this chapter, I demonstrate the importance of interface stiffness on the interfacial thermal transport by measuring the pressure dependence of thermal conductance $G(P)$ of clean and modified Al/SiC interfaces at pressures as high as P=12 GPa. Diffuse mismatch model with phonon densities of states and cutoff frequencies similar to the real values is able to predict the observed thermal conductance of clean interfaces.

5.4 References

[1] D. G. Cahill, W. K. Ford, K. E. Goodson, G. D. Mahan, A. Majumdar, H. J. Maris, R. Merlin, and S. R. Phillpot, J. Appl. Phys. **93**, 793 (2003).

[2] C. W. Nan, R. Birringer, D. R. Clarke, and H. Gleiter, J. Appl. Phys. **81**, 6692 (1997).

[3] S. Shenogin, L. P. Xue, R. Ozisik, P. Keblinski, and D. G. Cahill, J. Appl. Phys. **95**, 8136 (2004).

[4] Y. K. Koh, Y. Cao, D. G. Cahill, and D. Jena, Adv. Funct. Mater. **19**, 610 (2009).

[5] C. Chiritescu, D. G. Cahill, N. Nguyen, D. Johnson, A. Bodapati, P. Keblinski, and P. Zschack, Science **315**, 351 (2007).

[6] R. M. Costescu, D. G. Cahill, F. H. Fabreguette, Z. A. Sechrist, and S. M. George, Science **303**, 989 (2004).

[7] S. T. Huxtable, A. R. Abramson, C. L. Tien, A. Majumdar, C. LaBounty, X. Fan, G. H. Zeng, J. E. Bowers, A. Shakouri, and E. T. Croke, Appl. Phys. Lett. **80**, 1737 (2002).

[8] E. T. Swartz, and R. O. Pohl, Rev. Mod. Phys. **61**, 605 (1989).

[9] H. K. Lyeo, and D. G. Cahill, Phys. Rev. B **73**, 144301 (2006).

[10] N. S. Snyder, Cryogenics **10**, 89 (1970).

[11] R. J. Stoner, and H. J. Maris, Phys. Rev. B **48**, 16373 (1993).

[12] M. Hu, P. Keblinski, and P. K. Schelling, Phys. Rev. B **79**, 104305 (2009).

[13] Z. Y. Ong, and E. Pop, Phys. Rev. B **81**, 155408 (2010).

[14] B. N. J. Persson, A. I. Volokitin, and H. Ueba, J. Phys. -Conden. Matt. **23**, 045009 (2011).

[15] M. Shen, W. J. Evans, D. G. Cahill, and P. Keblinski, unpublished.

[16] R. Prasher, Appl. Phys. Lett. **94**, 041905 (2009).

[17] D. A. Young, and H. J. Maris, Phys. Rev. B **40**, 3685 (1989).

[18] P. Nagy, J. Nondestructive Evaluation **11**, 127 (1992).

[19] G. Tas, J. J. Loomis, H. J. Maris, A. A. Bailes, and L. E. Seiberling, Appl. Phys. Lett. **72**, 2235 (1998).

[20] R. G. Ross, P. Andersson, B. Sundqvist, and G. Backstrom, Rep. Prog. Phys. **47**, 1347 (1984).

[21] P. Beck, A. F. Goncharov, V. V. Struzhkin, B. Militzer, H. K. Mao, and R. J. Hemley, Appl. Phys. Lett. **91**, 181914 (2007).

[22] W. P. Hsieh, B. Chen, J. Li, P. Keblinski, and D. G. Cahill, Phys. Rev. B **80**, 180302 (2009).

[23] W. P. Hsieh, M. D. Losego, P. V. Braun, S. Shenogin, P. Keblinski, and D. G. Cahill, Phys. Rev. B **83**, 174205 (2011).

[24] C. Onneby, and C. G. Pantano, J. Vac. Sci. Tech. A **15**, 1597 (1997).

[25] X. S. Li, W. W. Cai, J. H. An, S. Kim, J. Nah, D. X. Yang, R. Piner, A. Velamakanni, I. Jung, E. Tutuc, S. K. Banerjee, L. Colombo, and R. S. Ruoff, Science **324**, 1312 (2009).

[26] D. Graf, F. Molitor, K. Ensslin, C. Stampfer, A. Jungen, C. Hierold, and L. Wirtz, Nano Lett. **7**, 238 (2007).

[27] H. K. Mao, P. M. Bell, J. W. Shaner, and D. J. Steinberg, J. Appl. Phys. **49**, 3276 (1978).

[28] Z. B. Ge, D. G. Cahill, and P. V. Braun, Phys. Rev. Lett. **96**, 186101 (2006).

[29] C. Thomsen, H. T. Grahn, H. J. Maris, and J. Tauc, Phys. Rev. B **34**, 4129 (1986).

[30] B. Chen, W. P. Hsieh, D. G. Cahill, D. R. Trinkle, and J. Li, Phys. Rev. B **83**, 132301 (2011).

[31] D. G. Cahill, Rev. Sci. Instrum. **75**, 5119 (2004).

[32] Y. K. Koh, M. H. Bae, D. G. Cahill, and E. Pop, Nano Lett. **10**, 4363 (2010).

[33] R. Stedman, and G. Nilsson, Phys. Rev. **145**, 492 (1966).

[34] D. W. Feldman, J. H. Parker, W. J. Choyke, and L. Patrick, Phys. Rev. **173**, 787 (1968).

[35] S. Ghose, M. Krisch, A. R. Oganov, A. Beraud, A. Bosak, R. Gulve, R. Seelaboyina, H. Yang, and S. K. Saxena, Phys. Rev. Lett. **96**, 035507 (2006).

[36] M. Hofmann, A. Zywietz, K. Karch, and F. Bechstedt, Phys. Rev. B **50**, 13401 (1994).

[37] R. Stedman, L. Almqvist, and G. Nilsson, Phys. Rev. **162**, 549 (1967).

[38] M. Kresch, M. Lucas, O. Delaire, J. Y. Y. Lin, and B. Fultz, Phys. Rev. B **77**, 024301 (2008).

[39] J. C. Duda, T. E. Beechem, J. L. Smoyer, P. M. Norris, and P. E. Hopkins, J Appl Phys **108**, 073515 (2010).

[40] P. Reddy, K. Castelino, and A. Majumdar, Appl. Phys. Lett. **87**, 211908 (2005).

CHAPTER 6

METAL FILM TRANSDUCERS FOR TIME-DOMAIN THERMOREFLECTANCE AT HIGH PRESSURES

Parts of this chapter were published in *J. Appl. Phys.* **109**, 113520 (2011) by Wen-Pin Hsieh and David G. Cahill.

6.1 Introduction

Time-domain thermoreflectance (TDTR) [1, 2], as introduced in Chapter 2, is an ultrafast pump-probe technique and has been widely employed to measure thermal conductivity of thin film materials [3, 4] as well as the interface thermal conductance [5, 6]. TDTR utilizes the thermoreflectance, changes in the reflectivity as a function of temperature dR/dT, of a metal film as a thermometer. The surface temperature variation of the metal film is monitored by measuring changes in the reflectivity. Typically Al is the metal film transducer used in TDTR measurements due to its large thermoreflectance at laser wavelengths near 785 nm.

In Chapters 3 to 5, I have shown that the combination of TDTR with diamond and SiC anvil cells is a powerful tool to study pressure dependence of heat transport in various materials [7-10]. However, dR/dT of Al is found to be sensitive to the pressure and even crosses through zero at $P \approx 6$ GPa [8] which degrades the signal-to-noise ratio. Moreover, the low melting temperature of Al limits its use in high temperature measurements. A previous study of the thermoreflectance of several metals reported that Ta and Au with ≈5 at. % Pd have thermoreflectances comparable to Al at a laser wavelength of 785 nm [11] at ambient pressure. In order to find useful alternatives of Al in TDTR measurements at high pressures and temperatures, I investigated pressure dependence of the thermoreflectance and piezo-optical coefficients of Ta, Au(Pd), and Al films.

6.2 Experiments

6.2.1 Sample preparation

I deposited ≈80 nm-thick metal films of Al, Ta, and Au(Pd) on SiC anvils using magnetron sputtering. Since the equilibrium α-phase Ta has higher thermal conductivity than β-phase Ta, the SiC anvil was heated to ~900 K during the Ta film deposition [12-14]. X-ray diffraction shows that such a Ta film deposited on a Si wafer heated to ~900 K during the film deposition has a strong [110] texture, which

confirms that crystal structure of the Ta film is that of the bcc α-phase. The expected [111] texture of Au(Pd) films deposited on Si wafers was also confirmed by X-ray diffraction. Since the culet size of the SiC anvil is only 600 μm, I used four-point probe measurements of the in-plane electrical conductivity combined with the Wiedemann-Franz law to determine the thermal conductivities Λ of Al, Ta, and Au(Pd) thin films deposited on Si wafers. (The Si wafers were also included in the sputtering chamber during the deposition of metal films on SiC anvils.) The thermal conductivities of the Al, Ta, and Au(Pd) thin films were 200, 45, and 80 W m^{-1} K^{-1}, respectively. The SiC anvils coated with metal films were pressurized by loading with H_2O as the pressure medium. The pressure was measured by ruby fluorescence [15]. Figure 6.1 shows a schematic illustration of the TDTR measurements of metal films in a SiC anvil cell.

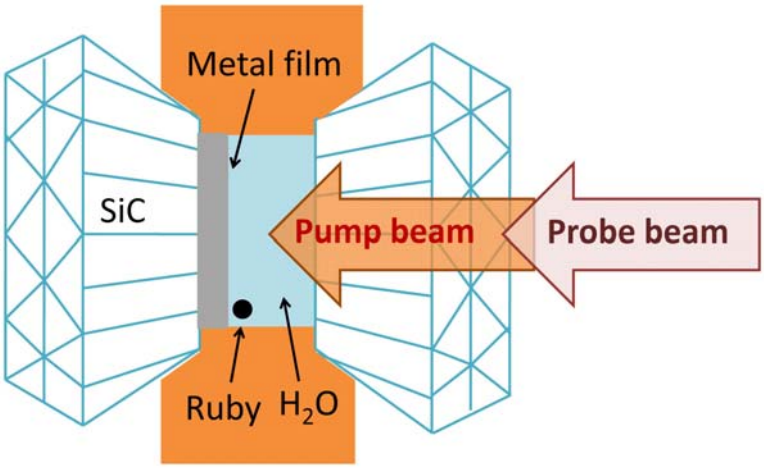

Fig. 6.1. Schematic illustration of the time-domain thermoreflectance measurements of metal films within a SiC anvil cell. A small ruby chip is loaded into the sample chamber to measure the pressure. H_2O is the pressure medium.

6.2.2 Measuring thermoreflectance by TDTR

I used time-domain thermoreflectance (TDTR) with a laser wavelength of 785 nm to measure the pressure dependence of the thermoreflectance of metal films [1, 2, 11, 16]. The details of the TDTR system are described in Chapter 2. In my experiments, the power of the pump and probe beams were fixed at 20 and 10 mW, respectively, and both pump and probe beams were focused on the surface of the metal film to a $1/e^2$ intensity radius of ≈7.5 μm using a 10× objective lens. The reflected probe beam intensity was measured by a Si photodiode detector. A resonant band-pass filter with a quality factor Q≈10 was used to enhance the output of the Si photodiode. The signal was then further enhanced by a preamplifier and finally measured by a radio-frequency lock-in amplifier which is set to synchronize with the 10 MHz modulation frequency of the pump pulse.

6.3 Results and discussion

6.3.1 Measuring the in-phase signals from TDTR

The thermoreflectance of metal films are determined by:

$$\frac{dR}{dT} = \frac{\sqrt{2}}{G_p Q} \frac{V_{in}(t = 80\,ps)}{V_0} \frac{R}{\Delta T(t = 80\,ps)}, \qquad (6.1)$$

where $G_p = 5$ is the gain of the preamplifier, $Q \approx 10$ is the quality factor of the resonant

circuit, $V_{in}(t = 80\,ps)$ is the in-phase voltage signal of the rf lock-in amplifier at a delay time t=80 ps between pump and probe pulses, V_0 is the average dc voltage generated by the photodiode detector as measured before the preamplifier, R is the optical reflectivity of the metal film, and $\Delta T(t = 80\,ps)$ is the calculated surface temperature at t=80 ps using the thermal model described in Ref [1]. Example data for $V_{in}(t)$ of Al, Ta, and Au(Pd) are shown in Fig. 6.2(a), (b), and (c), respectively.

Figure 6.3(a) shows the V_{in} signal at t=80 ps for Al, Ta, and Au(Pd) films as a function of pressure. Note that due to the reflection losses at interfaces between air/SiC and water/SiC, the V_{in} after the metal film is loaded into a SiC anvil cell is only ≈43 % of the signal before loading. At the air/SiC interface the reflectivity is R_1=0.17, and at the water/SiC interface the reflectivity is R_2=0.09. In my experimental setup, the pump beam passes through each interface once and the probe beam passes through each interface twice. Because the strength of the thermoreflectance signal is proportional to the product of the intensities of pump and probe beams, the V_{in} signal after the film is loaded in to the SiC anvil cell decreases by a factor of $(1-R_1)^3(1-R_2)^3 = 0.43$, i.e., 43% of the V_{in} before loading. For Al, V_{in} decreases from 140 μV to 55 μV; for Ta, V_{in} decreases from 470 μV to 190 μV; for Au(Pd), V_{in} decreases from 44 μV to 19 μV. All are in good agreement with the estimated reduction of the V_{in} due to the reflection losses.

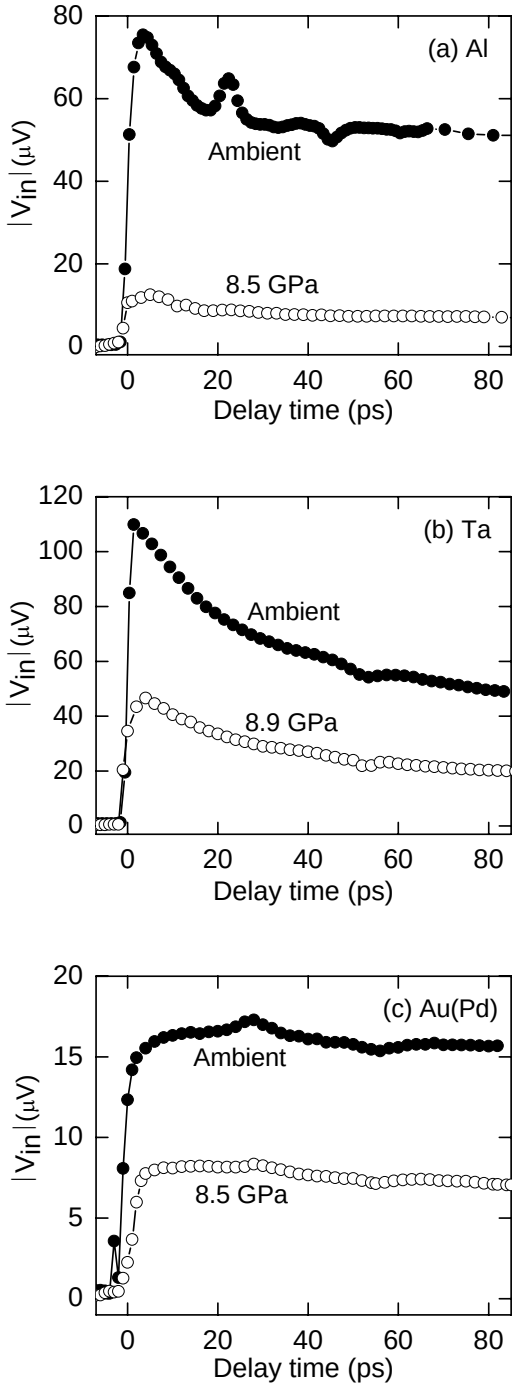

Fig. 6.2. Example data for $V_{in}(t)$, the in-phase voltage of the rf lock-in as a function of delay time between pump and probe for **(a)** Al, **(b)** Ta, and **(c)** Au(Pd) films deposited on SiC anvils. $V_{in}(t)$ is proportional to the change in optical reflectivity produced by the pump pulses. The thicknesses of Al, Ta, and Au(Pd) are 74 nm, 111 nm, and 91 nm, respectively, as measured by picosecond acoustics. Each panel includes data acquired at ambient pressure before assembling the SiC anvil cell, and data acquired after the anvil cell is loaded and pressurized to $P \approx 8.5$ GPa.

Au(Pd) and Ta films both show nearly constant V_{in} with pressure. However, the V_{in} signal of Al is highly sensitive to the pressure and undesirably crosses through zero near $P \approx 6$ GPa. (Data for $P > 12$ GPa were collected from an Al film deposited on a muscovite mica within a diamond anvil cell using H_2O as the pressure medium.) Therefore, the signal-to-noise ratio and accuracy of the thermal measurements using Al transducer in the range $5 < P < 7$ GPa are substantially degraded. (To overcome this problem I shifted the laser wavelength to 765 nm and used another set of optical filters, see section 3.1 for the details.)

6.3.2 Pressure dependence of the thermoreflectance

Data for the pressure dependence of V_{in}, as shown in Fig. 6.3(a), were converted to the pressure dependence of the thermoreflectance, dR/dT, using Eq. (6.1), see Fig.6.3(b). To do this conversion, the optical reflectivity of each metal film [11] was assumed to be a constant in the pressure range I studied. At ambient conditions, the thermoreflectance of thin films of Al ($dR/dT \approx 1.31\times10^{-4}$ K^{-1}), Ta ($dR/dT \approx 1.42\times10^{-4}$ K^{-1}), and Au(Pd) ($dR/dT \approx 0.6\times10^{-4}$ K^{-1}) are in good agreement with the literature values [11]. The dR/dT of Al under pressure is sensitive to pressure and goes through zero near 6 GPa. (The applied pressure blue-shifts the absorption edges of Al to higher energy [17].) By contrast, dR/dT of Ta and Au(Pd) are comparable to that of Al

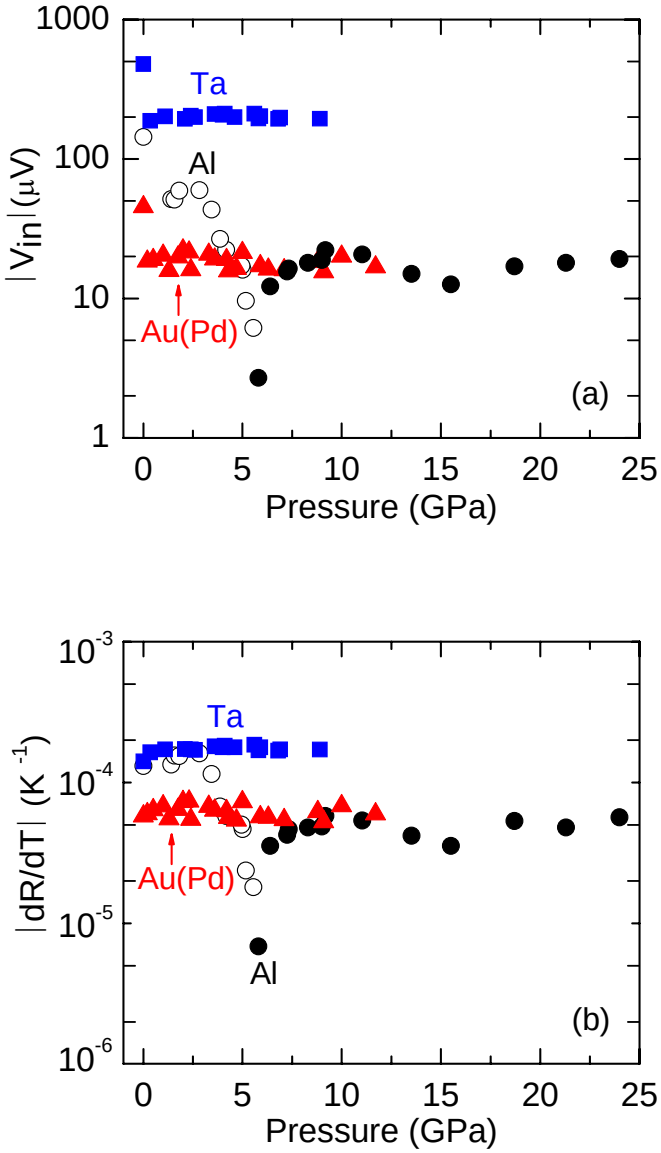

Fig. 6.3. (a) Pressure dependence of the in-phase voltage V_{in} of the rf lock-in amplifier at a delay time t=80 ps for Al, Ta, and Au(Pd) thin films deposited on SiC. The V_{in} signal after the film is loaded into a SiC anvil cell is ≈43% of the signal before loading. Data for Al at P>12 GPa were collected from an Al film on a muscovite mica within a diamond anvil cell. **(b)** Pressure dependence of the thermoreflectance dR/dT of the same three metal films. The dR/dT is obtained using the data for V_{in} in (a) and Eq. (6.1). Solid symbols denote negative values of V_{in} and dR/dT; open symbols denote positive values. V_{in} and dR/dT of Al change sign near P=6 GPa.

at ambient conditions but remains large under pressure, indicating that Ta and Au(Pd) transducers provide higher sensitivity than Al in the pressure range 4<P<10 GPa.

Furthermore, because of their high melting temperatures, Ta and Au(Pd) films are more suitable for TDTR measurements at high temperature. The melting points T_m of Ta and Au(Pd) at ambient conditions are ≈3269 K [18] and ≈1420 K [19], respectively, while T_m of Al is only 930 K. Melting temperatures typically increase with pressure: dT_m/dP≈11 K GPa^{-1} for Ta at P<20 GPa [18], dT_m/dP≈50 K GPa^{-1} for Au at P<7 GPa [20], and dT_m/dP≈50 K GPa^{-1} at P<20 GPa [21] for Al.

6.3.3 Strength of the acoustic echo at high pressures

As discussed in the section 2.1.5, the thickness of a metal film can be accurately derived from the position of the acoustic echo in picosecond acoustics [22]. Therefore, large values of the piezo-optical coefficient, which characterizes changes in optical reflectivity with acoustic strain, are desirable in picoseconds acoustics experiments.

The thickness of a metal film is determined by multiplying the speed of sound of meal by half of acoustic echo time. The speed of longitudinal sound along the [110] direction of bcc Ta is 4.2 nm ps^{-1} [23].The speed of sound in similar Au(Pd) 5% alloy films, 3.3 nm ps^{-1}, was measured by a combination of picosecond acoustics,

Rutherford backscattering spectroscopy, and assuming that the atomic density of Au(Pd) is accurately described by Vegard's law [24]. (Vegard's law is an approximate rule that predicts a linear relation between the lattice constant of an alloy and the concentration of the constituent elements.) For pure Au, the longitudinal speed of sound along the [111] direction is 3.24 nm ps^{-1} [25].

To characterize the relative strength of the piezo-optical coefficient for each metal film as a function of pressure, I compared the ratio of the acoustic echo strength to an estimate of the thermal expansion of the metal film. The example data in Fig. 6.2 shows that the acoustic echo of Al almost disappears at P=8.5 GPa; however, at similarly high pressures the acoustic echoes of Ta and Au(Pd) are still identifiable.

To analyze the acoustic echo strength, I first subtracted a smooth curve from the $V_{in}(t)$ and integrated the echo strength over an 8 ps range that is centered at the peak position of the echo. This integrated echo strength is then normalized by the value of $V_{in}(t)$ at t≈10 ps after the echo. To compare the acoustic signal strength between metal films, a figure-of-merit is created and defined by dividing the normalized echo strength obtained above by an estimate of thermal strain, which is the product of the thermal expansion coefficient α and the calculated temperature rise ΔT at the surface of the metal film. Here I assume that α of each metal [26, 27] is independent of the pressure in the range $0<P<12$ GPa. ΔT is calculated using the

thermal model described in Ref. [1]. As shown in Fig. 6.4, the figures-of-merit of Ta and Au(Pd) are approximately constant as a function of pressure. The figure-of-merit of Al, however, drops rapidly by approximately an order of magnitude with initial loading and is always small at P>2 GPa.

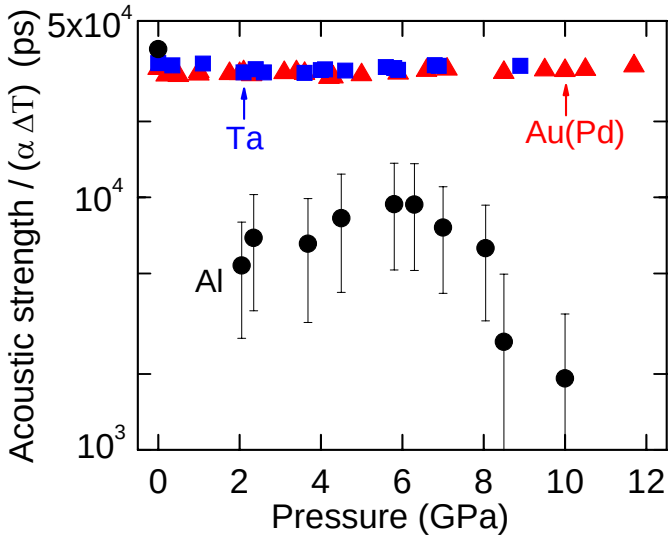

Fig. 6.4. Pressure dependence of the figure-of-merit for the strength of acoustic signals (integrated acoustic peak normalized by thermal strain) for Ta, Au(Pd), and Al films deposited on SiC anvils. The acoustic signal strengths for Ta and Au(Pd) are essentially independent of pressure while the acoustic signal strength for Al drops abruptly with initial loading.

6.4 Conclusion

Pressure dependence of the thermoreflectance and relative piezo-optical coefficients of Ta, Au(Pd), and Al metal films were measured by time-domain thermoreflectance within SiC anvil cells. I anticipate that this compilation of critical

parameters in TDTR measurements at high pressure will assist in the selection of suitable transducers, and ultimately enable the extension of TDTR techniques to higher pressures and temperatures. This extension will benefit studies of thermal transport in condensed matter systems, including geophysically important materials. For instance, Ta could be an excellent metal transducer to measure the thermal conductivity of major constituent minerals in the lower mantle, e.g., (Mg,Fe)O ferropericlase and (Mg,Fe)SiO_3 perovskite, under extreme pressures and temperatures comparable to the Earth's lower mantle.

6.5 References

[1] D. G. Cahill, Rev. Sci. Instrum. **75**, 5119 (2004).

[2] K. Kang, Y. K. Koh, C. Chiritescu, X. Zheng, and D. G. Cahill, Rev. Sci. Instrum. **79**, 114901 (2008).

[3] C. Chiritescu, D. G. Cahill, N. Nguyen, D. Johnson, A. Bodapati, P. Keblinski, and P. Zschack, Science **315**, 351 (2007).

[4] R. M. Costescu, D. G. Cahill, F. Fabreguette, Z. Sechrist, and S. George, Science **303**, 989 (2004).

[5] Z. B. Ge, D. G. Cahill, and P. V. Braun, Phys. Rev. Lett. **96**, 186101 (2006).

[6] H. K. Lyeo, and D. G. Cahill, Phys. Rev. B **73**, 144301 (2006).

[7] B. Chen, W. P. Hsieh, D. G. Cahill, D. Trinkle, and J. Li, Phys. Rev. B **83**, 132301 (2011).

[8] W. P. Hsieh, B. Chen, J. Li, P. Keblinski, and D. G. Cahill, Phys. Rev. B **80**, 180302 (2009).

[9] W. P. Hsieh, M. Losego, P. Braun, S. Shenogin, P. Keblinski, and D. G. Cahill, Phys. Rev. B **83**, 174205 (2011).

[10] W. P. Hsieh, A. Lyons, E. Pop, P. Keblinski, and D. G. Cahill, (in preparation).

[11] Y. X. Wang, J. Park, Y. K. Koh, and D. G. Cahill, J. Appl. Phys. **108**, 043507 (2010).

[12] P. Catania, J. P. Doyle, and J. J. Cuomo, J. Vac. Sci. Technol. A **10**, 3318 (1992).

[13] D. W. Face, and D. E. Prober, J. Vac. Sci. Technol. A **5**, 3408 (1987).

[14] S. Sato, Thin Solid Films **94**, 321 (1982).

[15] H. K. Mao, P. Bell, J. Shaner, and D. Steinberg, J. Appl. Phys. **49**, 3276 (1978).

[16] C. A. Paddock, and G. L. Eesley, J. Appl. Phys. **60**, 285 (1986).

[17] R. Dandrea, and N. Ashcroft, Phy. Rev. B **32**, 6936 (1985).

[18] D. Errandonea, M. Somayazulu, D. Hausermann, and H. K. Mao, J. Phys. Condens. Matt. **15**, 7635 (2003).

[19] H. Okamoto, and T. B. Massalski, J. Phase Equilibria **6**, 229 (1985).

[20] P. W. Mirwald, and G. C. Kennedy, J. Geophys. Res. **84**, 6750 (1979).

[21] R. Boehler, and M. Ross, Earth Planet. Sci. Lett. **153**, 223 (1997).

[22] C. Thomsen, H. Grahn, H. Maris, and J. Tauc, Phys. Rev. B **34**, 4129 (1986).

[23] O. Gulseren, and R. E. Cohen, Phys. Rev. B **65**, 064103 (2002).

[24] A. R. Denton, and N. W. Ashcroft, Phys. Rev. A **43**, 3161 (1991).

[25] J. H. Hodak, A. Henglein, and G. V. Hartland, J. Chem. Phys. **111**, 8613 (1999).

[26] F. C. Nix, and D. MacNair, Phys. Rev. **60**, 597 (1941).

[27] F. C. Nix, and D. MacNair, Phys. Rev. **61**, 74 (1942).

CHAPTER 7

CONCLUSIONS

The novel combination of time-domain thermoreflectance (TDTR) with diamond and SiC anvil cell techniques is a powerful approach to measure the thermal transport properties of materials at extreme pressures and temperatures. Extreme pressures are particularly necessary to significantly vary physical properties relevant to thermal transport, such as elastic constants, phonon densities of states and interface stiffness, and thereby further explore the physics of heat conduction in various materials.

By measuring the pressure dependence of cross-plane thermal conductivity of a muscovite mica crystal, I discovered that the cross-plane sound velocity plays a dominant role in the thermal transport in anisotropic layered crystals. This study provides important clues to the origin of the ultralow thermal conductivity observed in disordered layered crystals.

I tested the minimum thermal conductivity model for a prototypical amorphous polymer, poly(methyl methacrylate) (PMMA). The good agreement between the pressure dependence of the thermal conductivity of PMMA measured by

TDTR combined with a SiC anvil cell and the prediction based on the minimum thermal conductivity model verifies the model's validity for describing thermal transport behavior in amorphous polymers.

I demonstrated the importance of interface stiffness on heat transfer across interfaces by studying the pressure dependence of the thermal conductance of weak interfaces. The interface stiffness dominates the thermal transport at weak interfaces, but becomes a minor effect as the stiffness is strengthened to approach the limit of strongly bonded interfaces.

I also measured the pressure dependence of the thermoreflectance and piezo-optical coefficients of Al, Ta, and Au(Pd). Compare to Al, Ta and Au(Pd) are more suitable for TDTR experiments at high pressures and temperatures, such as measurements of thermal conductivity of minerals at conditions comparable to the Earth's lower mantle.

Since TDTR combined with gem anvil cells is also compatible with applications of other external stimuli, e.g., temperature and magnetic/electric fields, I anticipate that much more interesting physics of thermal transport will be uncovered using TDTR and anvil cells under some combinations of extreme pressure, temperature, and magnetic/electric fields.

APPENDIX A

THERMAL TRANSPORT IN SPIN LADDER MATERIALS

A.1 Introduction

Thermal transport by collective, magnetic excitations called magnons was first predicted by Fröhlich and co-workers [1]. Approximately 30 years later, Luthi provided the first experimental evidence showing the heat conduction in yttrium-iron-garnet at low temperature regime is mainly due to the magnons [2]. Recently large magnetic contribution to the thermal transport was discovered in a spin ladder material $Sr_{14}Cu_{24}O_{41}$ [3-5] and since then various studies on the heat conduction in one-dimensional spin ladder materials, in particular the (Sr, Ca, La)$_{14}Cu_{24}O_{41}$ cuprate family, have been performed [6-11].

In (Sr, Ca, La)$_{14}Cu_{24}O_{41}$ crystals, there are two quasi-one-dimensional subsystems along the *c* axis. One is the Cu_2O_3 two-leg ladders in which parallel pairs of spin chains are strongly coupled with each other via the Cu-O-Cu interactions. The other subsystem is the CuO_2 chains that have weak magnetic coupling. Figure A.1

illustrates the spin arrangements in the (Sr, Ca, La)$_{14}$Cu$_{24}$O$_{41}$ spin ladder materials.

Investigations of the magnon thermal transport could provide information regarding the magnetic excitations, e.g. the scattering of magnons. Here, I present my preliminary studies of the temperature dependent thermal conductivity of the spin ladder material $Ca_9La_5Cu_{24}O_{41}$.

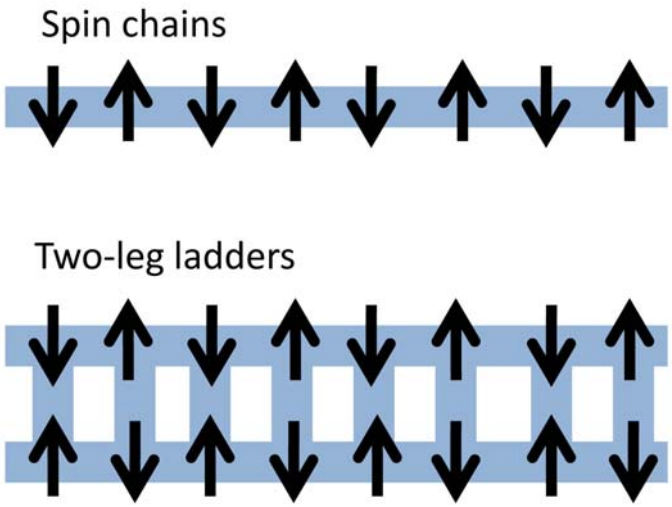

Fig. A.1. Schematic illustration of the spin structures of (Sr, Ca, La)$_{14}$Cu$_{24}$O$_{41}$. The upper panel shows a spin chain and the lower panel shows a two-leg spin ladder. The blue bars indicate the antiferromagnetic coupling between spins.

A.2 Experimental results

The $Ca_9La_5Cu_{24}O_{41}$ samples were provided by Prof. Paul H. M.van Loosdrecht's group at the Zernike Institute for Advanced Materials, Groningen, Netherlands. The sample was first mounted on a tripod polisher by crystal bond and dry-polished using SiC sandpapers with grit sizes of P800, P2400, and P4000 on a rotating polisher until the sample surface was observed flat under an optical

microscope. The polished sample was then annealed at 820-1170 K for one hour at ambient condition and deposited ≈80 nm-thick Al film after the sample cooled to room temperature. I measured the temperature dependence of the thermal conductivity along the *c* axis, i.e., the spin ladder direction, at ambient pressure using time-domain thermoreflectance (TDTR), see section 2.1 for the details of TDTR. Note that since the measurements were performed at ambient pressure, no gem anvil cell was used.

The thickness of Al was measured by picosecond acoustics. Since the volumetric heat capacity C_v of $Ca_9La_5Cu_{24}O_{41}$ is not known, I used C_v =2.3 J cm^{-3} K^{-1}, a typical value for oxide, at room temperature and fixed the value of C_v at high temperatures.

Figure A.2 shows the preliminary measurements of the thermal conductivity of $Ca_9La_5Cu_{24}O_{41}$ along the *c*-axis from room temperature to 573 K. The thermal conductivity is weakly dependent on the modulation frequency of the pump beam which determines the thermal penetration depth, see Eq. 2.2. (The thermal penetration depth is ≈300 nm-5 μm in my experiments.) Because the volumetric heat capacity of $Ca_9La_5Cu_{24}O_{41}$ is assumed to be a constant, a slope of ≈ -2 on this log-log plot, corresponding to $\Lambda \propto T^{-2}$, is difficult to justify.

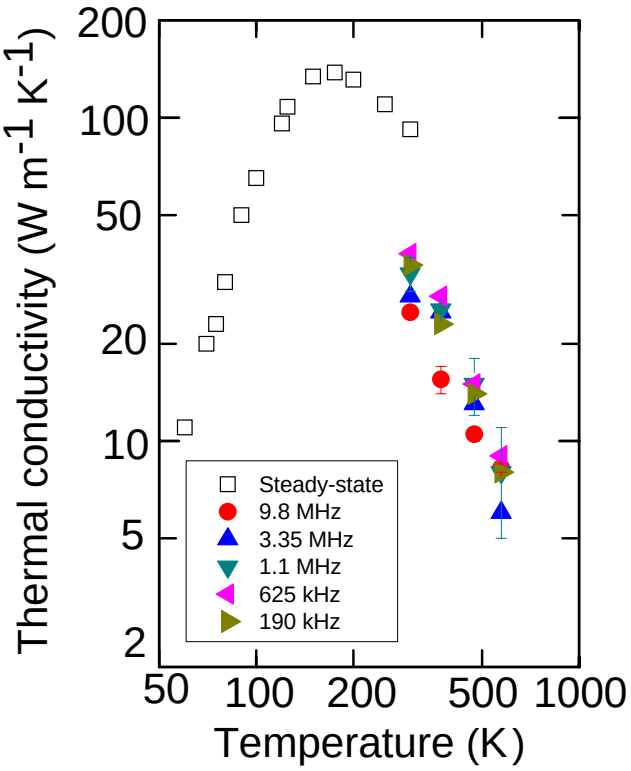

Fig. A.2. Thermal conductivity of $Ca_9La_5Cu_{24}O_{41}$ along the *c*-axis as a function of temperature and modulation frequency of the pump beam. Data measured by steady-state technique [3] (open squares) is plotted for comparison.

Also plotted in Fig. A.2 is the literature data measured by steady-state technique [3]. At room temperature the thermal conductivity measured by steady-state technique is higher than my data by a factor of ≈2-3. Further studies on the reason causing such difference and measurements of thermal conductivity at lower temperatures are ongoing.

A.3 References

[1] H. Frohlich, and W. Heitler, Proc. R. Soc. Lond. A **155**, 640 (1936).

[2] B. Luthi, J. Phys. Chem. Solids **23**, 35 (1962).

[3] C. Hess, C. Baumann, U. Ammerahl, B. Buchner, F. Heidrich-Meisner, W. Brenig, and A. Revcolevschi, Phys. Rev. B **64**, 184305 (2001).

[4] A. V. Sologubenko, K. Gianno, H. R. Ott, U. Ammerahl, and A. Revcolevschi, Phys. Rev. Lett. **84**, 2714 (2000).

[5] K. Kudo, S. Ishikawa, T. Noji, T. Adachi, Y. Koike, K. Maki, S. Tsuji, and K. Kumagai, J. Low Temp. Phys. **117**, 1689 (1999).

[6] C. Hess, H. ElHaes, B. Buchner, U. Ammerahl, M. Hucker, and A. Revcolevschi, Phys. Rev. Lett. **93**, 027005 (2004).

[7] A. V. Sologubenko, K. Gianno, H. R. Ott, A. Vietkine, and A. Revcolevschi, Phys. Rev. B **6405**, 054412 (2001).

[8] A. V. Sologubenko, E. Felder, K. Gianno, H. R. Ott, A. Vietkine, and A. Revcolevschi, Phys. Rev. B **62**, R6108 (2000).

[9] M. Hofmann, T. Lorenz, K. Berggold, M. Gruninger, A. Freimuth, G. S. Uhrig, and E. Bruck, Phys. Rev. B **67**, 184502 (2003).

[10] A. V. Rozhkov, and A. L. Chernyshev, Phys. Rev. Lett. **94**, 087201 (2005).

[11] C. Hess, Europ. Phys. J. -Special Topics **151**, 73 (2007).

AUTHOR'S BIOGRAPHY

Wen-Pin Hsieh received his B.S. and M.S. in Physics from National Taiwan University, Taiwan, Republic of China, in 2004 and 2005, respectively. During his undergraduate and master studies, he worked with Dr. Yuh-Lin Wang at the Institute of Atomic and Molecular Sciences, Academia Sinica. Starting from August 2007, Wen-Pin began to pursue his Ph.D. degree in Physics at the University of Illinois, Urbana-Champaign. He joined Prof. David Cahill's group since the summer of 2008 and studied the physics of thermal transport at extreme pressure using an ultrafast pump-probe method combined with diamond anvil cell techniques. After finishing his Ph.D. degree, Wen-Pin will move to Bay area and work as a postdoctoral researcher at Stanford University, California, and Stanford Linear Accelerator Center, National Accelerator Laboratory.